2022-06

NUMERICAL MODELING OF FLUID BEHAVIOR AROUND A HOVERING DRONE ROTOR

Richmond, Alexander K.

Monterey, CA; Naval Postgraduate School

NAVAL POSTGRADUATE SCHOOL

MONTEREY, CALIFORNIA

THESIS

NUMERICAL MODELING OF FLUID BEHAVIOR AROUND A HOVERING DRONE ROTOR

by

Alexander K. Richmond

June 2022

Thesis Advisor: Anthony J. Gannon
Co-Advisor: Christopher S. Clay

THIS PAGE INTENTIONALLY LEFT BLANK

REPORT DOCUMENTATION PAGE			*Form Approved OMB No. 0704-0188*

1. AGENCY USE ONLY *(Leave blank)*	**2. REPORT DATE** June 2022	**3. REPORT TYPE AND DATES COVERED** Master's thesis

4. TITLE AND SUBTITLE NUMERICAL MODELING OF FLUID BEHAVIOR AROUND A HOVERING DRONE ROTOR	**5. FUNDING NUMBERS** RMQ80
6. AUTHOR(S) Alexander K. Richmond	
7. PERFORMING ORGANIZATION NAME(S) AND ADDRESS(ES) Naval Postgraduate School Monterey, CA 93943-5000	**8. PERFORMING ORGANIZATION REPORT NUMBER**
9. SPONSORING / MONITORING AGENCY NAME(S) AND ADDRESS(ES) ONR, Arlington, VA, 22217	**10. SPONSORING / MONITORING AGENCY REPORT NUMBER**

11. SUPPLEMENTARY NOTES The views expressed in this thesis are those of the author and do not reflect the official policy or position of the Department of Defense or the U.S. Government.

12a. DISTRIBUTION / AVAILABILITY STATEMENT Approved for public release. Distribution is unlimited.	**12b. DISTRIBUTION CODE** A

13. ABSTRACT (maximum 200 words)

Research conducted on a remote-controlled drone aids in the quantification of individual rotor performance in the hovering state. Analysis via a three-dimensional numerical model identifies specific flow characteristics that are unique to the drone blade selected for the study. These flow characteristics give insight to lifting force, torque, velocity and pressure characteristics exerted on and induced by the blade. These metrics are made available to validate and improve actuator disk theory for a disk-size equivalent to the rotor's planform area. Improvements to actuator disk theory occur by implementing pressure and velocity gradients extracted from the three-dimensional numerical simulation. Although computationally expensive, three-dimensional simulations provide most accurate results. Once the extracted radial pressure and velocity distributions are provided, less accurate and computationally cheaper analytical processes can be used as a substitution to this time-consuming investigation into vehicle performance.

14. SUBJECT TERMS drone, VTOL, motor, vertical take-off and landing, efficiency, actuator disk theory	**15. NUMBER OF PAGES** 149
	16. PRICE CODE

17. SECURITY CLASSIFICATION OF REPORT Unclassified	**18. SECURITY CLASSIFICATION OF THIS PAGE** Unclassified	**19. SECURITY CLASSIFICATION OF ABSTRACT** Unclassified	**20. LIMITATION OF ABSTRACT** UU

NSN 7540-01-280-5500

Standard Form 298 (Rev. 2-89)
Prescribed by ANSI Std. 239-18

THIS PAGE INTENTIONALLY LEFT BLANK

Approved for public release. Distribution is unlimited.

NUMERICAL MODELING OF FLUID BEHAVIOR AROUND A HOVERING DRONE ROTOR

Alexander K. Richmond
Ensign, United States Navy
BS, United States Naval Academy, 2021

Submitted in partial fulfillment of the
requirements for the degree of

MASTER OF SCIENCE IN AEROSPACE ENGINEERING

from the

NAVAL POSTGRADUATE SCHOOL
June 2022

Approved by: Anthony J. Gannon
Advisor

Christopher S. Clay
Co-Advisor

Garth V. Hobson
Chair, Department of Mechanical and Aerospace Engineering

THIS PAGE INTENTIONALLY LEFT BLANK

ABSTRACT

Research conducted on a remote-controlled drone aids in the quantification of individual rotor performance in the hovering state. Analysis via a three-dimensional numerical model identifies specific flow characteristics that are unique to the drone blade selected for the study. These flow characteristics give insight to lifting force, torque, velocity and pressure characteristics exerted on and induced by the blade. These metrics are made available to validate and improve actuator disk theory for a disk-size equivalent to the rotor's planform area. Improvements to actuator disk theory occur by implementing pressure and velocity gradients extracted from the three-dimensional numerical simulation. Although computationally expensive, three-dimensional simulations provide most accurate results. Once the extracted radial pressure and velocity distributions are provided, less accurate and computationally cheaper analytical processes can be used as a substitution to this time-consuming investigation into vehicle performance.

THIS PAGE INTENTIONALLY LEFT BLANK

TABLE OF CONTENTS

LIST OF FIGURES

LIST OF TABLES

THIS PAGE INTENTIONALLY LEFT BLANK

LIST OF ACRONYMS AND ABBREVIATIONS

A	Planform area
CFD	Computational fluid dynamics
C_L	Coefficient of lift
DC	Direct current
ESC	Electronic speed controller
F	Force
IPS	Inch, Pound, Seconds
N	Rotational velocity
NI	National Instruments
P	Power
PWM	Pulse width modulation
Q	Flow rate
RC	Remote control
RPM	Revolutions per minute
SOI	Sphere of influence
SST	Shear stress transport
v	Fluid velocity
VTOL	Vertical take-off and landing
y	Distance from wall
y^+	Y-plus value
υ	Kinematic viscosity
ρ	Fluid density
τ	Torque
τ_w	Wall shear stress
ω	Rotational velocity (rad/s)
$\perp Y$	Normal vector Y-direction
$\perp Z$	Normal vector Z-direction

THIS PAGE INTENTIONALLY LEFT BLANK

ACKNOWLEDGMENTS

I would like to thank the following people who supported me immensely through my research:

Ben and Karen Richmond, for their continual support and encouragement as I worked on getting my master's degree.

Dr. Anthony Gannon, for his guidance and aid in defining my research path.

Chris Clay for his continual insight and availability to help with setting up laboratory equipment and helping with testing.

THIS PAGE INTENTIONALLY LEFT BLANK

I. INTRODUCTION

A. BACKGROUND

1. Drones

Designing an aircraft that is able to fly like a helicopter and a fixed wing aircraft introduces multiple new design parameters for flight. Understanding and implementing vertical take-off and landing (VTOL) engineering concepts into drone design is a key element in both VTOL and horizontal flight performance and efficiency. In order to achieve flight, the total lifting force generated by the engine must exceed the weight of the vehicle [1]. The same principle is applicable for hovering, with the only difference being that the vehicle's gross weight must be counterbalanced by the thrust. It is advantageous then to have a lightweight drone in order to minimize the power required by the engine at take-off. The engine's rated power cannot be approached when conducting VTOL operations either, as higher power is necessary for maneuverability and rapid acceleration than is required for hovering [1]. For aircraft with a single lifting rotor (most helicopters), a second horizontally oriented rotor blade is required to offset the reactionary torque generated by the lifting rotor. Without this stabilizing rotor, aircraft flight would be unstable and an induced uncontrollable spinning would take place. Thus, for drone design, where there is no stabilizing rotor, it is necessary to have an even number of rotors as well as alternating their direction of rotation from clockwise to counterclockwise. In Figure 1, when circling the hexacopter, all even rotors spin in one direction and all odd rotors spin the opposite direction.

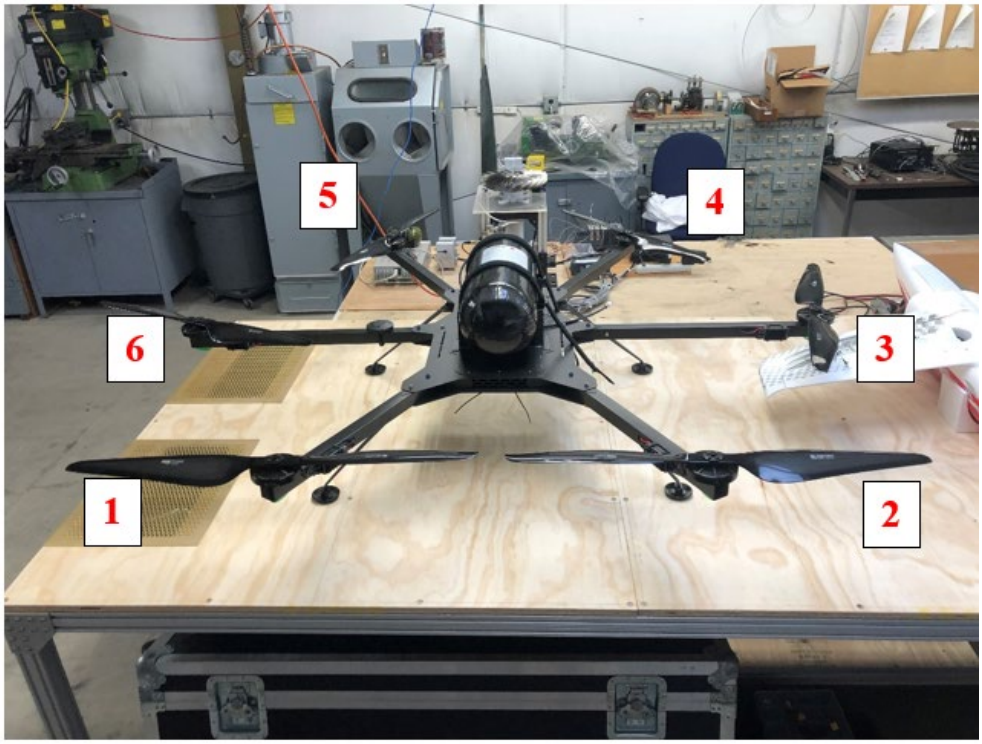

Figure 1. Current Hexacopter

These two sets of rotors will offset any induced torque allowing for stable hovering and flight. A helicopter's tail rotor not only serves as a stabilization mechanism, but also as the means for steering the helicopter. By altering individual blade speeds, which induces differential torques and lifting forces on the vehicle, a drone is able to alter its orientation. Altering multiple rotor speeds at one time allows for multiple maneuvers (roll, pitch, and yaw) to simultaneously occur. Copter drones present a more difficult engineering design challenge as multiple additional flight parameters are introduced into the design process. In order to have an efficient drone, it must be lightweight, stable, and have a low energy consumption rate.

2. Hover Efficiency

The autonomous vehicle industry has made significant technological advancements in drone performance in recent years. Due to these advancements, it is now economically feasible to purchase and integrate a fleet of drones into both private and public sector roles. Due to the increase in demand for drones, further specialization in drone design has been

undertaken to further improve performance. One area that has significant potential for improvement is drone energy efficiency. The efficiency of a drone is greatly dependent upon not only the environment within which it operates, but also highly influenced by the electrical and mechanical equipment used to control the drone. This study specifically quantifies the current hover efficiency of a hexacopter drone. Hover efficiency is quantified as the ratio of vehicle weight to the power necessary to maintain a hover and has units of kg/kW or lb/hp [2]. In order to directly influence the hover efficiency of a drone, two variables must be altered: the vehicle weight and/or the power required to hover. Variation in the mechanical components of the drone, (variation in energy consumption and conversion) specifically the airfoil and planform shapes of the rotor are shown to affect hover efficiency [3]. Variation in the electrical components also influence the hover efficiency, by tailoring the electrical equipment used to drive motors and propellers, minimizing electrical losses like internal resistances, component magnetism and internal eddy currents can increase the hover efficiency of a drone [4]. Increasing hover efficiency allows for more power to be extracted at the output state for the same amount of input power. Current research has recorded hover efficiencies as high as 55.5% [5]. Figure 2 shows a cross-flow fan drone in hover. By quantifying this metric, further research can be conducted into equipment alterations that would produce a net increase in the hover efficiency of the hexacopter drone.

Figure 2. Drone Hover during Test Flight. Source: [6].

More information with regard to both motor and ESC influence on hover efficiency and overall system efficiency can be found in Appendix A.

B. LITERATURE REVIEW

1. Open Flow Propeller Modeling

Modern numerical modelling software can solve a wide range of engineering problems that range from generation of in-depth fluid flow models through and around unique geometries to electromagnetic interferences experienced by electronic systems [7]. The foundational method by which the modelling software conducts these analyses is through use of CFD, computational fluid dynamics. CFD is an engineering tool that discretizes regions of interest in an engineering application and iteratively establishes equilibrium through each element within the domain. It is able to generate an approximate solution that will predict how a geometry will react to external forces, acoustic and vibrational interferences, and many other interactions [8]. The scope of CFD, and subsequently most engineering numerical modelling software, has yet to be constrained due to its ability to be applied to a wide variety of engineering and physics-based problems. Figure 3 shows a mesh used to discretize a generic airfoil.

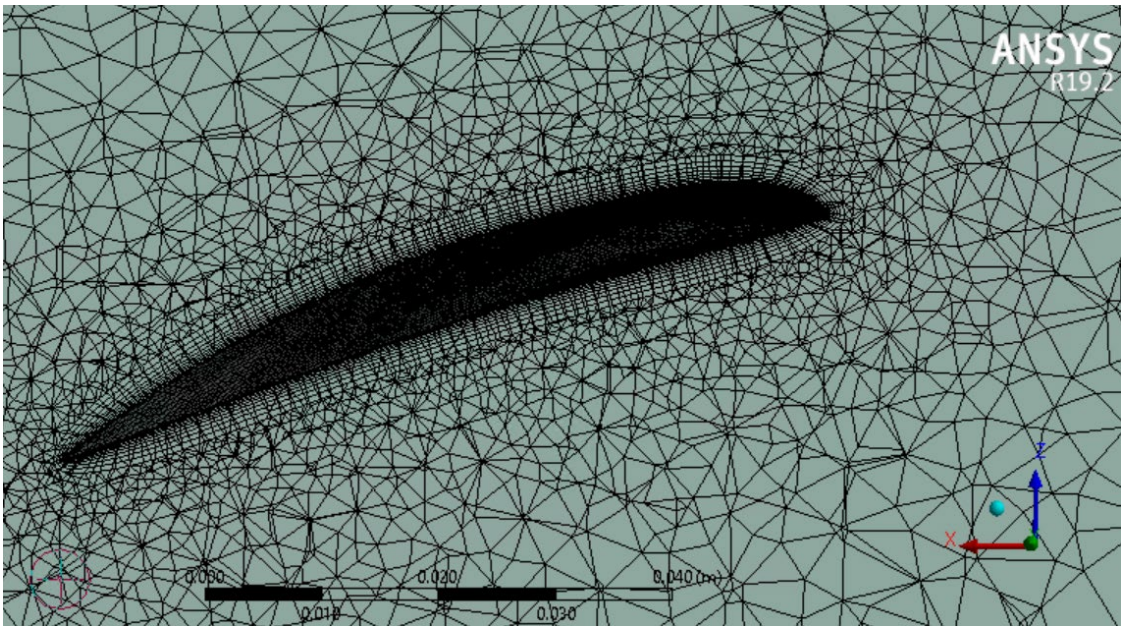

Figure 3. CFD Discretization of Airfoil

Far away from the object of interest it is seen that the mesh is coarse in comparison to the smooth inflation layers developed along the boundary of the airfoil. These inflation layers aid in the resolution of the fluid flow solutions near the surface of the airfoil where the behavior of the fluid is expected to be under different influences than regions removed from the surface of the airfoil. CFD can be a practical tool for engineering analysis when complex multi-dimensional solutions are required, however there is a tradeoff between solution resolution and computational time. If simpler models can be used to accurately approximate complex solutions, analysis time can be reduced which in turn will reduce costs and development time of engineering products.

When modeling an open flow propeller in three dimensions, simulation complexity is high and the analysis is time consuming. Published papers have documented simulation results with an accuracy within 15% of experimentally obtained metrics [9]. The most difficult phenomenon to capture when conducting open flow simulations is the wake generated by the blade as its behavior is transitory in nature [9]. When creating fluid control volumes around an open flow propeller, dimensioning is critical to numerical results. The blade model used in Yomchinda's [9] paper consists of a fluid domain with a diameter of four times the blade's diameter, while the domain diameter in Kutty and Rajendran's [10]

paper is only 1.1 blade diameters. The smaller domain is used to reduce the effects of pipe flow, specifically recirculating flow, on blade performance. Flow recirculation, similar to blade wakes, makes convergence difficult. Figure 4 shows the fluid domain used in Kutty and Rajendran's analysis.

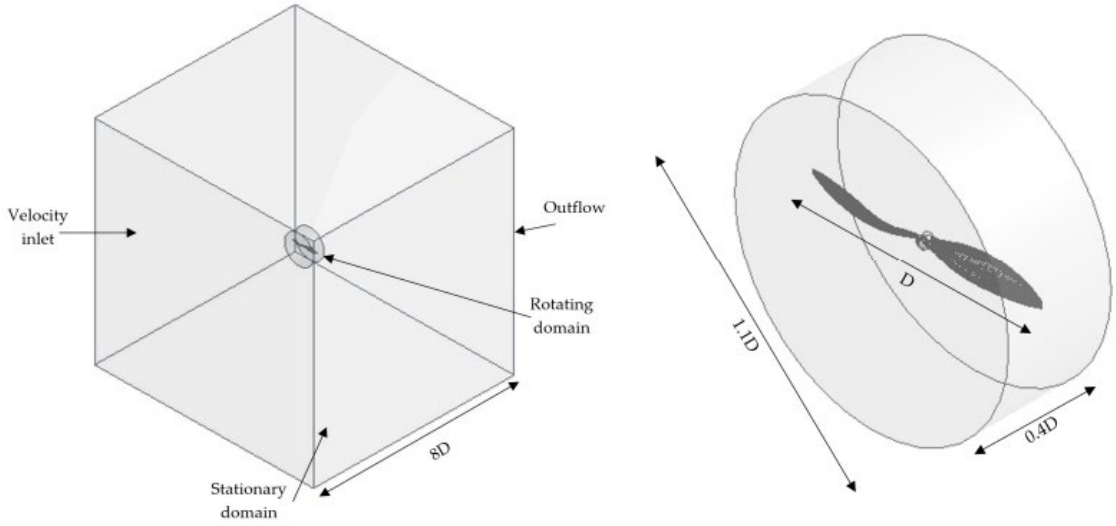

Figure 4. Fluid Domain for Open Flow. Source: [10].

As is seen, the domain is separated into two components, an inner domain that rotates and captures the minute details of fluid behavior immediately around the blade and attempts to filter out any recirculating flow, while the larger fluid domain sets up the general flow field. An expanded version of the inner fluid domain design will be used in this analysis.

Meshing tactics for open flow simulations are highly dependent upon the objective of the model. Coarse meshing is able to produce, with some degree of accuracy, metrics pertaining to lifting force and general velocity profiles upstream and downstream of a blade for relatively little computational power and time. Refining the mesh to decrease element size allows finer details to be assessed both near and away from the blade. This comes at a cost of computational time and its necessity is assessed on a case by case basis.

2. Actuator Disk Theory

Actuator Disk Theory is a method by which complex multi-dimensional fluid flow can be reduced to a simple two-dimensional fluid model. This model is constructed by replacing a rotor with a permeable disk and analyzing the fluid behavior across said disk [11]. The disk shape being analyzed is obtained from the planform area generated by a spinning rotor. Figure 5 shows a simple actuator disk theory model provided by the NASA Glenn Research Center.

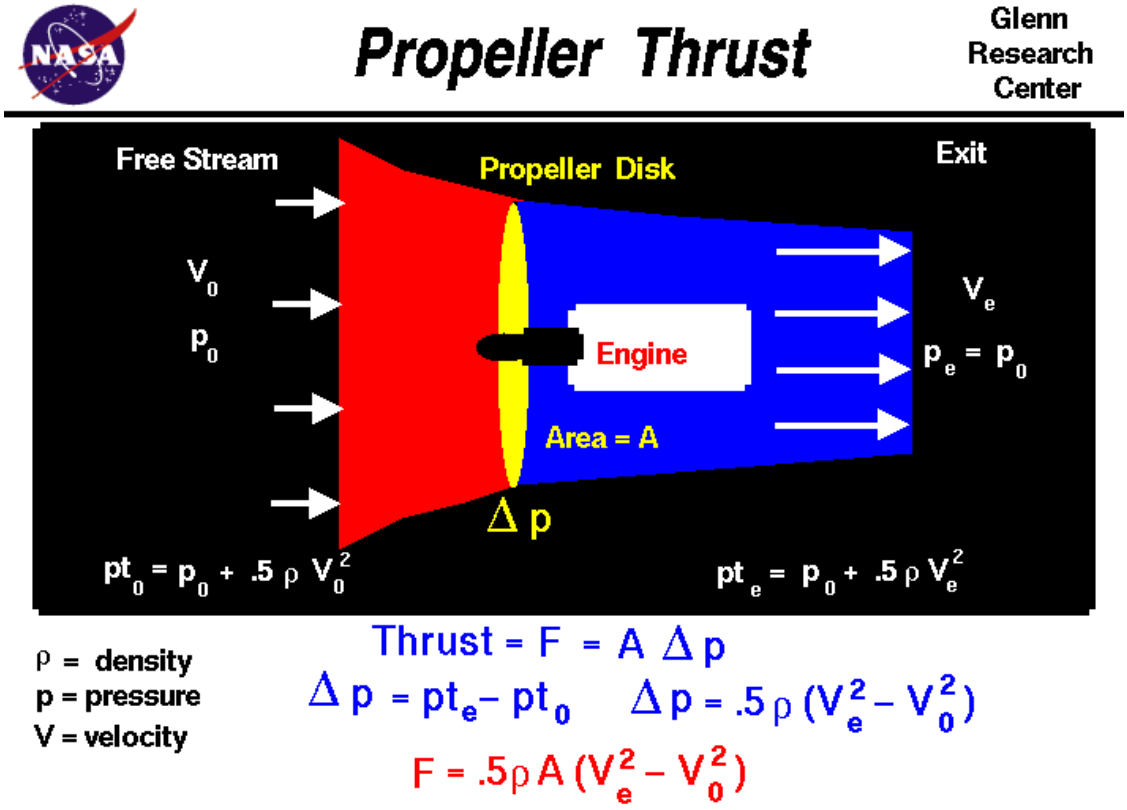

Figure 5. Actuator Disk Model. Source: [12].

By replacing the rotor with the respective disk area generated by its rotation, mathematical substitutions can be made to simplify analysis. As seen Figure 5, rather than performing complex integrals of pressures across a variable blade geometry, forces can be calculated knowing only the density, disk area, and velocity difference across the propeller

disk. Similarly, simple models can be generated by applying different pressures on each side of the blade to simulate thrust. The simplicity of this approximation has led to its repeated use for elementary modeling and simulations. Despite the Actuator Disk Theory's ability to estimate the performance of a rotor somewhat accurately, there are still shortcomings associated with this model and its assumptions [13]. The reason that the Actuator Disk Theory is preferred over complex multi-dimensional models are its baseline assumptions, which greatly reduce the computational time of simulations. These assumptions, however, are what lead Actuator Disk Theory to be less accurate than multi-dimensional models. The Actuator Disk Theory fails to provide a relationship between the unique blade geometry and the blade's performance characteristics like torque and thrust [13]. The rotational and linear forces are instead related to the disk area of the blade. When averaging pressure forces and velocity profiles across the rotor, inaccuracies are created as these forces do not assume the average value across the disk radii. The pressure forces and velocity profiles are more accurately modeled by polynomial functions, something that this theory does not account for. An additional shortcoming of the Actuator Disk Theory is the inability to model the induced velocity field generated on the trailing edge of the disk [11]. Despite these shortcomings, reasonable fluid models are able to be generated using the Actuator Disk Theory. With further analysis into the true velocity and pressure profiles across a rotor, this simple model can be improved to provide results with increased accuracy which would allow for a computationally cheap model to be used for complex analysis.

C. OBJECTIVES

There are two primary objectives for this project. The first is to provide a computationally expensive numerical model and analysis of fluid flow over a remote-control (RC) drone blade that will aid in validating actuator disk theory analysis. If the actuator disk theory is seen to produce comparable results to three-dimensional fluid flow analysis, the second objective then is to provide the computationally simple analytical method with fluid flow performance data so that it can be used in replacement of complex three-dimensional fluid flow models. The results produced will themselves be compared

to experimental data collected on a test stand mounted blade in a lab setting to ensure their validity.

D. THESIS OUTLINE

Chapter II contains all information with regards to numerical modeling. This includes information regarding critical inputs for simulation success (blade speed and meshing guidance), as well as results, differences, and analysis for two models, pipe flow and open flow.

Chapter III contains all experimental data acquired that is subsequently used to validate the previous section's results and focuses on the acquisition process and analysis of the raw experimental data. Multiple different experimental methods are used to obtain necessary data to include: hovering a hexacopter drone and acquiring real time data, specifically energy consumption rates and torques, and test stand data to provide lifting forces and torques on a single blade.

Chapter IV is dedicated to comparing and validating the numerical results via comparing them to the experimental data. Plots, figures, and tables are used to convey the accuracy and similarity between the two independently obtained data set.

Chapter V focuses on refining the assumptions of Actuator Disk Theory by implementing radial pressure and velocity distribution curves as well as the sectional lift coefficient along a rotor blade. These distribution curves and lifting coefficients are obtained from the numerical and experimental modeling discussed in Chapters II and III.

THIS PAGE INTENTIONALLY LEFT BLANK

II. NUMERICAL MODELING

A. BLADE MODEL AND ROTATIONAL SPEED CALCULATION

The rotational velocity at which the blades spin must be known for an accurate analysis, the hexacopter drone was connected to a sensor which was subsequently connect to an oscilloscope and hovered until a steady state measurement of the electrical frequency could be obtained. Then, using a simple conversion of 1 Hertz being equivalent to 60RPM, the blade speed in RPM could be determined. The measured frequency of the hexacopter drone in hover was 30Hz, which yielded a blade speed of 1800RPM. This blade speed is a required input for the "Setup" step in the numerical modelling software.

B. SIMULATION MODEL

1. Model Inspection

A complete layout of the blade model used in this simulation can be found in Appendix E. Prior to constructing fluid domains, inspection of the blade model is done to identify inconsistencies between the physical rotor and model rotor, if any. Figure 6 shows a frontal perspective of the blade model's profile.

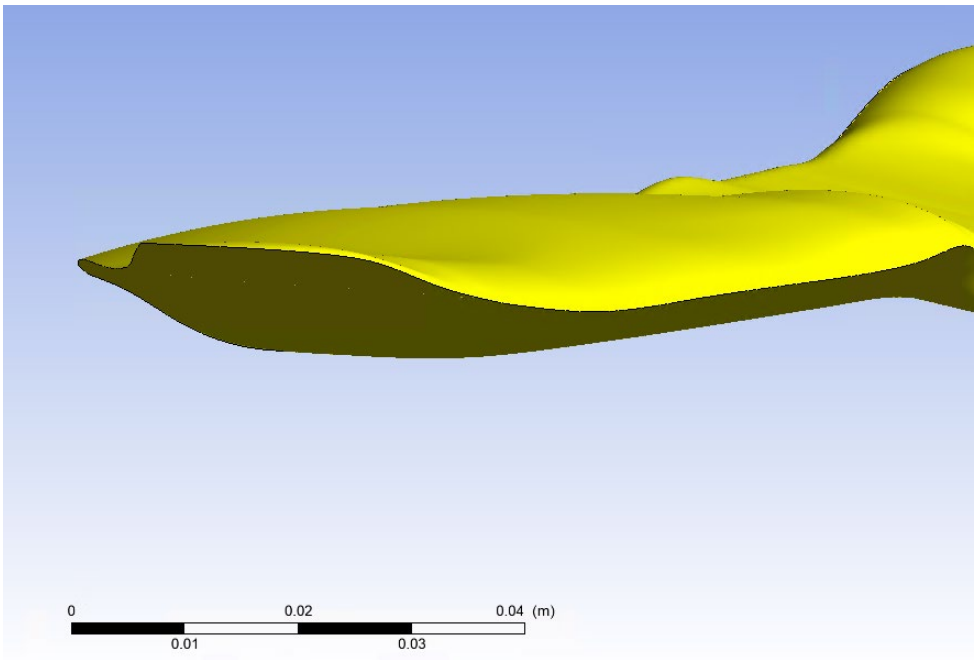

Figure 6. Selected Blade Tip Geometry

Two unexpected design characteristics are seen in this model. The first pertains to the behavior of the airfoil at the tip of the blade, and the second with regards to the leading edge of the blade. At the blade tip, which matched the physical rotor, the end pitches up as seen in Figure 6. Although not advertised, based on this design it is suspected that T-motor, the manufacturer of this blade, designed it for performance rather than endurance. The suspected reason for the blade flaring at the end is to allow for quieter flight by augmenting the behavior of the tip vortex generated by this rotor. A blade designed for maximum endurance would be made in such a way as to utilize the entire blade for lifting. A maximum endurance rotor would prevent the tip vortex from disturbing upstream flow. The second unexpected design characteristic which is a source of inaccuracy in the blade modeling is present along the leading edge of the blade, which is sharp. Subsonic airfoil designs focus on having smooth profiles rather than ones with sharp edges. This is especially important for leading edges, where the location of the stagnation point has a major effect on the downstream fluid behavior. For the real blade, an elliptical shape is seen at the leading edge of the airfoil, where in the Figure 6 model, the top and bottom surface are separated by the sharp leading edge. Due to this, inaccuracies will arise in the

simulation fidelity due to the discrepancy between the true and modeled leading edge of the airfoil. The blade tip flare is an incorporated feature of the blade design and thus, focus on the model fidelity and fluid behavior in this region will be emphasized in the setup. Simulation setup will continue with the blade model shown in Figure 6 with the identified inconsistency (sharp leading edge) and unexpected geometry (tip flare).

2. Fluid Domain Construction

Figure 7 shows the two fluid domains used in this analysis. A more complete discussion on the fluid domain's construction can be found in Appendix E.

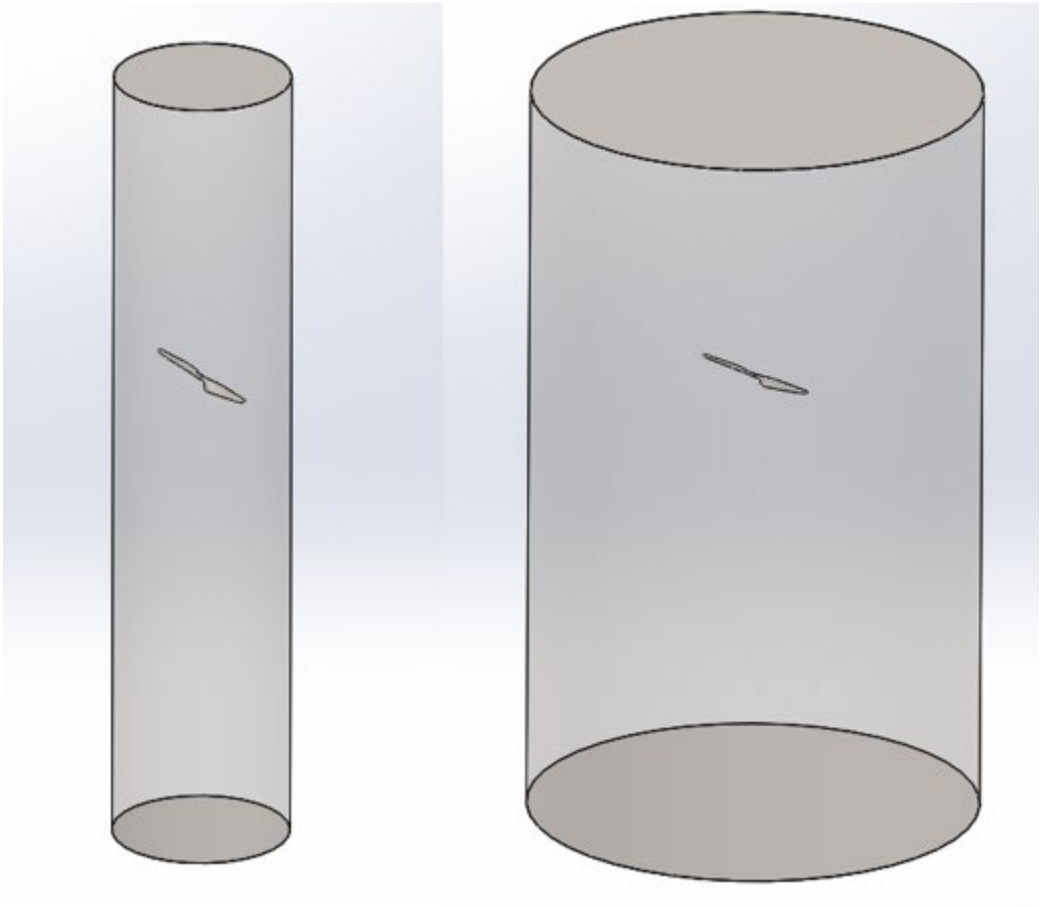

Figure 7. Pipe Flow and Open Flow Fluid Domains

In Figure 7, the blade is actually negative space within the cylindrical control volume. All geometric references will be made with respect to the blade radius of 355 millimeters due to the symmetry of the fluid domain. Due to the natural difficulty of modeling three-dimensional fluid flow over a rotating domain, a single fluid domain is generated for each simulation to reduce the complexity of the analysis. More discussion on common errors and methods to overcome these errors can be found in Appendix G. The fluid domain used in the pipe flow simulations is a full-cylinder body enclosing the blade with a radius 1.1 times that of the blade radius. For the open flow case, a cylinder of 3.0 times the blade radius is used. Table 1, shows the dimension of each fluid domain in millimeters.

Table 1. Fluid Domain Dimensions

	Radius (mm)	**Upward extrusion (mm)**	**Downward Extrusion (mm)**
Blade Dimensions	355	-	-
Pipe Flow Fluid Domain	391	1422	2133
Open Flow Fluid Domain	1065	1422	2133

To focus simulation fidelity around key areas of the model, targeted meshing is done around the region of the fluid domain surrounding the blade. Face sizing is implemented on the blade face to increase the resolution of the solution on the blade. This face sizing results in the fluid's behavior and interaction with the blade surface being more accurately portrayed in the numerical model. Inflation layers stemming from the blade surface are the next compliment to this face sizing. Inflation layers are inserted in order to capture the boundary layer behavior of the fluid as the distance from the blade grows. The 7 implemented inflation layers are setup to have a total thickness of only 2 millimeters to prevent deformation as they wrap around the leading, trailing, and tip edges of the blade. Figure 8 shows the results of the boundary layer and inflation layer implementation.

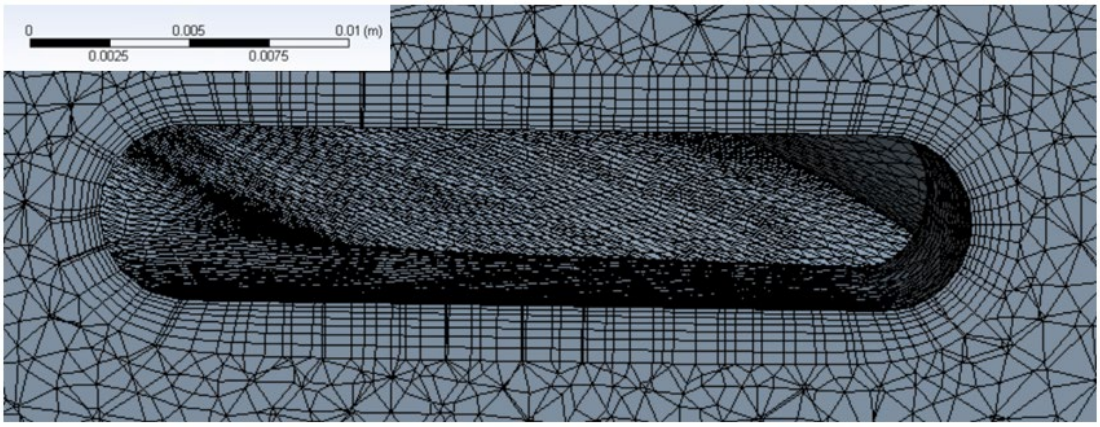

Figure 8. Body Sizing and Inflation Layers

The generation of wakes and vortices off of the trailing edge of rotors, especially at the blade tip, affect the lifting ability of the blade. These vortices produce downwash behind the blade and result in lower lifting forces. In order to compensate for the reduced forces from trailing vortices, the wing must have a steeper angle of attack to generate the additional lift necessary to neutralize the loss in lift. Accurate capturing of the blade vortex is imperative for an accurate simulation and characterization of the lifting characteristics of a blade at a specified rotational speed. These vortices are not contained within the region emphasized by the previously implemented blade face sizing and inflation layers. Thus, implementation of two spheres of influence is done at the blade tips to produce fine mesh within the region of influence surrounding the blade tips only. This is done in lieu of employing a body sizing method over the fluid domain in order to save computational time. Figure 9 shows the results of the sphere of influence over a single blade tip.

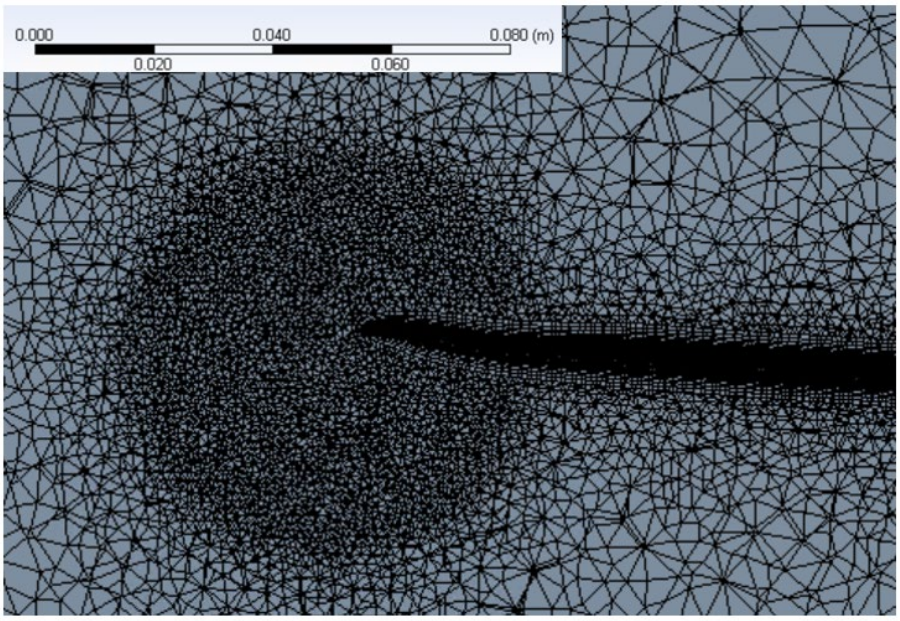

Figure 9. Blade Tip SOI

By imposing two spheres of influence each with radius 3 centimeters and a cell body size of 1 millimeter, the trailing vortices generated by the blade tips can be accurately captured without greatly increasing the computational time of the model. Related to this logic, body sizing is not done on the fluid volume for two reasons, one of which is discussed earlier. The second reason being it is unnecessary to have body sizing. The fluid behavior far away from the blade will remain unaffected on a local scale by what happens at the blade. That is, there will be no vortices or boundary layers generated upstream or downstream of the blade. Instead, on the upstream side of the blade, flow is expected to be parallel to the axis of rotation of the blade as it is entrained by the rotor. As the flow accelerates toward the blade it will constrict forming an hourglass shape. Even at this point, the flow will remain relatively uniform, within the resolution of the cell's default body size in the upstream fluid domain. As the flow comes into contact with the blade and blade tips, this is where the specific mesh manipulation is implemented and should allow for the minute details on, across, and immediately following the blade to be captured. Downstream of the blade the flow will become swirled due to work imparted on it by the blade. This swirl, as with the upstream fluid, will be uniform and should be locally resolved by the default body sizing downstream of the blade.

3. Stability Measures

Before setting a rotational speed for the blade, it is necessary to impose an initial flow through the fluid domain. A fluid velocity of 1 m/s is imposed to enter perpendicular to the fluid domain inlet, and exit perpendicular to the outlet. Figure 10 shows the resulting flow field after the 1 m/s flow converges.

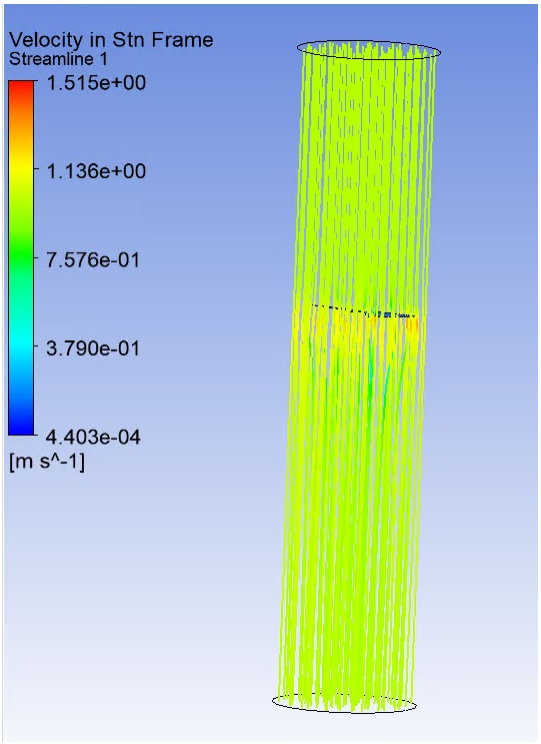

Figure 10. 1 m/s Imposed Flow Visualization

This configuration initializes the flow field throughout the fluid domain and additionally aids in stabilizing the simulation at the beginning stages when the fluid domain is first given a rotational velocity. As no work is being imparted on the fluid by the blade, the residuals of the flow field quickly converge to a steady state value (<100 iterations). The only disturbance of the flow field comes from the fluid being displaced by the currently stationary blade. Following the convergence of the initialization field, it is necessary to incrementally increase the rotational velocity of the blade rather than immediately setting the speed to 1800RPM. When the blade speed is immediately set to 1800RPM in the

initialization process the flow becomes separated from the surface of the blade and the resultant lifting forces in these simulations are less than half of the expected value. The rotor stalls in these situations and stirs the flow rather than generates lift with it. Table 2 shows the increments at which the rotational velocity of the blade is increased throughout both the pipe flow and open flow simulations.

Table 2. Rotational Velocity Step Size

RPM (Pipe Flow)	**RPM (Open Flow)**
80	80
120	120
-	300
450	425
	575
-	725
-	875
1100	1025
	1175
-	1325
-	1475
-	1625
1800	1800

Discretion is used when determining the step size increase of the blade speed seen in Table 2. If the blade speed is increased too much between steps, the flow separates. In this case the simulation needs to begin again from the previous stable simulation solution. The criteria necessary to increase the speed to the next level requires that the residuals and in particular, the lifting force, reach steady state. For this simulation, once the lifting force reaches a steady state, the iterative process is continued until the mass and momentum residuals converge to an acceptable value (greater than three orders of magnitude lower than their beginning value). Appendix F contains the remaining information on the simulation model for this analysis. When the simulation is run, but the lifting force not allowed to reach steady state, the simulation will break. The flow detaches and becomes unstable, resulting in a failed simulation. The simulation is a steady state analysis as

opposed to transient analysis. When the initial or boundary conditions are changed in the simulation, these changes have to be given computational time to propagate through the flow field. The speed varying effects on the mass and momentum residuals are displayed in Figure 11 for the pipe flow simulation to illustrate this point.

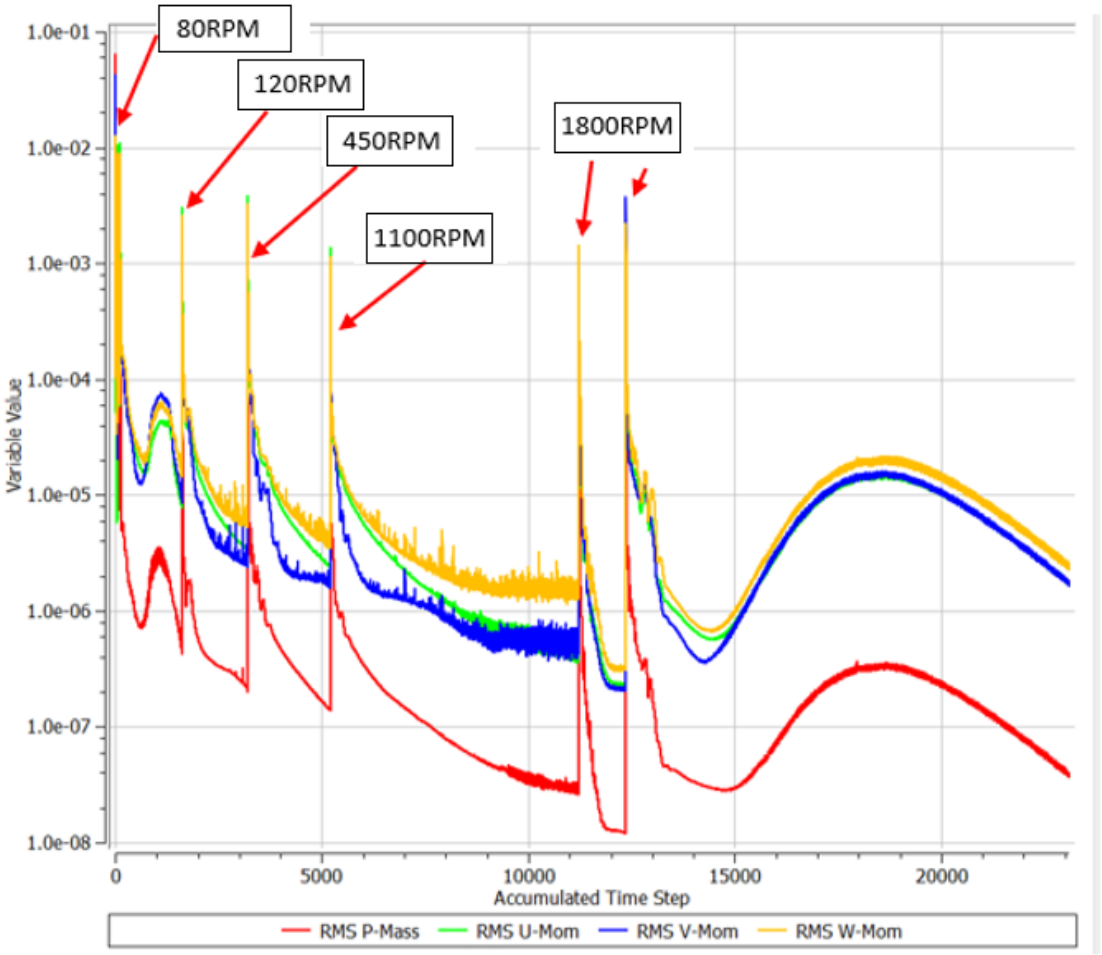

Figure 11. Mass and Momentum Residuals Pipe Flow

Figure 11 shows that after each RPM step there is an initial spike in the residual value followed by a general decay toward zero as iterations reduce errors in the numerical model. The residual plot for the open flow simulation has a similar trend and can be found in Appendix F. As is seen in Table 2, the step size between iterations depends on the stability of the simulation. The pipe flow simulation is far more stable in comparison to the

open flow simulation and thus, larger step sizes can be taken between iterations. The more complex the simulation, the larger number of iterations required for the altered flow conditions to diffuse through the entire fluid domain, increasing the computational time of the simulation. Simulation complexity is caused by the problem being difficult in nature, or, for example, due to open ended boundary and initial conditions which then lead the simulation spending computational time on solving these ambiguous settings.

C. PIPE FLOW SIMULATION RESULTS

Additional information about the pipe flow residuals can be found in Appendix F. The major properties of concern for this study are the force and torque generated by the blade. Over the course of the pipe flow simulation, over 23000 iterations were completed. The pipe flow fluid domain geometry is stable as the control volume is relatively small and uncomplex. When increasing the pipe diameter in later studies, more iterations and smaller speed increases are seen to be required as stable conditions are more difficult to maintain. The non-linear growth in the magnitude of force and torque between 3000 and 10000 iterations in Figure 12 and Figure 13 can be attributed to each increase in blade speed as the simulation progressed. Before increasing the rotational speed, each "step" is iterated until relative steady state is achieved. In quasi-steady state what is desired is a controlled but decaying increase (non-oscillatory) of the lifting force. Once the force and torque begin to level out, the simulation is stopped and the speed of the blade increased. As is seen in Figure 12 and Figure 13 the force and torque at 1800RPM reach a steady state value after approximately 16000 iterations. The remaining 7000 iterations allow for minor details in the simulation boundary conditions to be resolved. The changes after 16000 iterations have little effect on the blade's lifting force or moment.

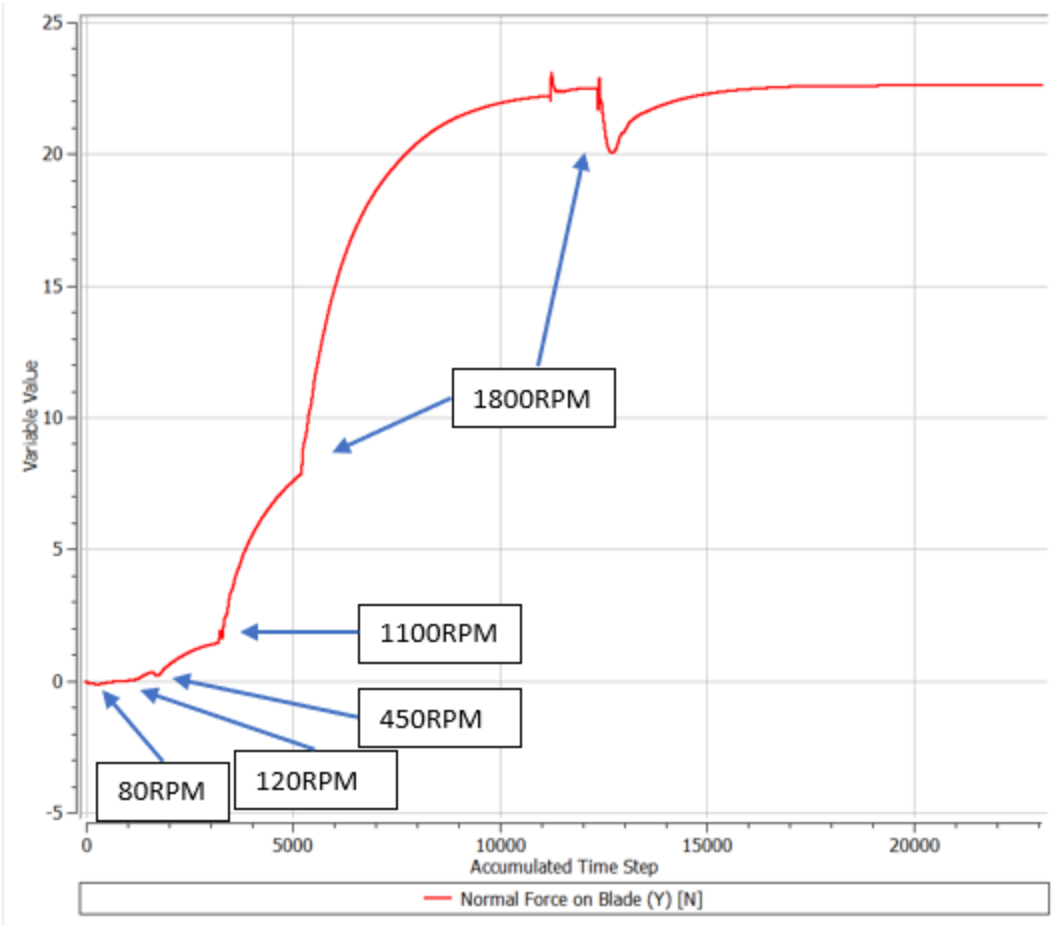

Figure 12. Normal Force, Pipe Flow

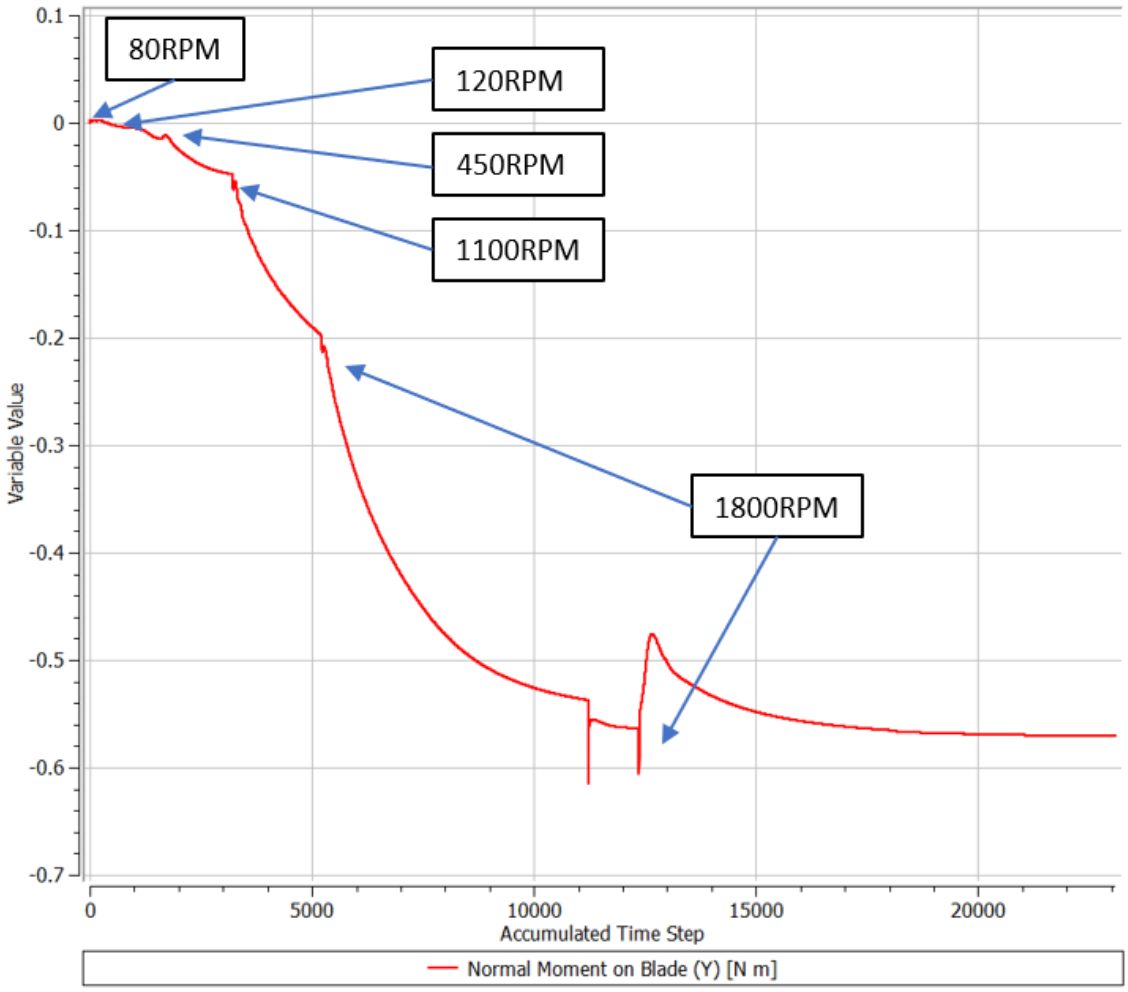

Figure 13. Torque, Pipe Flow

Despite the simulated force and torque value being in steady state, the simulation continued to iterate in order to reduce the residual's magnitude. This aids in ensuring that the flow field is fully developed throughout the entire fluid domain. The final steady state force as predicted by the pipe flow simulation is found to be 22.59N and the torque is 0.5903Nm. The flow field shown around the blade in Figure 14 is accurate for a flow field of air being entrained through a pipe by a blade.

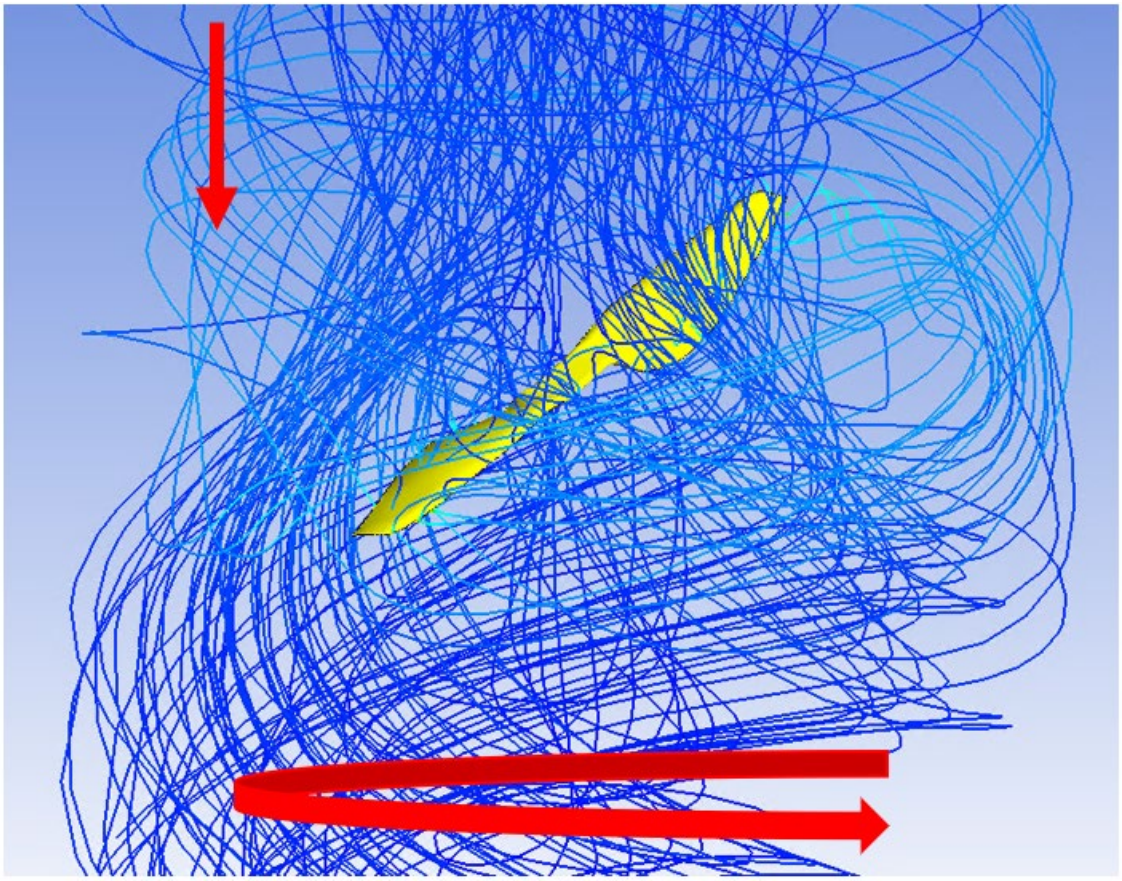

Figure 14. Flow Field, Pipe Flow

The streamlines enter the confines of the pipe and maintain parallelism to the walls of the pipe. As they approach the blade, the flow accelerates due to being entrained by the blade as well as due to the work imparted on the air across and beneath the blade. This acceleration leads to a rise in the dynamic pressure. This is seen at the top of Figure 14 where the pressure change causes the flow to constrict slightly prior to and immediately over the blade. The flow exits swirled due to drag as depicted by the arrows in Figure 14. As the flow begins to decelerate its static pressure returns to a value comparable to the inlet static pressure. Visually, the flow field over the blade seen in Figure 14 behaves as expected, the flow is parallel to the axis of rotation above the blade and swirled flow leaves the blade below, but verifying and quantifying the accuracy of the fluid properties passing over the blade as produced by this mesh must be analytically inspected.

A common metric used to determine the accuracy of the fluid flow over objects in relation to the meshing of the blade is the y-plus value. This is a non-dimensional metric that gives insight to the mesh quality for a particular simulation and its value is shown in Equation 1.

$$y^{+} = \frac{y}{\upsilon}\sqrt{\frac{\tau_{\omega}}{\rho}} \tag{1}$$

The value of y-plus is equivalent to the distance away from the wall, y, the kinematic viscosity, υ, and ρ and τ_{ω} the fluid density and shear stress at the wall [14]. The lower the value over the blade, the more suitable the meshing is, and vice versa. Figure 15 shows the contour of y-plus values over the top blade and Figure 16 shows the contour over the bottom surface of the blade.

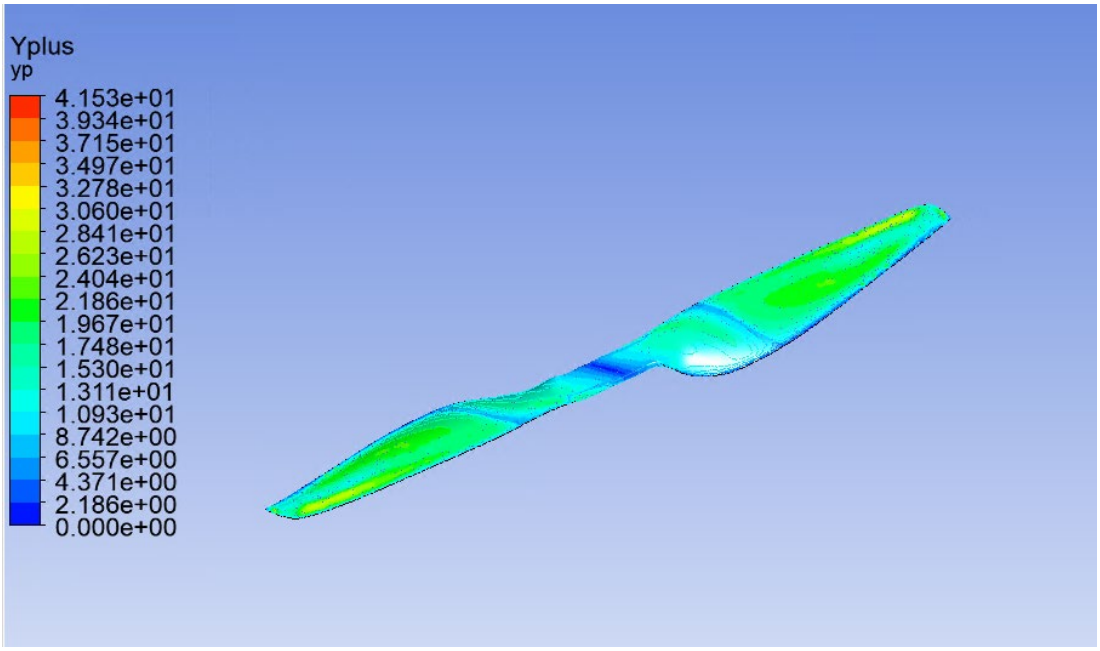

Figure 15. Y-plus Contour Top, Pipe Flow

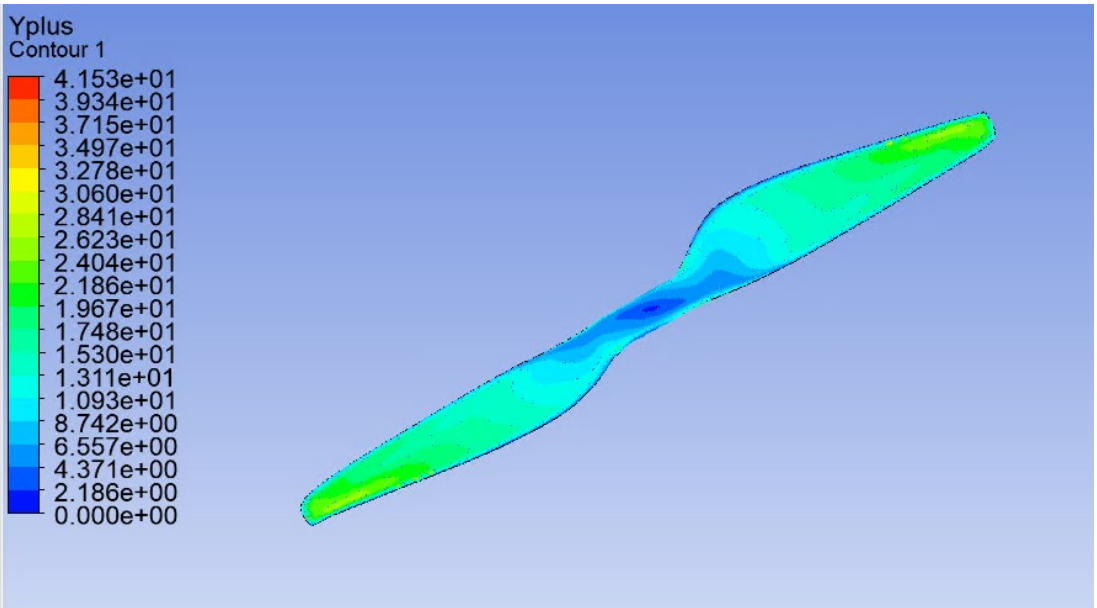

Figure 16. Y-Plus Contour Bottom, Pipe Flow

The y-plus value over the blade ranges from a minimum of approximately 0 to a maximum of 30 when reading the contour legend. The lowest values occur over the hub of the blade which is logical as the fluid over this portion of the blade is moving the slowest as well as not being used to generate lift. The highest y-plus values occur at the leading edge on the upper surface and the trailing edge of the bottom surface. This is because this is where the most extreme changes in fluid behavior are occurring. The highest pressure and velocity differences occur at the leading edge of the blade on the upper surface. These y-plus values are within an order of magnitude of an ideal simulation, which would have values under 10. With a maximum y-plus value of near 30 and an average over both surfaces of 15–20, the meshing quality can be deemed acceptable for this simulation. The face sizing and boundary layers imposed during the meshing phase aid in simulating an accurate flow field immediately over the blade tip. The next component of meshing and its influence on the solution to be inspected are the spheres of influence that are placed over each of the blade tips.

The purpose of the sphere of influence implementation is to help accurately capture the vortex coming off the tip of the blade. Figure 17 shows the produced tip vortex.

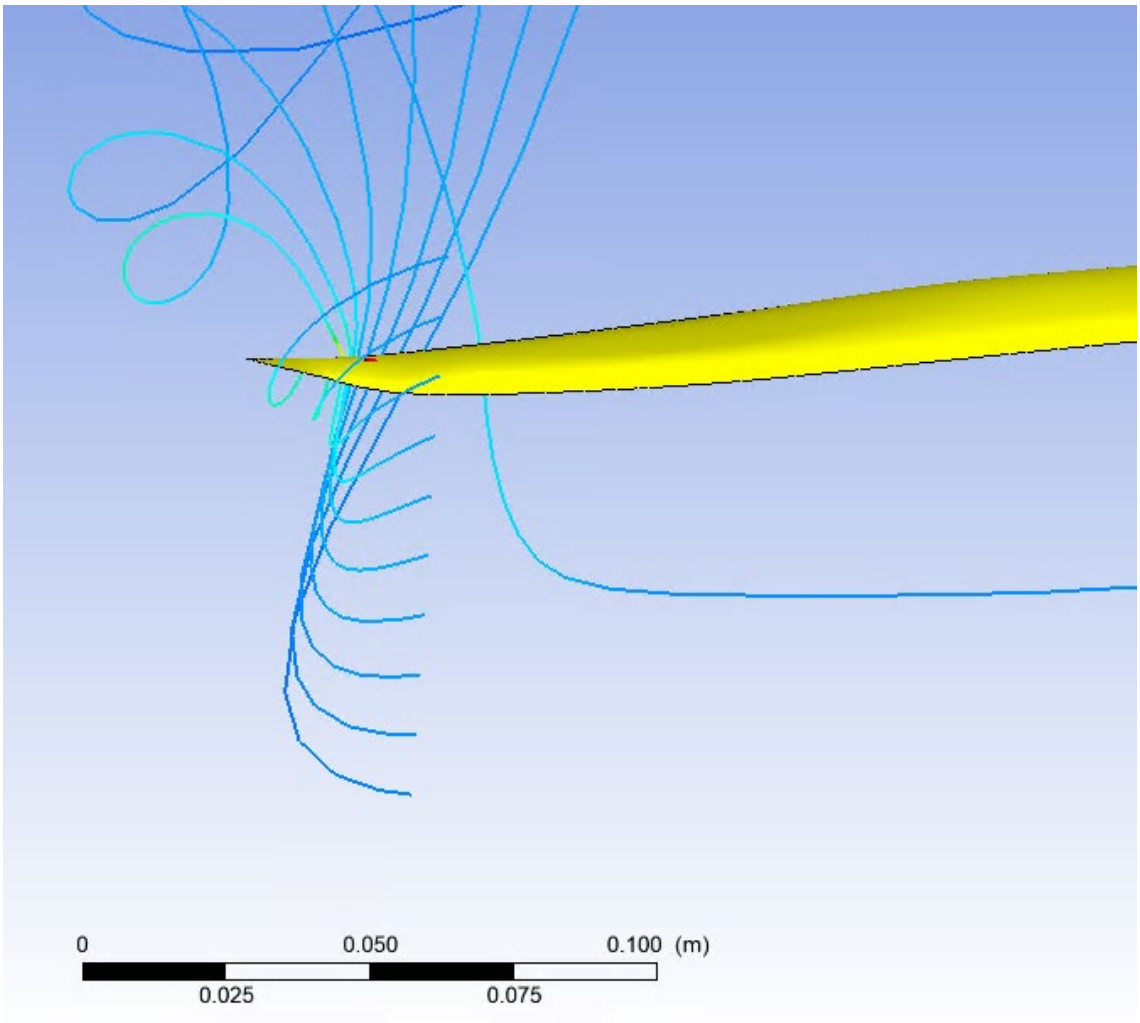

Figure 17. Tip Vortex

When inspecting the tip vortex generated by the spinning blade in Figure 17, it is seen that the behavior immediately following the blade pass is as expected. The flow begins to turn on itself and is displayed as a swirl on the trailing edge of the blade. The resolution of the simulation is due to the spheres of influence and their placement at the blade tips. Adding the spheres of influence did not affect the steady state force or torque values as predicted by the simulation. Their presence did increase simulation fidelity, however. This is seen in Figure 11 by the residuals steadily declining at the end of the simulation. The final product, shown in Figure 17 contains a neater, more fully developed swirl coming off the blade tip.

Despite producing what is locally expected with respect to tip vortices, Figure 18 shows a more global view of the fluid behavior. What is unusual and unexpected in this figure is the vortex streamline continues on the same circumferential path that the blade does until it is intercepted by the leading edge of the second half-rotor. This contact with the revolving rotor deflects the wake streamlines upward.

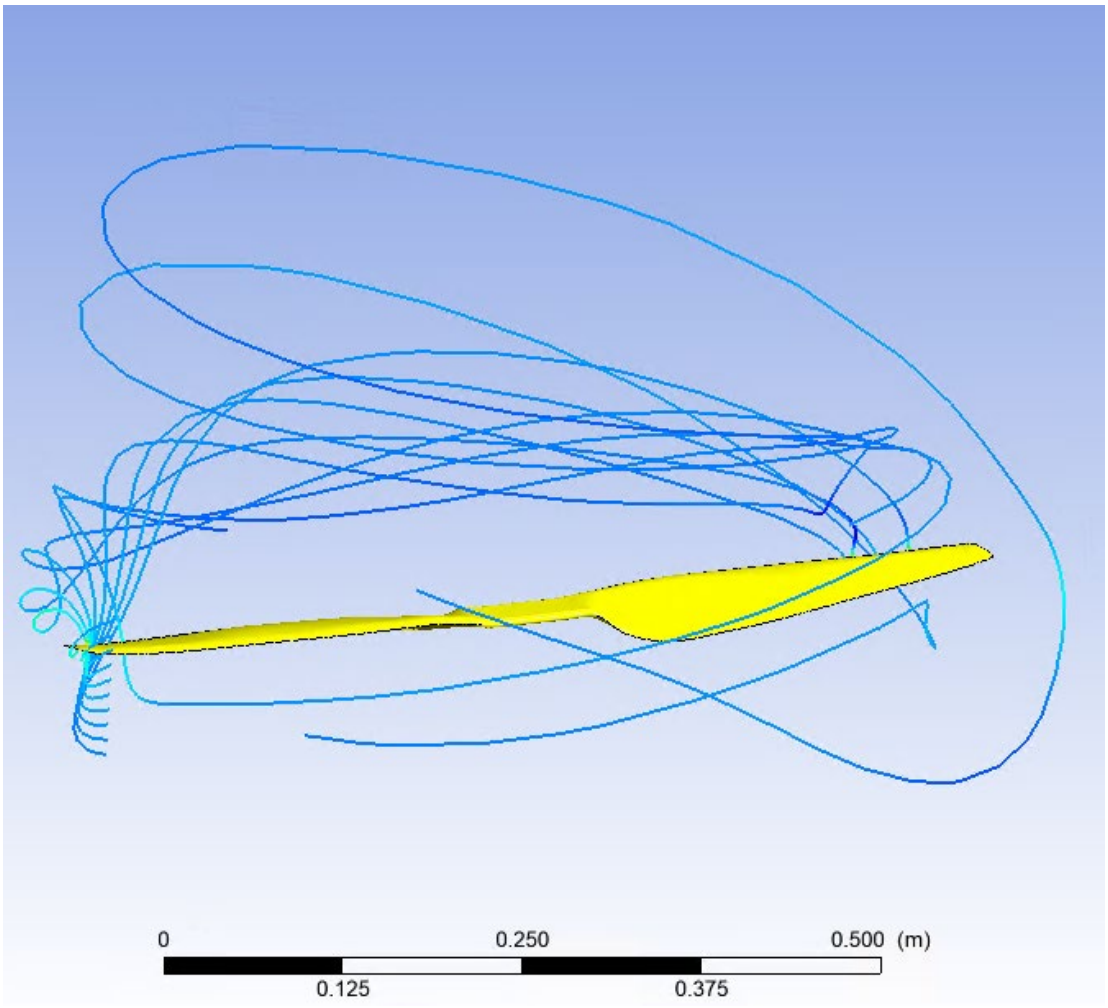

Figure 18. Tip Vortex Global Behavior

Vortices are typically forced down following their shedding from the blade, however the geometry of the airfoil, as shown in Figure 6, has a blade that kicks up at the blade tip, which causes the vortex, instead of moving downward with the rest of the flow, to remain on the same plane as the rotor. The incoming fluid from above prevents the vortex

from rising (which is what the pitched blade tip causes the fluid to do in an ideal encounter) allowing it to come into contact with the second rotor. Although not resulting in any major disturbances in the upstream flow field, the trailing vortex being scattered vertically does appear to disrupt the flow over the outer radii of the blade. This is seen in Figure 14 which shows minimal flow passing over the outer half of the blade while the core flow remains unaffected. This behavior is unexpected for most airfoils, however, upon further inspection of the blade geometry and the resulting force and torque generated matching the experimental values, an understanding of the fluid flow field in relation to the blade geometry is reached.

Figure 19 shows the velocity gradient over the chord length of the blade at a radius of 200mm, a central radial value, and 340mm, at the outer radii.

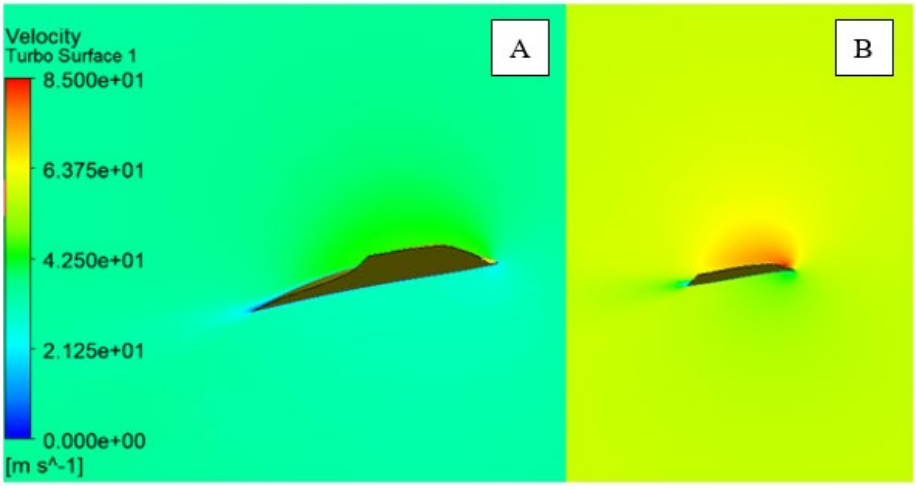

Figure 19. Velocity Distribution at Radii of 200mm (A) and 340mm (B), Pipe Flow

As is seen, the magnitude of velocity is higher over the outer radius of the blade due to having a higher linear velocity, despite having the same rotational velocity. However, the velocity contour over the blade at 200mm is more developed and attached than at 340mm. The trailing edge of the 200mm radius chord shows a thin and developed boundary layer attached to the blade while at 340mm, the velocity gradient shows signs of becoming detached at the trailing edge. The outer radii being more near separation is due

to the blade pitching up as it nears the tip. This non-uniform velocity over the surface of the blade has severe implications for blade performance at that location.

Figure 20 shows the pressure profiles over the chordwise section of the blade located at a radius of 200mm and 340mm from the center of the blade's hub.

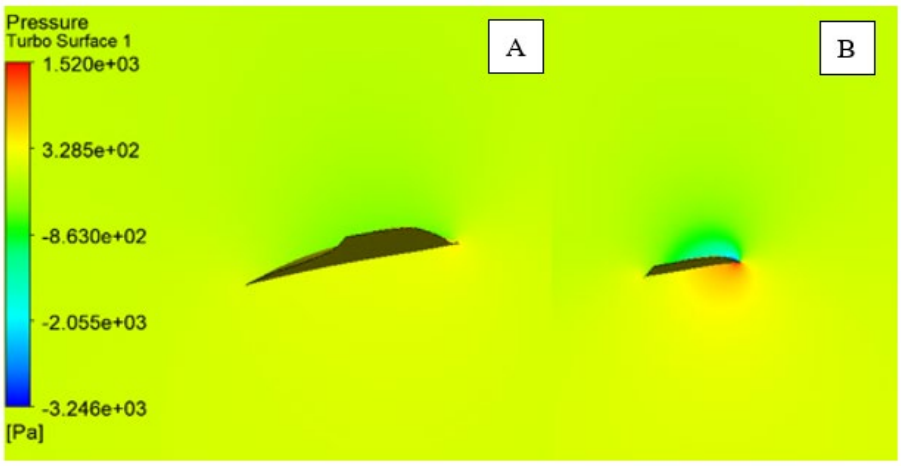

Figure 20. Pressure Distribution at Radii of 200mm (A) and 340mm (B), Pipe Flow

The magnitude of pressures shown in Figure 20 are higher at the outer radius due to the rotation of the blade. However, as seen, the pressure gradient over the more centrally located radius is more uniform over the chord of the blade, and the chord length at 200mm is over double that at 340mm (65mm vs 30mm). Taking these facts into consideration, the lifting force generated is expected to be higher over the blade at 200mm than at 340mm.

Radial pressure and velocity gradients as well as the lift coefficient along the rotor's span will be extracted from these results and have two primary functions. The first being to prove that bulk lifting force generated is at the inner radius locations of the blade and the second is to take these gradient curves and use them for an actuator disk theory simulation to further increase the fidelity of that modelling convention.

D. OPEN FLOW SIMULATION RESULTS

Appendix F contains additional information regarding the open flow simulation setup. Similar to the pipe flow simulation, the force residuals need to reach a quasi-steady state prior to increasing the rotational velocity of the fluid domain. By modelling a wider fluid domain, a more complex flow field is generated due to fluid being able to be deflected away from the blade. There is more open space through which the fluid is able to pass in the open flow simulation in comparison to the closed flow simulation where nearly all fluid mass is forced to pass across the blade. These differences in fluid domain dimensions necessitate much higher simulation times for the open flow simulation in comparison to the pipe flow simulation. Thus, in comparison to the 1500–5000 iterations required to converge for pipe flow, 10000+ iterations are required for open flow. The computational time between each speed increase varies, but is on the magnitude of days for each increment.

Additional differences observed between the pipe flow and open flow simulations are in the behavior of the force plot. The force growth between speed increase intervals can be seen in Figure 21.

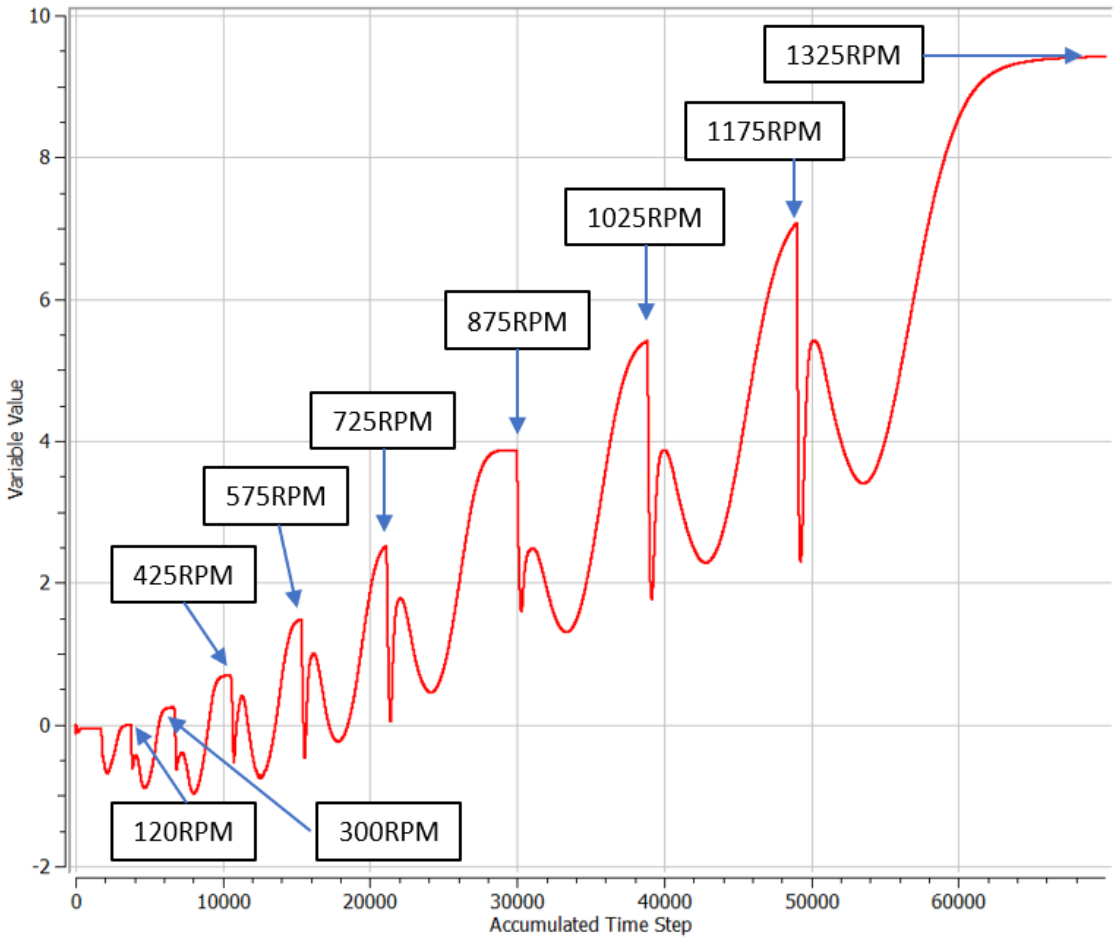

Figure 21. Normal Force, Open Flow

The steady state force achieved at a blade speed of 1325RPM is 9.45N. In order to obtain an accurate estimation of the output force at 1800RPM, scaling is done with previously known lift and speed data points using a modified version of the Affinity Laws for Pumps and Fans, seen in Equations 2, 3, and 4 [15].

$$\frac{Q_1}{Q_2} = \left(\frac{N_1}{N_2}\right) \tag{2}$$

$$\frac{F_1}{F_2} = \left(\frac{N_1}{N_2}\right)^2 \tag{3}$$

$$\frac{P_1}{P_2} = \left(\frac{N_1}{N_2}\right)^3 \tag{4}$$

Q represents the flow rate, F represents the force, P is the power, and N signifies speed. The equation used in this analysis is Equation 3. As is seen, the squared component on the right is the ratio of speeds while the ratio on the left is that of the known and expected force value. The ratio of force is related to the ratio of the corresponding speeds squared. It is expected that as the force is scaled to higher velocities, the growth will be quadratic. The force exerted on the blade at 1800RPM obtained from scaling the results at 1325RPM is 17.44N.

The behavior of the torque can be seen in Figure 22.

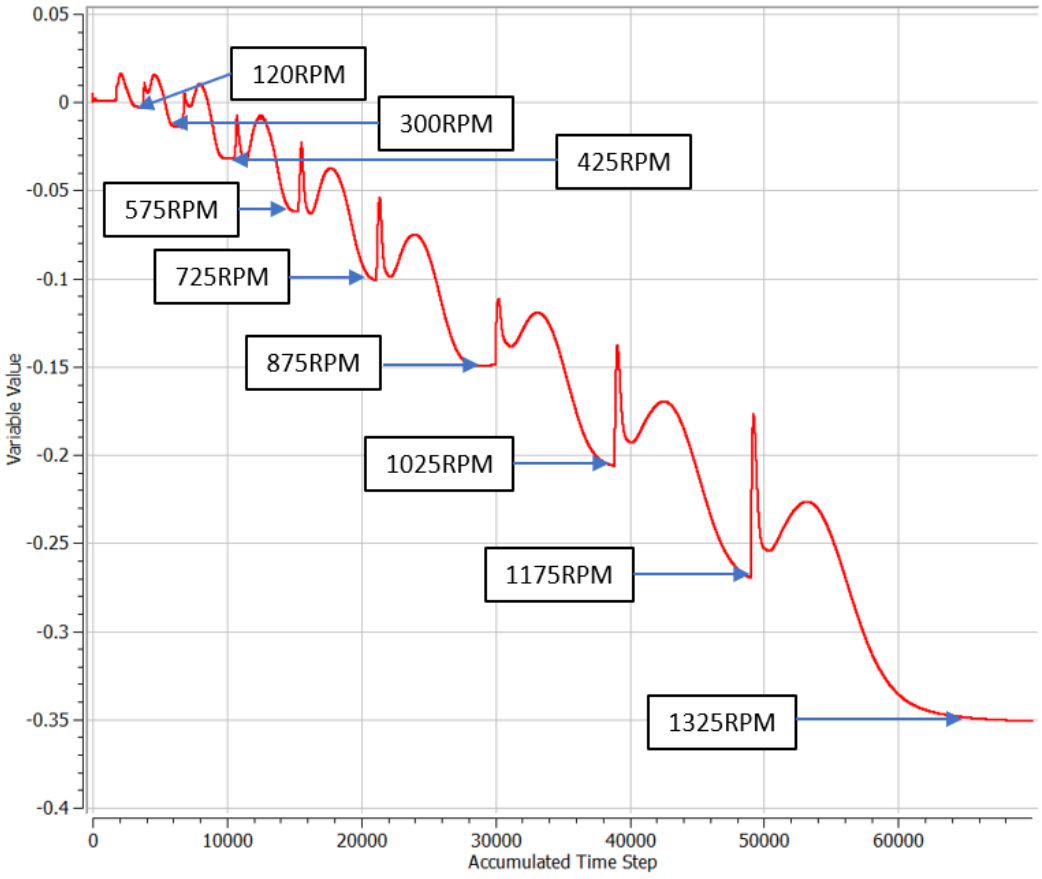

Figure 22. Torque, Open Flow

As is seen in Figure 22, the torque convergence curve mimics the force convergence curve's behavior quite closely with the exception of the sign of the curves being opposite. The steady state torque value at 1325RPM as predicted by the simulation is -0.3533Nm. The relationship seen in Equation 3 between force and speed applies to torque and speed as well. The torque exerted on the blade at 1800RPM obtained from scaling the results at 1325RPM is -0.6758Nm.

Figure 23 shows a close up view of the flow field as generated by a three rotor-diameter wide fluid domain. Similar expectations and outcomes are derived from this figure as the pipe flow simulation results seen in Figure 14.

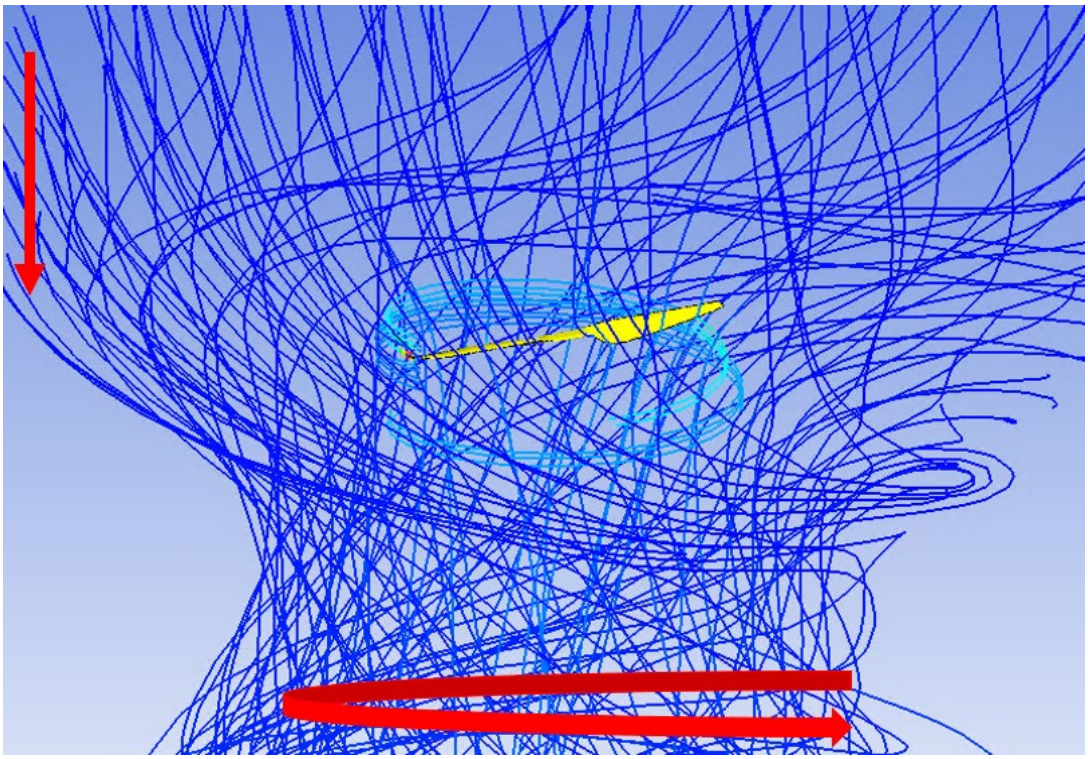

Figure 23. Flow Field, Open Flow

The fluid is again seen to enter the fluid domain with streamlines parallel to the cylindrical boundary of the domain body. In the domain area immediately around the blade's swept area, the flow constricts as it accelerates as expected and is similar to the pipe flow field. The difference between Figure 23 and Figure 14 is due to the same reason

that the analysis is more unstable and takes longer to converge than the pipe flow simulation. The domain is now wide enough to allow fluid that is influenced by the blade to pass around the blade without coming into contact with it. Fluid being entrained by the blade does not always pass over the blade, but in some instances can be pushed outward, causing it to pass by the blade. Computational time must be allotted for the outer region of the fluid domain to converge.

The suitability of the mesh for this simulation can be observed and quantified in Figure 24 and Figure 25 which show the y-plus values of the mesh over the blade surface.

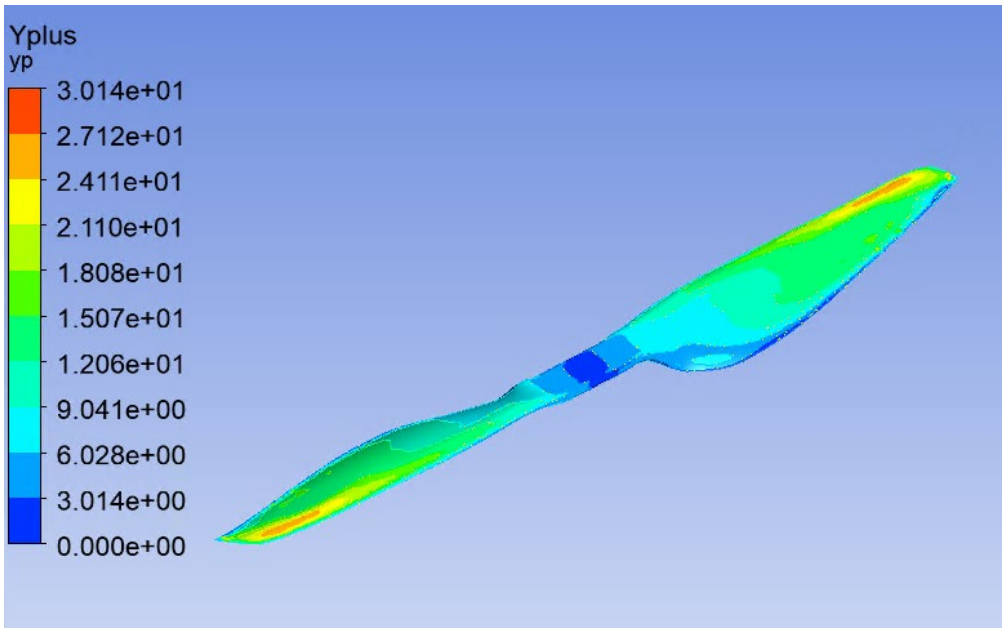

Figure 24. Y-Plus Contour Top, Open Flow

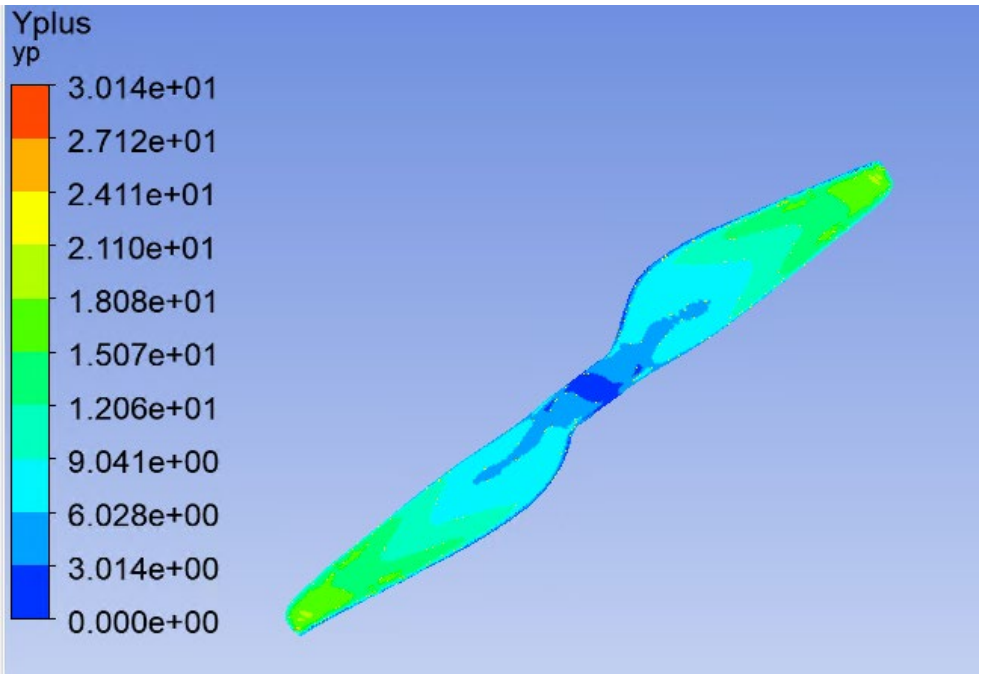

Figure 25. Y-Plus Contour Bottom, Open Flow

As is seen the highest y-plus values are located on the leading edge and outer surfaces of the blade while the lowest values occupy the trailing edge region and inner surfaces. The approximate maximum y-plus value is 27 and the approximate average value is 10 signifying that the meshing is satisfactory for this simulation. The y-plus values for the open flow simulation are similar to that seen in the pipe flow simulation as the general fluid behavior around the blade remains relatively constant.

Figure 26 and Figure 27 show the distribution of the velocity and pressure in the chordwise direction at radial distances of 200 and 340 millimeters. Similar analytical results are reached for these figures as are reached for Figure 19 and Figure 20 in the pipe flow results discussion (minimal tip loading and high fluid velocity at the tip is due to higher linear velocity).

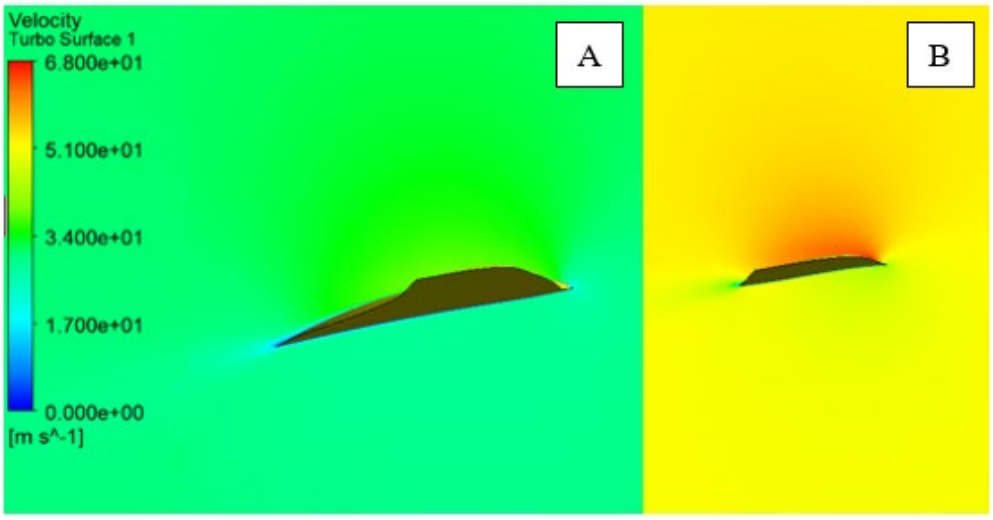

Figure 26. Velocity Distribution at Radii of 200mm (A) and 340 mm (B), Open Flow

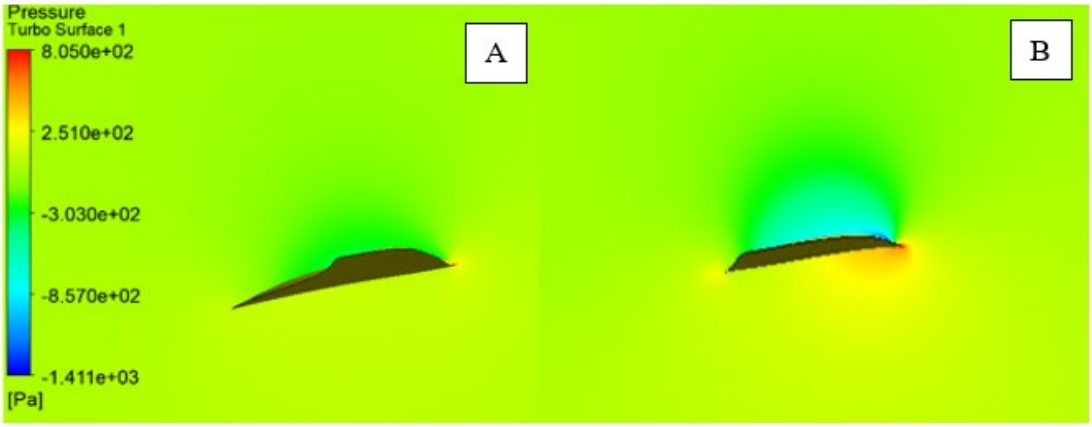

Figure 27. Pressure Distribution at Radii of 200mm (A) and 340 mm (B), Open Flow

Appendix G provides images and discussion of previous fluid domain and simulation trials that failed and the subsequent steps taken to overcome these failures.

III. SINGLE ROTOR EXPERIMENTAL DATA

A. TEST STAND SETUP

The equipment and setup process for all mechanical components of the test stand are laid out in Appendix B, while the electronics used throughout all experimental testing are depicted in Appendix C. Test stand sensors attached directly to the blade are fed into amplifiers that in turn feed information into an NI DAQ block which has individual modules that are setup to read in specific information coming in from the test stand. The NI DAQ produces an RPM value and feeds that information to the display monitors and the oscilloscope shows the throttle signal being fed into the ESC. All load and torque measurements are obtained from a voltmeter. The oscilloscope is powered directly by local electrical outlets, and the other systems (DAQ, sensors and amplifiers) are powered by a power supply box which are fed the rated excitation voltage of each specific component being powered.

B. HOVER SOFTWARE SETUP

Software that aids in the acquisition of power consumption data is Terminal, which is a "simple serial port (COM) terminal emulation program" that allows the drone to communicate with different electronic devices such as phones and computers [16]. This software communicates with Mission Planner to display position and orientation information for the drone during in flight experiments as well as maintains a data logs with energy consumption rates.

C. HOVERING DATA ACQUISITION METHOD

To begin data collection in the Terminal Software, the record button on Mission Planner is clicked prior to drone flight. Over the course of the flight, data is recorded into a .txt file. Upon completion of the flight, the recording is stopped and the metrics of the drone flight being recorded cease. The power log produced by Mission Planner during this experiment is shown in Appendix H and helps in calculating the ratio of weight to power.

D. TEST STAND COLLECTION METHOD

National Instruments is used to quantify the output of the rotor's performance via controlling the duty cycle of the ESC. Altering the ESCs duty cycle alters the rotor speed. A unique voltage is produced at each rotor speed (and ESC duty cycle), with a higher magnitude of the voltage corresponding to a higher output variable—force and torque in this case. Two DAQ units are used to measure the force and torque respectively. Prior to any test stand experiments, the sensors were loaded and unloaded with a purely axial forces, and then a purely rotational moment. The corresponding voltage outputs at each load condition for force and torque were placed into a table to produce Appendix D, sensor calibration curves. These curves are critical to interpreting any data collected moving forward in the analysis.

The primary data points that would confirm or invalidate the rotor model are the lifting force and torque generated by the blade in a hovering state. To ensure accuracy of these experimentally obtained values, multiple different methods are undertaken to provide data points for the simulation. The first method for obtaining the lifting force on a single blade of the drone is to simply weigh the drone and divide the nominal weight by the number of blades on the drone, for this experiment, six. The nominal weight of the drone is 124.55N (28.00lbf), resulting in a lifting force per blade of 20.75N. The second test, discussed in Chapter II.A, yields a blade speed of 1800RPM. The final experiment which coalesces the previously acquired data into a single validity test, is to take a single rotor and conduct a test stand trial run. Figure 28 depicts the T-Motor blade attached to all appropriate sensors for the experiment.

Figure 28. Experimental Force and Torque Acquisition

The sensor located to the left of the blade is a laser sensor which emits and receives a beam reflected off a piece of metallic tape placed on the motor hub. The received beam is converted to an electric signal and transmitted to the computer system of the test stand, which displays the signal as the blade's rotational velocity. By monitoring the displayed rotational velocity, the speed of the blade was increased until it reached the appropriate value. At this value, the voltage being output by the Futek sensor is recorded.

E. DATA ANALYSIS

Multiple voltages and RPM values are recorded in order to generate a scaling curve. This curve will display the relationship between the rotational velocity of the rotor and the corresponding force generated. The general process for obtaining force and torque from the voltage data is as follows: with a voltage from the force output of 0.9985V and backing out of the best fit-curve in Appendix D at 1800RPM a force of 21.12N is obtained. A

voltage of 1.195V from the torque cell results in a torque of 0.8176Nm. An average of the two force values and the single torque value are used as the data point to be compared to the simulations. The average between the thrust stand and average force per blade lifting force is 20.94N. The lifting force closely adheres to the previously obtained lifting force obtained from weighing the drone confirming its accuracy as two different collection methods yield near identical results. Table 3 lays out the RPMs, voltages, and subsequent force and torque values collected from the test stand for the scaling plot.

Table 3. Test Stand Metrics

RPM	Force Voltage	Force (N)	Torque Voltage	Torque (Nm)
425	-0.0261	1.332	-0.084	0.2447
725	-0.1145	3.269	-0.228	0.3189
1025	-0.258	6.413	-0.409	0.4123
1325	-0.459	10.818	-0.657	0.5402
1625	-0.715	16.427	-0.982	0.7078
1800	-0.9985	21.12	-1.195	0.8176

In conjunction with the metrics displayed in Table 3, Appendix H identifies a steady state power consumption of approximately 1.1kW, and with a known drone-mass of 125.64N, the experimental mass to power consumption ratio in units of N/kW is 114.22.

IV. NUMERICAL AND EXPERIMENTAL RESULTS COMPARISON AND VALIDATION

The test stand metrics shown in Table 3 are now plotted against force and thrust values obtained from the pipe flow simulation at the various rotational speeds and the open flow simulation results at test stand collected values as well as scaled values. Figure 29 and Figure 30 show the accuracy of the scaling laws laid out in Equation 2, Equation 3, and Equation 4.

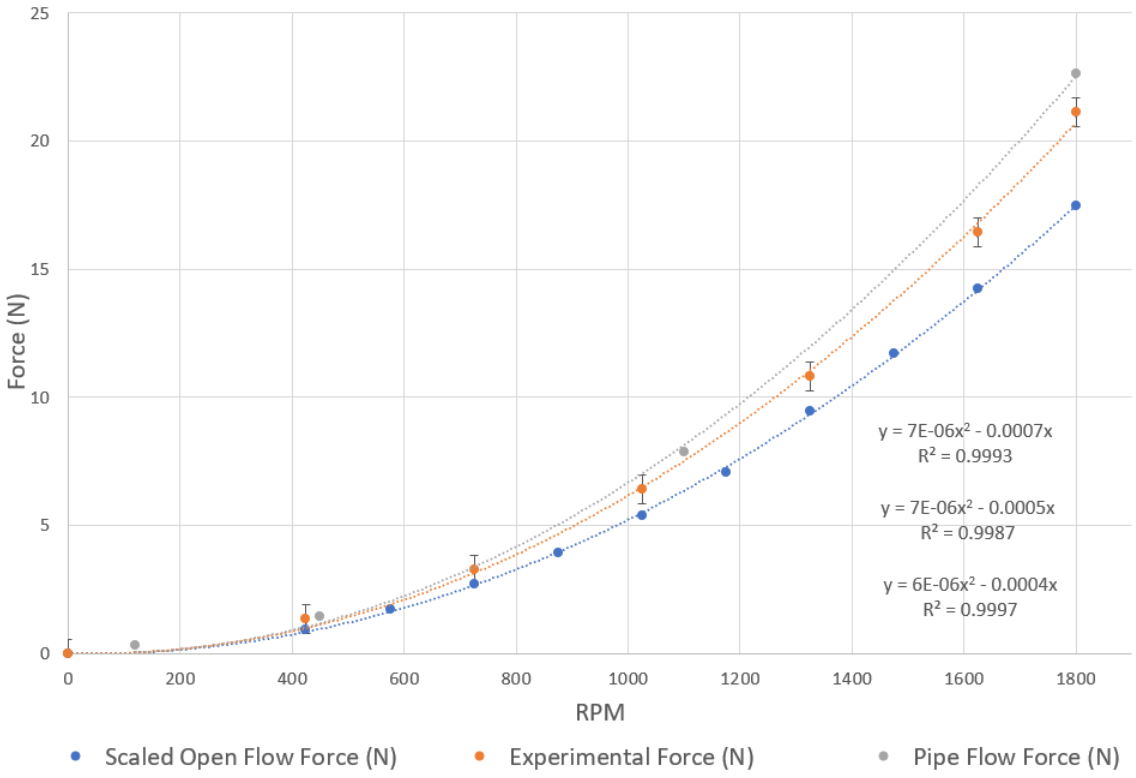

Figure 29. Force and Speed Relationship

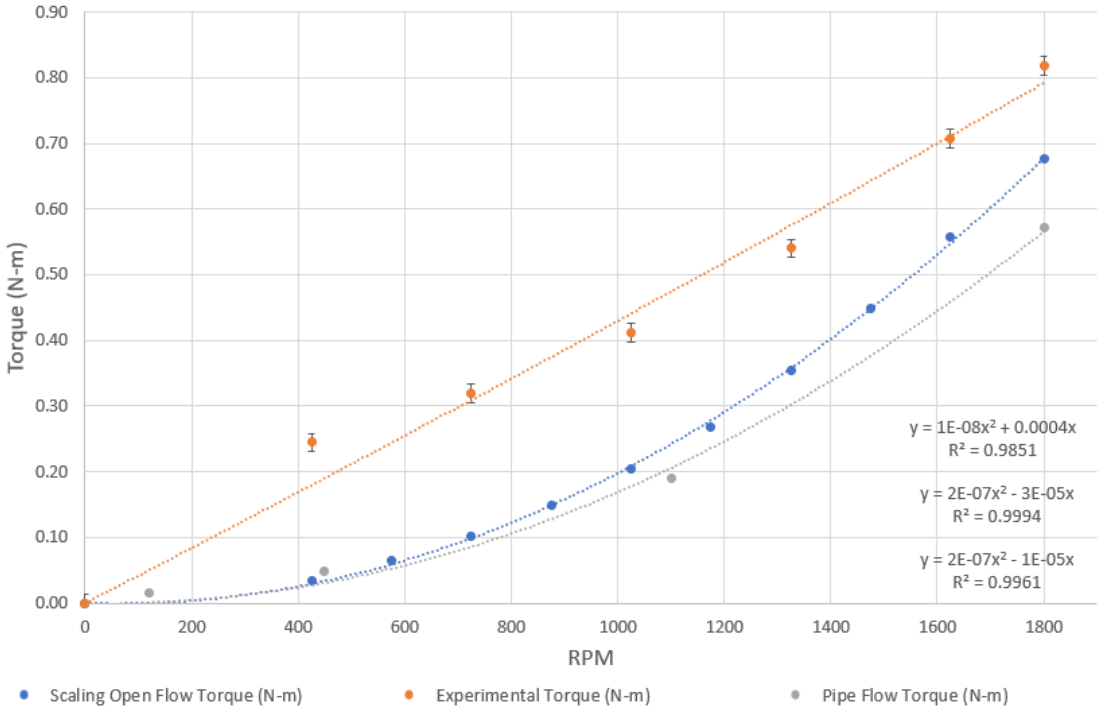

Figure 30. Torque and Speed Relationship

In both figures the trend of each curve appears to adhere to the assertion in Equation 3 that the relationship between both torque and force is a quadratic one. The open flow force and torque most closely adhere to the quadratic relationship because the simulation data ceases at 1325RPM and is scaled to 1800RPM using the quadratic scaling law. The experimental and pipe flow values follow the same trend as the scaled values. The difficulty of measuring drag force, and subsequently torque, on an airfoil is seen again as the data in Figure 30 are much more dispersed in comparison to those in Figure 29. The error bars displayed on the experimental data curves of Figure 29 and Figure 30 define the region within which the error in measuring is accounted for by the sensor's specification sheet. This value is 0.25% of the rated output, which is 0.555N of force and 0.0143Nm of torque [17]. The region that is the most difficult to measure and simulate is seen to be the area of low linear velocity. There are multiple reasons for this. The first being that the small torque values exerted on the blade result in a low signal to noise ratio, making it difficult for the sensor to filter out noise in the recorded signal. This produces large relative error. The second reason is due to the simulation setup. For the numerical simulations, an SST model

is used with no transition model. This model type more accurately simulates turbulent flow and is thus more accurate around the outer radii of the rotor where the fluid flow is more turbulent. In the inner radii of the blade, the linear velocity is low in comparison, and thus, a purely turbulent assumption does not hold up in this region. No transition models are used in this analysis due to the additional computational time associated with their implementation. The final reason is due to rotor disk loading. On multi-rotor aircraft, the rotors spin counter clockwise to the neighboring rotor and the clearance between the two is low. In this case, the boundary condition is similar to a symmetry plane as the streamlines are constrained to move axially downward only. This creates an uneven disk loading on the rotor and contributes to the error between experimental and modeled results. The raw data used to generate the curves seen in Figure 29 and Figure 30 are found in Appendix I.

Table 4 displays the values of all results obtained both by the numerical model (both pipe flow and open flow) and the experimental methods previously discussed.

Table 4. Force, Torque, and Hover Results at 1800RPM

-	**Pipe Flow Simulation**	**Open Flow Simulation***
Force	**N**	**N**
Weighing Drone	20.75	20.75
Test Stand	21.12	21.12
Simulation	22.59	17.44
Error	7.9%	16.7%
-	-	-
Torque	**Nm**	**Nm**
Test Stand	0.8176	0.8176
Simulation	0.5903	0.6758
Error	27.8%	17.3%
-	-	-
Hover Efficiency	**N/kW**	**N/kW**
Hover	114.22	114.22
Simulation	203.03	136.91
Error	77.75%	19.87%

* Denotes the values obtained for 1800RPM are done so using the scaling law

When specifically inspecting the torque, it is seen that a large discrepancy is present between the observed and true value. This is due to the design process of rotors and airfoils, where the primary objective is to produce lift and reduce drag. This design parameter

makes simulating accurate torque extremely difficult as it is affected by the drag force over the blade. The scaling law plots display the difficulty in modeling as the force from the simulation, open and pipe flow simulations all closely match while the torques from the same three analyses differ greatly in comparison. From the torque, power input can be calculated using Equation 5.

$$P = \tau\omega \tag{5}$$

where P is the power, τ is the torque, and ω the rotational velocity in radians per second. Doing this and scaling the product by six to account for the total power consumed by all of the drone rotors produces an expected (simulated) energy consumption rate of 667.6W for pipe flow and 764.3W for open flow. This simulated power input for a six-bladed drone is approximately 61% and 70% respectively of the total output power as measured by Mission Planner. The energy consumption rate as measured by the Terminal software is a metric that accounts for all power consumed by the drone, not just the rotors. Additional equipment on the drone such as sensors draw power from the fuel cell which increase the total power consumption as recorded by Mission Planner.

V. ACTUATOR DISK THEORY VALIDATION

A. DATA EXTRACTION SETUP (VELOCITY AND PRESSURE)

In order to extract useful data pertaining to the velocity and pressure distributions, multiple steps need to be taken when processing the raw data. First, two contour planes are constructed immediately above and below the blade to have 100 contour levels. The variable the contour planes display should be either the pressure or velocity depending on which is being analyzed. The data points for pressure and velocity are taken in increments of 10 contours to produce approximate distribution curves rather than at each of the 100 contours. In order to extract values over a slice of the contour, two polysurfaces are inserted on planes immediately above and below the blade surface. These provide metrics on the fluid properties immediately incoming to and exiting the blade and can be manipulated to approximate the desired metrics (pressure and velocity) at the blade. Figure 31 shows the two polysurfaces over a center radial value.

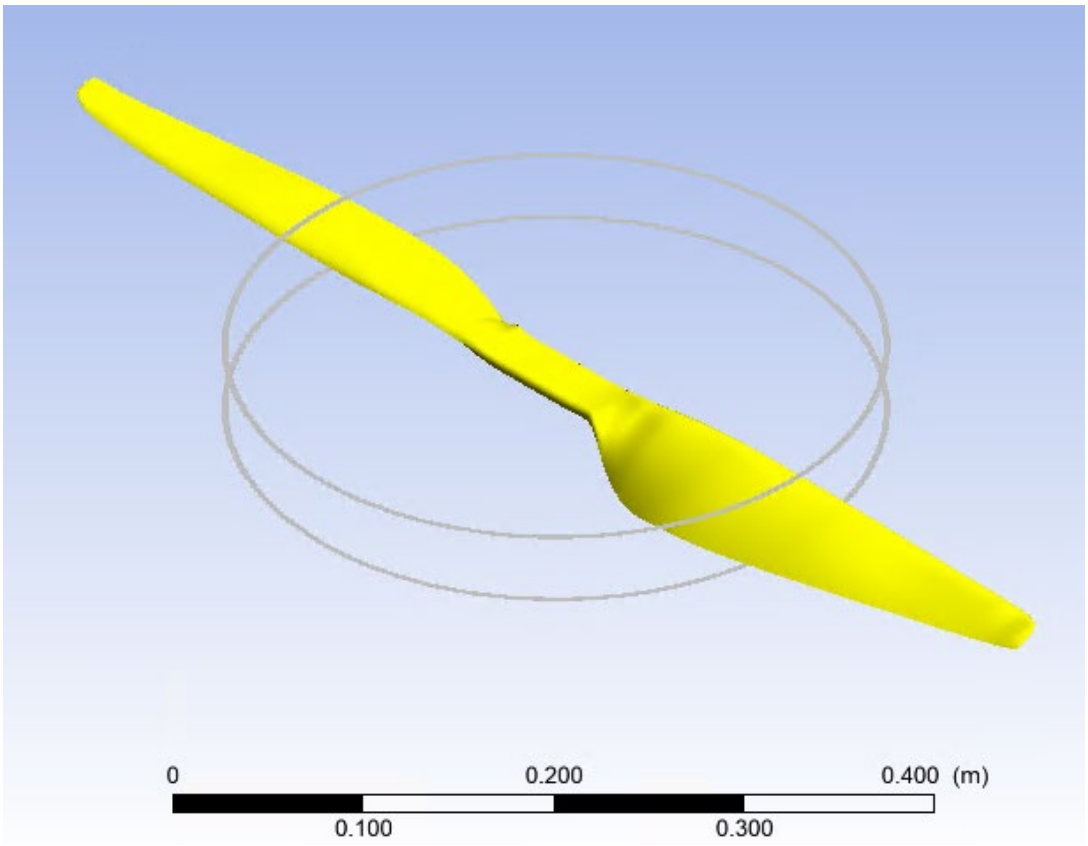

Figure 31. Polysurfaces Above and Below Blade

Viewing streamlines that originate immediately above the blade as seen in Figure 32 give an idea of the velocity distribution curve for the pipe flow. In Figure 32, two major recirculation zones are seen.

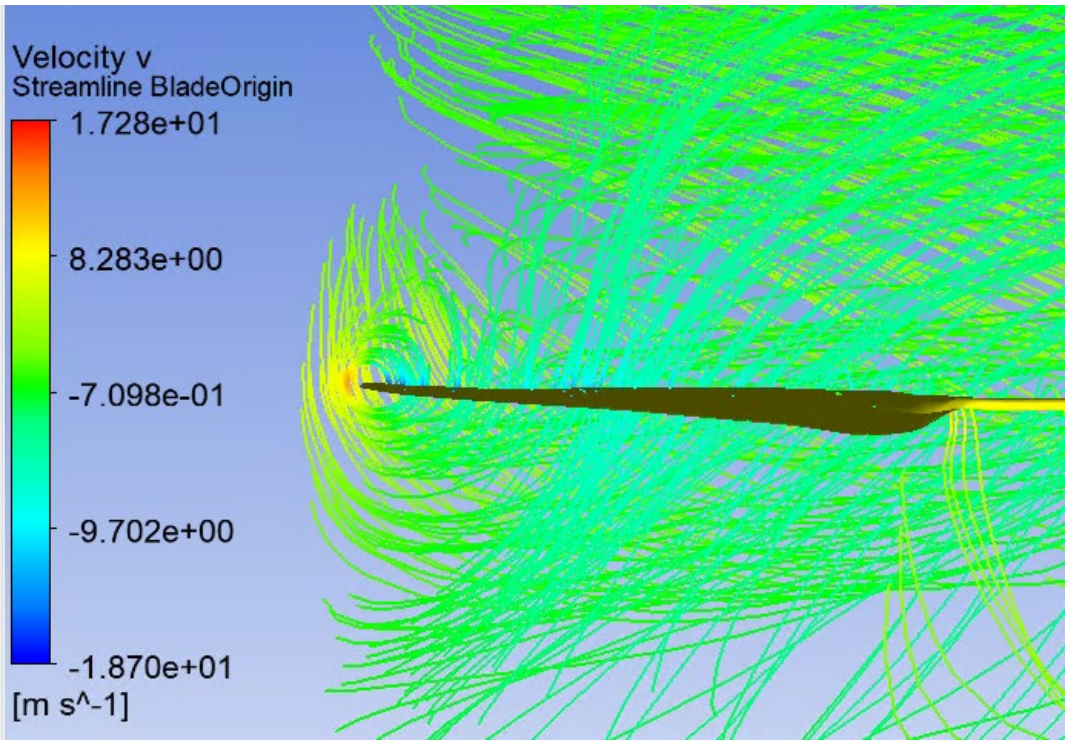

Figure 32. Blade Streamlines, Pipe Flow

The first and inner most one is located across the hub of the blade. On the hub it is seen that the streamlines do not follow the background streamlines, but instead move upward. A similar phenomenon is seen at the tip of the blade. The distinguishing difference between the two recirculation zones is the magnitude of each event, which is seen to have higher values at the blade tip. The pressure and velocity gradients along the blade radius are not expected to be mimic simple functions, but rather be most accurately estimated by a higher order polynomial due to small regions of recirculation present along the blade radius.

The velocity streamlines of the open flow simulation shown in Figure 33 is seen to be quite different in comparison to those in Figure 32.

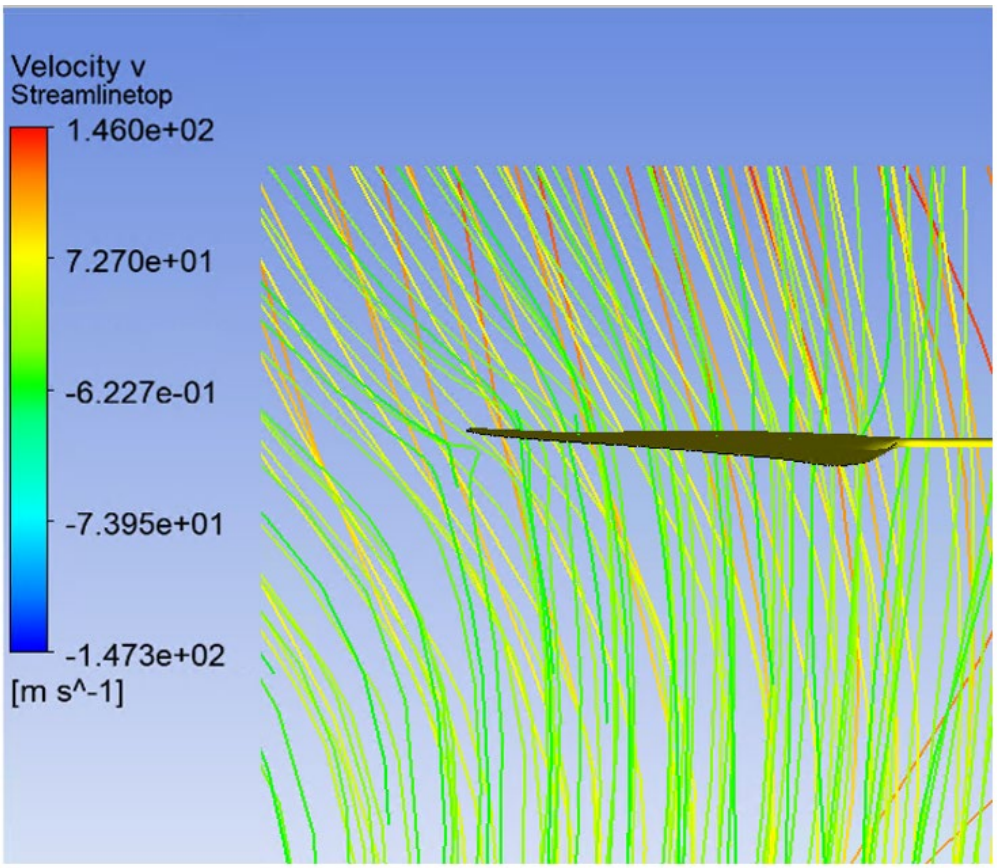

Figure 33. Blade Streamlines, Open Flow

The streamlines shown in Figure 33 flow smoothing across the face of the blade. There does not appear to be any type of recirculation occurring at either the blade hub or tip. The absence of recirculation zones in the open flow simulation is attributed to the increased volume and area about which the flow can move. Increasing the domain volume allows for regional recirculation zones seen in pipe flow to resolve themselves.

B. VELOCITY AND PRESSURE DISTRIBUTION CURVES

Figures 34 and 35 show the velocity distribution in the radial direction of the blade for both pipe flow and open flow. The plot is sampled in increments of 10% of the total radius length with additional samples being taken at regions of high variability along the length of the radius to accurately capture the unique behavior in those regions. Due to the more stable nature of the open flow simulation, a single plot of that velocity curve is

displayed in Figure 38 to prevent details of that curve from being suppressed by the highly variable pipe flow curve.

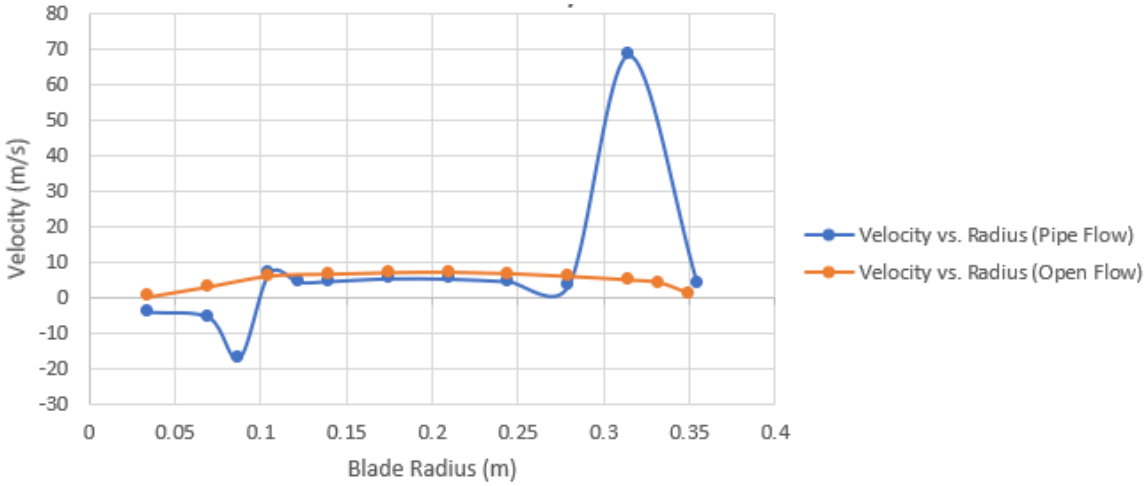

Figure 34. Velocity Distribution Curve Along Radius

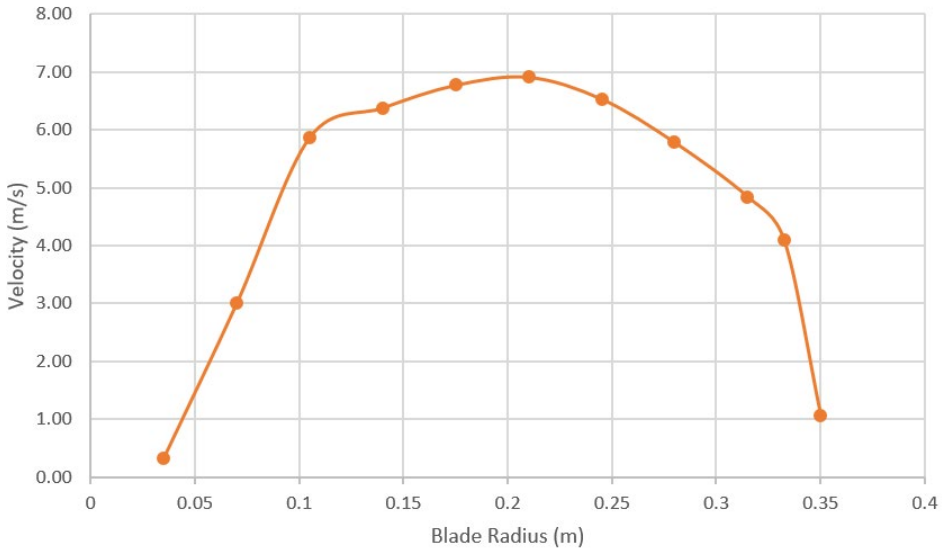

Figure 35. Velocity Distribution Curve Along Radius, Open Flow

For both pipe flow and open flow, the net fluid flow is expected to be negative as flow is moving in the negative y-direction through the control volume. For simplicity in presentation, the values on the graph shown in Figures 34 and 35 are made to have positive

flow be in the downward direction. Unique to pipe flow, the fluid velocity is negative in the hub region of the blade as it is being recirculated. As the radius of the blade increases, the velocity begins to maintain a positive value as the fluid is forced downward by the blade. The magnitude of the recirculating velocity field at the blade tip is far greater than at the hub due to the higher linear velocity as well as the smaller geometries of the blade tip in comparison to its hub. This causes the fluid velocity to spike to nearly 70 m/s. Previously noted for open flow is the absence of recirculation zones, as expected, the velocity distribution curve from the open flow simulation is much smoother in comparison to the pipe flow. The velocity starts and ends at approximately 0 m/s at the blade hub and blade tip while smoothly increasing in magnitude to a maximum at the approximate radial center of the blade.

The next image, Figure 36, shows the pressure contour along the disk generated by the planform area of the blade's rotation for the pipe flow simulation (a similar disk area pressure distribution is expected for the open flow case).

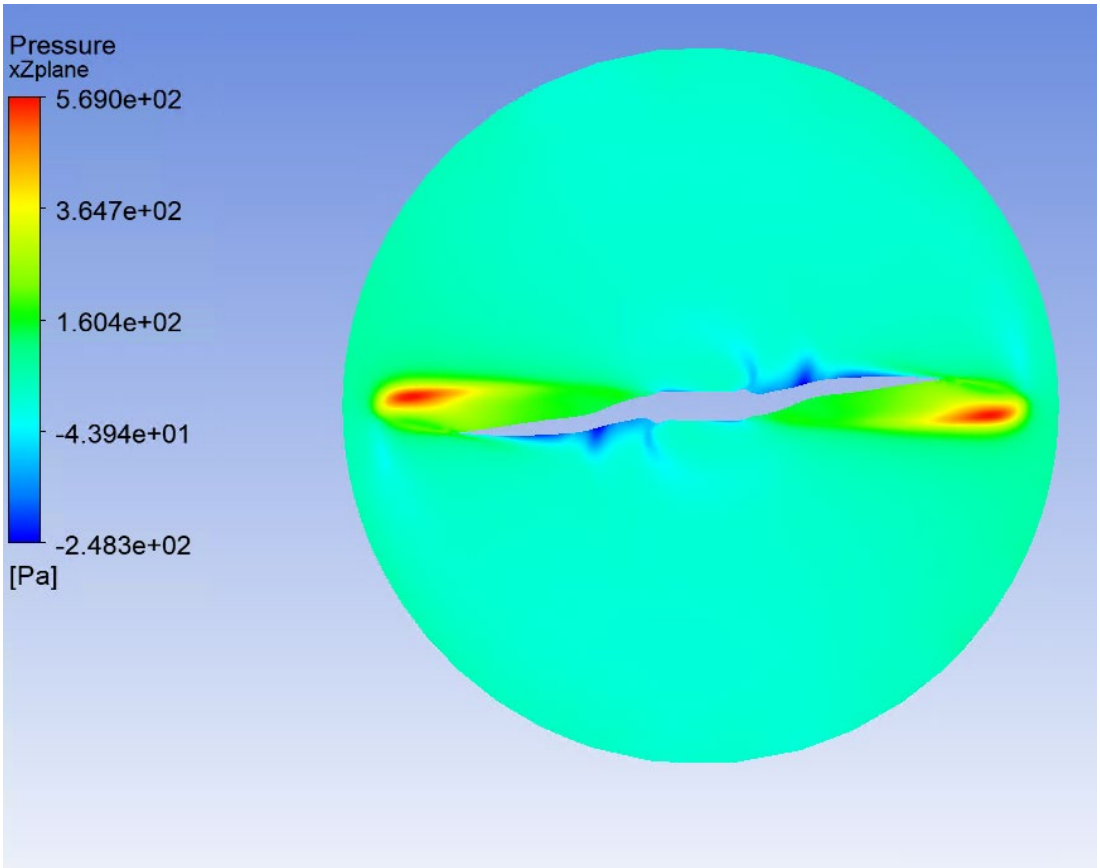

Figure 36. Pressure Distribution Across Rotor Planform Area, Pipe Flow

Immediately an error in assumptions made by actuator disk theory is seen. Actuator disk theory assumes that the pressure distribution is constant across the entire swept area of the blade. In Figure 36, a true pressure distribution is seen to have comparatively higher-pressure gradients near the blade's body, with the highest values occupying the region near the blade tips. Even the hub of the rotor produces non-uniform pressure gradients. This figure, after manipulating multiple properties, provides the radial pressure distribution curve along the blade seen in Figure 37, which displays results for the pipe flow and open flow simulations. This radial pressure distribution curve can be implemented to improve the actuator disk theory assumption of uniform disk pressure.

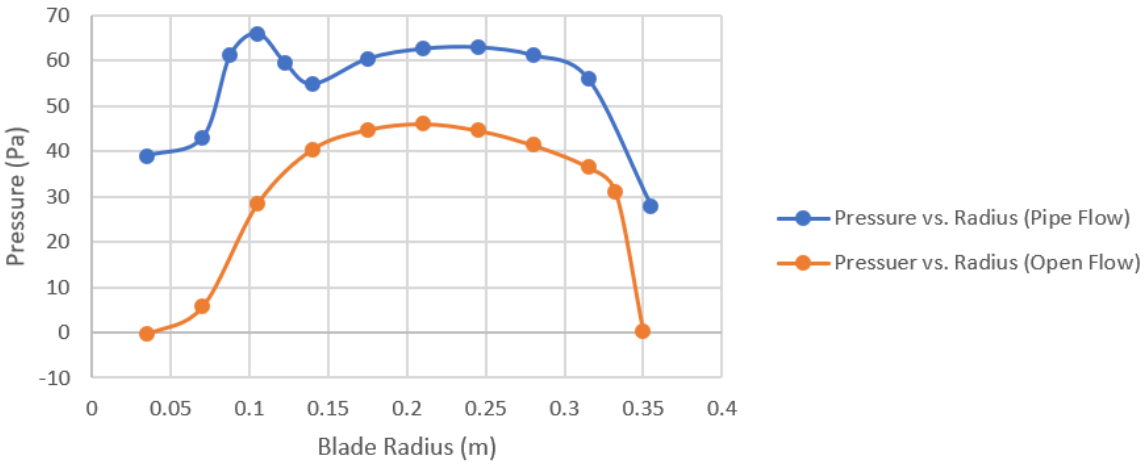

Figure 37. Pressure Distribution Curve Along Radius

Figure 37 shows the net pressure acting on the bottom surface of the blade, and is thus a lifting pressure. When inspecting the pipe flow results of Figure 37, a similar trend is seen as previously seen in Figure 36, two unique regions along the radial distribution. In Figure 37 it is seen that the pressure on the blade is at its second lowest value when at the blade hub. As the radial distance increases, the pressure initially increases due to the first recirculation zone as shown by Figure 37. As the flow exits the recirculation zone, the pressure levels off and is relatively constant from 0.15 meters up to right before the blade tip at 0.30 meters. Dissimilar to what is seen in Figure 37 for pipe flow, but predicted by the fluid flow field seen in Figure 14 is a drop off in the pressure distribution as the blade tip is approached. It is seen that minimal lifting is done by the outer portion of the blade. The behavior of the pressure distribution curve between the radii of 0.300 and 0.355 meters, confirms that the blade tip is unloaded and has little influence over the lifting characteristics of the entire blade. For the open flow pressure distribution, similar curve geometry is seen when compared to the open flow velocity distribution. A much smoother distribution curve from hub to blade tip is seen with no major inflections along the curve. The net lifting behavior as derived from the pressure distribution curve of the open flow simulation is slightly lower than that of the pipe flow and thus the magnitude of the open flow pressure distribution curve is lower along the radius. The majority of lifting is done in the median radii values of the blade, and as confirmed in the pipe flow simulation, minimal lifting is

done at the tip of the blade. Appendix J contains all raw data used to generate the velocity and pressure distribution curves.

C. DATA EXTRACTION SETUP (SPANWISE COEFFICIENT OF LIFT)

In order to obtain the spanwise coefficient of lift, a contour plane that is parallel to the blade's chord is first inserted. Next, a polyline is inserted at the intersection of the plane and the blade surface as shown in Figure 38.

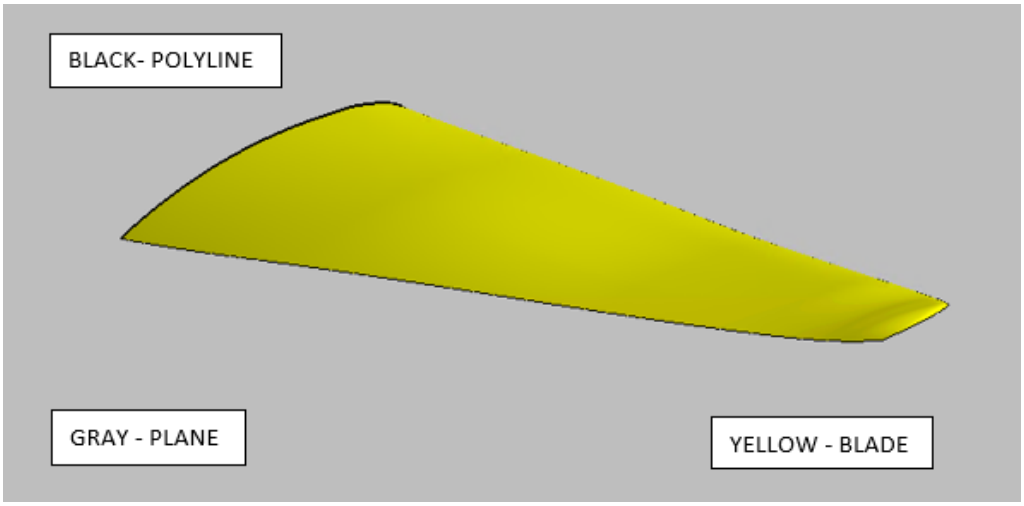

Figure 38. Polyline Insertion

This polyline will move to align where the plane and blade intersect. When the location of the plane is moved, the polyline does as well, allowing for data along the rotor's chord to be collected at any radius. Following the implementation of a polyline, Equations 6, 7, and 8 must be implemented as expressions in the modelling software in order to extract the properties needed to calculate the spanwise coefficient of lift. A full list of expressions can be found in Appendix F, Table 6.

$$C_L = \frac{2F_L}{\rho v^2 A} \tag{6}$$

$$C_L = \frac{4\sum(pdA\sin(\theta))}{\rho v^2 \sum(dA\sin(\theta))} \tag{7}$$

$$\sin(\theta) = \frac{\perp Y}{\sqrt{(\perp Y)^2 + (\perp Z)^2}} \tag{8}$$

These three equations are crucial to the successful calculation of the spanwise coefficient of lift. Equation 6 shows the standard equation for calculating the coefficient of lift. Equation 7 shows an adaptation of Equation 6 that calculates the coefficient of lift along a polyline at a pre-determined radius. Instead of integrating, a summation function is used to calculate the polyline-varying values (pressure, area, and the normal vector of pressure and area in relation to the surface of the blade). Equation 8 shows a simple substitution for the trigonometric function in Equation 7. Using the unit-value in the normal direction of the Y and Z-axes ensures that the value of sin(θ) will never go to infinity at any point along the polyline.

D. SPANWISE LIFT COEFFICIENT CURVES

Analysis of the spanwise coefficient of lift is a common method by which commercial rotor performance is evaluated and thus applicable to this study. The coefficient of lift along the blade more accurately conveys the disk loading of the rotor. Following the implementation of the expressions laid out in Equations 7, 8, and those found in Table 6, the plot of coefficient of lift in the spanwise direction of the rotor for both the pipe flow and open flow simulations are created. Figures 39 and 40 show these plots.

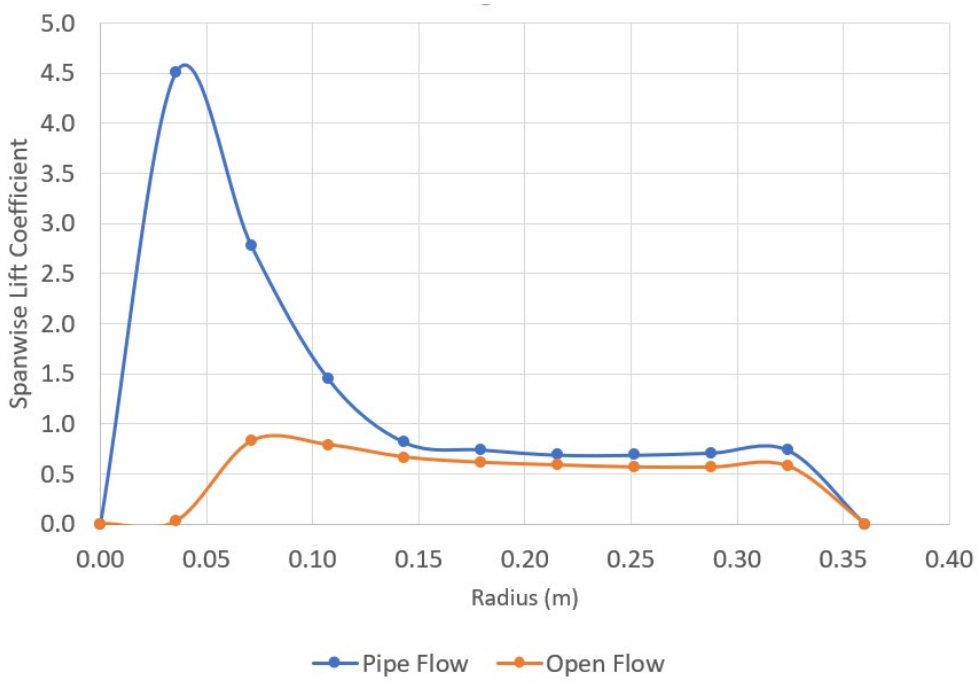

Figure 39. Spanwise Coefficient of Lift

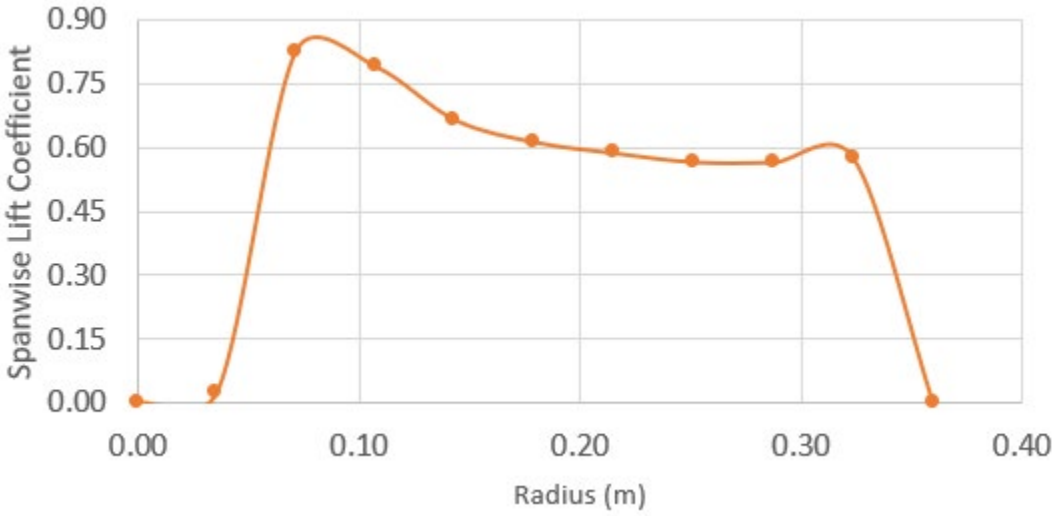

Figure 40. Spanwise Coefficient of Lift, Open Flow

As is seen in Figure 39, the value of the coefficient of lift in the central radii range of the rotor is nearly identical between the pipe flow and open flow simulations, maintaining a value of approximately 0.67. The coefficient of lift at the blade tip for both the open flow and pipe flow simulations is seen to go to zero, which again confirms the

theory that minimal lifting is done at the blade tip. The lifting coefficient is seen to spike near the rotor hub in the pipe flow simulation. This is due to the large recirculation zone occurring in this region as previously displayed in Figures 34 and 37. It is recommended that the C_L data from the open flow simulation be used for future work, hence a more depictive Figure 40, as its values are more stable when measured from blade hub to tip. Appendix K contains the raw data used to generate Figures 39 and 40.

VI. CONCLUSIONS

Conducting a 3-D CFX simulation of fluid flow is a viable method for determining blade performance. The resulting simulation over the course of months of problem shooting and model development resulted in a 7.9% error in force and 27.8% error in torque when simulating pipe flow, a 16.7% and 17.3% error for force and torque respectively when scaling an open flow simulation, while also producing accurate and in-depth visual results of fluid behavior over a rotor. When investigating outside experiments, a similar level of error was reported (15%) [10]. Despite producing results that match experimental data and the expected global and local flow field, it is not recommended that fluid modelling be done in this (3-D CFX) capacity. Now with a documented process, known accurate results, and the generation of radial pressure and velocity gradient curves, a much shorter analysis can be done making more accurate assumptions about disk loading distributions. Future ways to improve the three-dimensional modeling include expanding the model size to simulate a higher degree of open flow rather than the three blade-diameter fluid-domain used in this analysis, and redesign the blade to have a smooth leading edge rather than a sharp one. Additionally, increasing the resolution of the mesh, will to some degree, increase the solution accuracy within the entire fluid domain. Despite having reached a steady state torque and thrust value, allowing the simulation to continue iterating until residuals have completely converged will increase the fidelity of the model.

THIS PAGE INTENTIONALLY LEFT BLANK

VII. RECOMMENDATIONS

If a three-dimensional CFD analysis is conducted, ways to increase the accuracy of the model include redesigning the blade to have a smooth and continuous leading edge, refining the fluid domain's mesh, transfer simulation to a computer with higher computing capabilities, expanding the fluid domain to more realistically model open flow, and conducting a transient analysis rather than a steady state analysis. By implementing body sizing on the fluid domain, something not done in this analysis, and refining the face sizing, inflation layers and spheres of influence element size, the y-plus value on the blade surface can be decreased which implies a better suited mesh for the simulation. Transferring the simulation to a super computer or higher power system will reduce the analytical time from weeks to days or even shorter depending on the size of the simulation. For stability reasons, a fluid domain three blade diameters wide is used. Accuracy can be improved by widening the fluid domain's diameter to further minimize the difference between the experimental and simulated results. By conducting a transient analysis, a linear function can be implemented to ramp up the blade velocity throughout the simulation rather than increasing the blade speed by discrete steps as in a steady state analysis. When conducting a steady state analysis, each incremental increase in the blade speed required anywhere from 1500 to 5000 iterations depending on the step size of blade velocity to converge onto a steady state thrust and torque value for that blade velocity. The number of iterations required to re-converge on a steady state solution will change with model variation.

THIS PAGE INTENTIONALLY LEFT BLANK

APPENDIX A. COMPONENTS THAT CONTRIBUTE TO HOVER EFFICIENCY

Both direct current (DC) motors and electronic speed controllers (ESCs) exist in a quickly growing market [18]. This high interest market is drawing increased interest and funding into the performance, optimization, and adaptability of both of these electrical components. One emerging market that has generated research into ESC and DC motor advancement is the aviation sector. Small aircraft such as recreational drones and toy aircraft are able to utilize an entirely electrical fuel cells due to their light weight and lower energy consumption rate, and with their invention and mass production, have become viable in both the private and public sectors. Optimization of their mechanical and electrical components is only a logical response to their success as it can and will drive down costs and increase performance.

A. ELECTRICAL MOTORS

For high efficiency and better performance—speed specifically— a brushless DC motor is preferred over a brushed DC motor. The main drawback for a brushless DC motor is the cost, which is higher due to the need for additional electrical equipment to operate the motor [19]. The highest efficiencies are achieved when the motor is operating within its design envelope. As seen in Figure 41, most electrical motors instantaneous efficiency peaks at approximately 75% of the motor's rated load, while the efficiency remains relatively unchanged when operating within the 50%-100% rated load range [20].

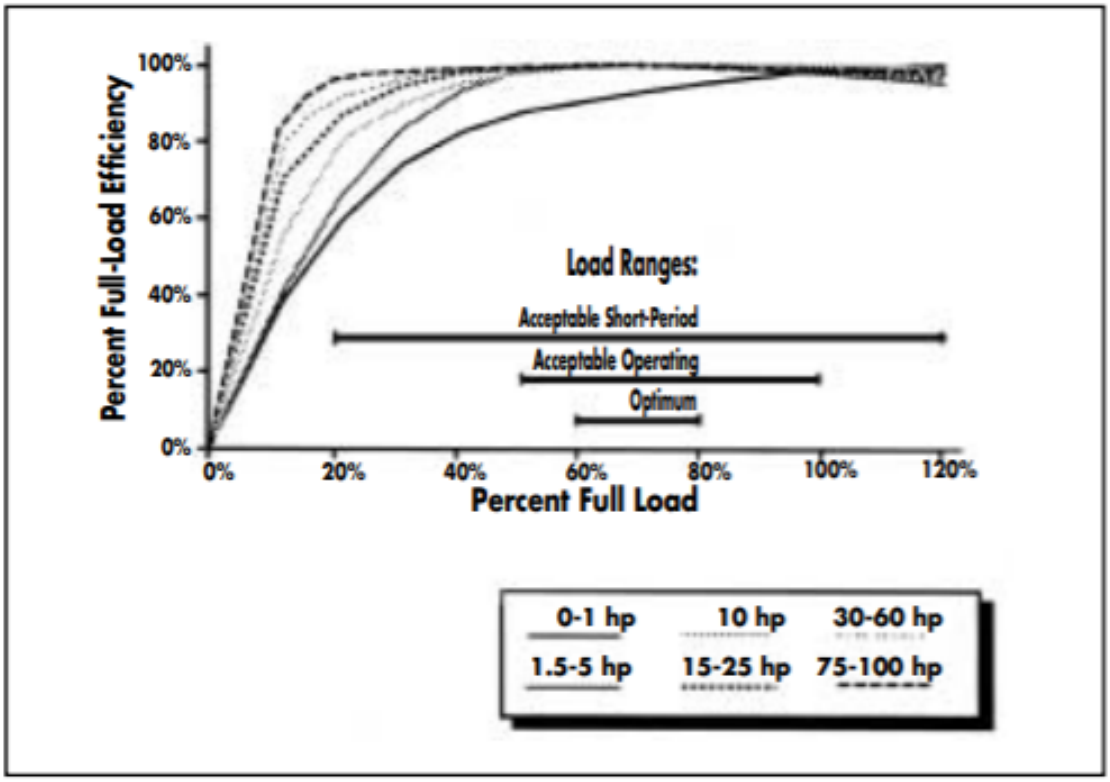

Figure 41. Motor Efficiency as a Function of Load Percentage. Source: [20].

For motors with a rated power greater than 1hp, the efficiencies all converge at approximately 50% load mark and have an efficiency value of greater than 95%. It is when the motors are operating drastically off design, in this case under 50% or greater than 100% of the rated load, that poor efficiencies and damage to equipment are encountered. Thus, in order to optimize electrical efficiency, the test load must fall between 50% and 100% of the rated load of the motor. The current market provides users with multiple DC motor options with respect to design specifications, allowing users to select a motor that operates optimally for different testing conditions.

The two most important parameters that affect motor performance are the torque and speed at which the motor operates under. In motors, the relationship between the torque and speed are inverse, while the relationship between torque and the number of poles on the motor is directly related. The rotational speed of the motor slows when the load torque

increases and vice versa. Figure 42 shows current motor option offered by T-motor, a company that specializes in electrical components and equipment for recreational drones.

Figure 42. T-Motor U-8 Lite. Source: [21].

The specification sheet of this motor lists a total of 42 individual poles on the motor [22]. Each copper winding seen in Figure 42 is a single pole. The maximum rotational speed of the motor is related inversely to the number of poles on the motor. More poles lead to lower speeds due to the need to increase the diameter of the motor in order to accommodate the increased number of poles. However, a larger diameter motor has a larger lever arm, leading to higher torques. This is the tradeoff between torque and speed. Motor power is the product of torque and speed, so in order to have high hover efficiencies in a drone, that is, lower power input per unit weight of the drone, a high torque, low speed motor is desired. In the modern market, motors are advertised and sold with a KV rating. A motor's KV rating tells the motor speed per volt applied. For example, a 95KV rated

motor would spin at 95 RPM with a single volt applied to the motor with no load applied. The higher a motor's KV rating is, the more power the motor will have [23]. In order to optimize hover efficiency, lower KV rated motors are desired because they consume less power and operate at lower speeds.

B. ESCS

An Electronic Speed Controller (ESC) is the brain of a propulsion system. ESCs dictate the speed the motor runs at through modulation of input signals known as pulse width modulation (PWM) which produces an approximate analog signal via digital means [24]. A simple schematic of PWM appears in Figure 43.

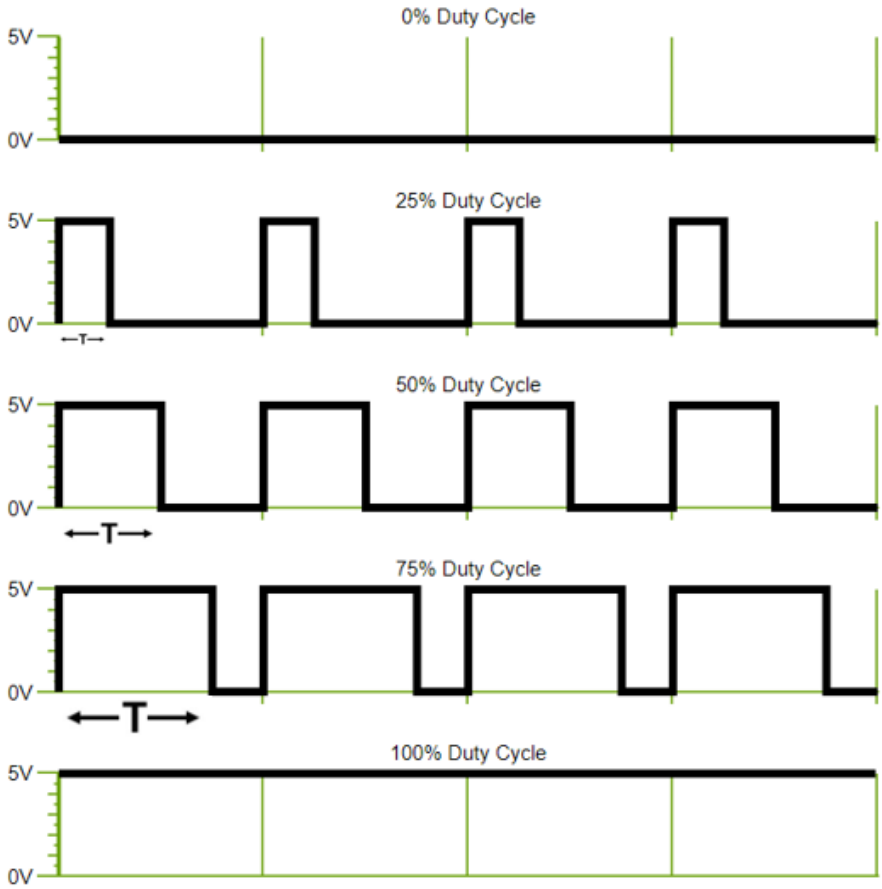

Figure 43. Pulse Width Modulation. Source: [24].

Characteristics of a PWM signal are the duty cycle and pulse width. The pulse width represents the time a single pulse remains "on." In the case of Figure 43, the time a single pulse remains at 5V and is equivalent to the inverse of the operating frequency. The duty cycle is simply the percentage the signal remains on for a single cycle [24]. The PWM frequency is directly related to vehicle performance. In the case of drones, a higher PWM frequency will produce faster response times and increased control over drone flight behavior [25]. PWM is producing a digital signal which is meant to mimic an analog signal. Because this is not a perfect conversion method, losses and inefficiencies are incurred in this process. Companies are now in pursuit of creating a pure sine wave PWM, which would be a perfect conversion from digital to analog. This type of conversion cannot currently be done, as even a "perfect" sine wave is a very fine combination of square waves. However, the closer a digitally modulated signal can be to a sine wave, the lower inefficiencies will be. Typical PWM frequencies are on the scale of kilohertz.

Despite being a crucial component to drone performance, there is very little knowledge available on ESC efficiencies [18]. When analyzing drone hover efficiency and overall performance, knowledge of the ESC will be necessary if improvement is desired. A large contributor to ESC efficiency is the PWM frequency, but this frequency must be balanced with temperature management of the component itself. "For high poles and high-speed motors, the higher PWM frequency can make the motor drive smoothly, but the higher PWM frequency will make the ESC hotter" [26]. Failure to properly manage heat generation within the ESC can result in component damage and greater losses across the entire electrical system. Although efficiency versus RPM plots will be unique for each ESC, general efficiency trends can be mapped through variation of speed and torque being handled by the ESC. One such trend is mapped in Figure 44, which is unique to a Hobbywing Platinum 50 Amp ESC in this case [18].

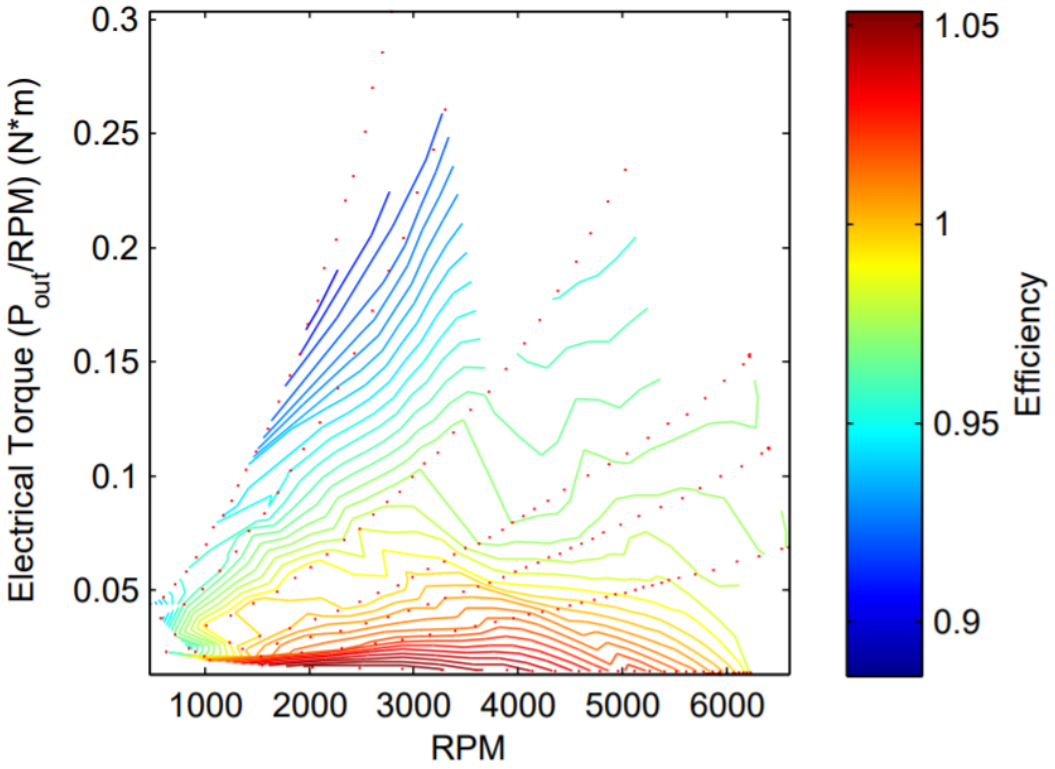

Figure 44. Load Map for the Hobbywing Platinum 50A. Source: [18].

Being experimental data, it is seen that efficiency is mapped at greater than 100% which is not possible. However, the general trend shows that ESCs operate most efficiently at high RPM, lower torque settings while efficiency quickly decreases as RPM decreases and load increases. In order to generate load map for an ESC, multiple loads and speeds will need to be analyzed. In order to optimize ESC efficiency which in turn will contribute to higher system efficiencies, a balance between torque and RPM will have to be reached.

APPENDIX B. TEST MOUNT EQUIPMENT

In order to mount equipment horizontally onto an 80/20 aluminum frame test stand, five polycarbonate mounts were created in SOLIDWORKS computer design software (Figures 45–49). Equipment that needed to be mounted include a Futek biaxial sensor that measured the torque and thrust of the propeller being tested, the T-motor DC motor onto which the drone rotor was attached and Futek amplifiers which transferred load data to be converted by a National Instruments DAQ. Both sides of the four polycarbonate mounts that connected the biaxial sensor and DC motor are shown as designed in SOLIDWORKS.

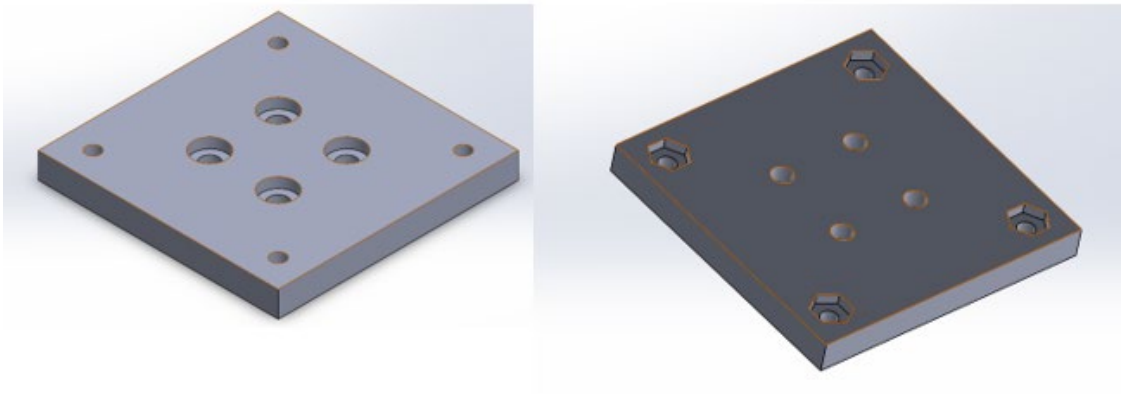

Figure 45. 80/20 Mount

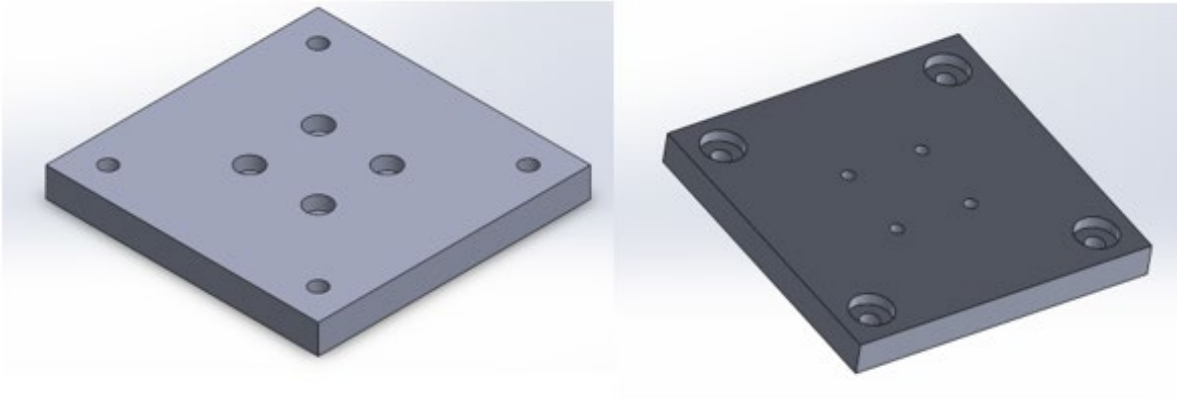

Figure 46. Sensor Mount 1

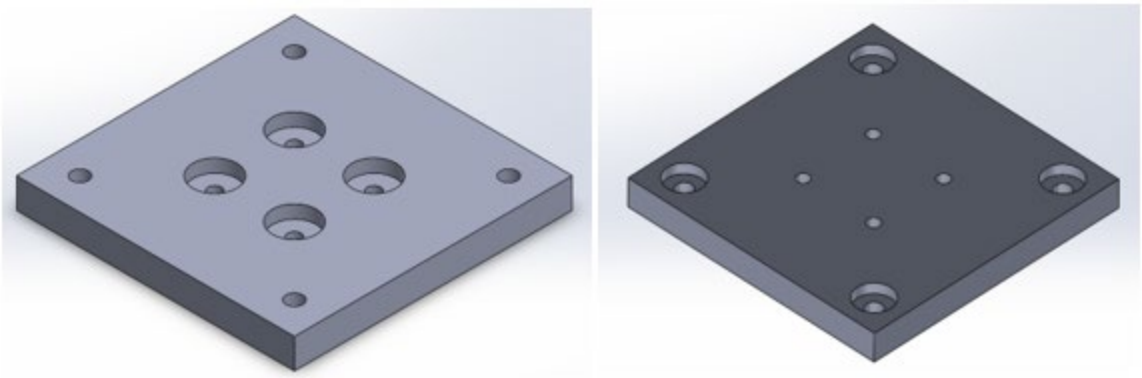

Figure 47. Sensor Mount 2

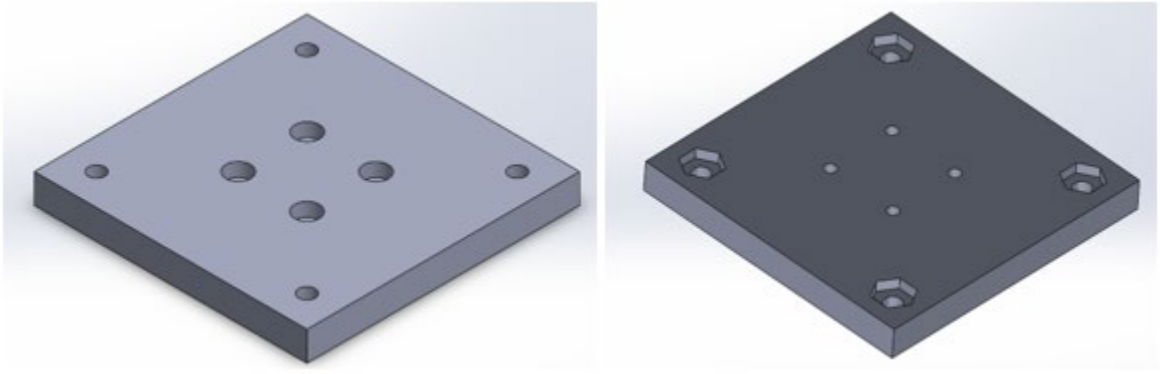

Figure 48. Motor Mount

The location of the screw holes on both the biaxial sensor and DC motor did not allow for a single connecting plate to be used between the 80/20-sensor interface and the sensor-motor interface. It was necessary to design two plates that would connect to each other and then to either the test stand, sensor or DC motor. The SOLIDWORKS model designed to mount the amplifiers to the test stand are shown in Figure 49.

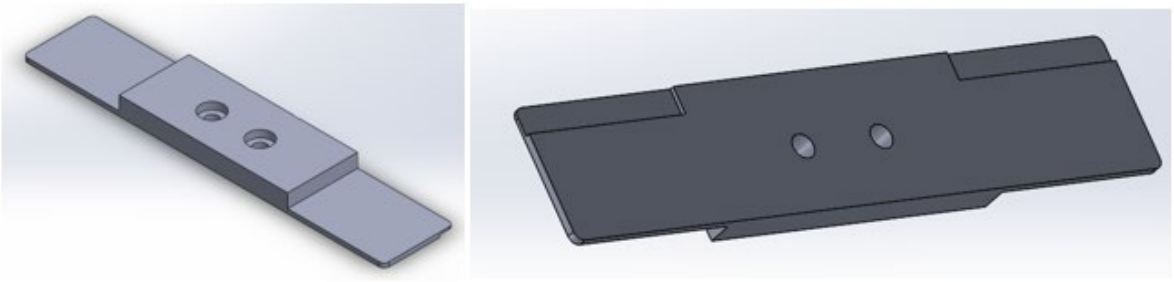

Figure 49. Amplifier Mount

The engineering drawings for each component are shown below in Figures 50–54. The drawings appear in the same order as their respective components in Figures 45–49. All dimensions for the engineering drawings are in inch, pound, seconds (IPS).

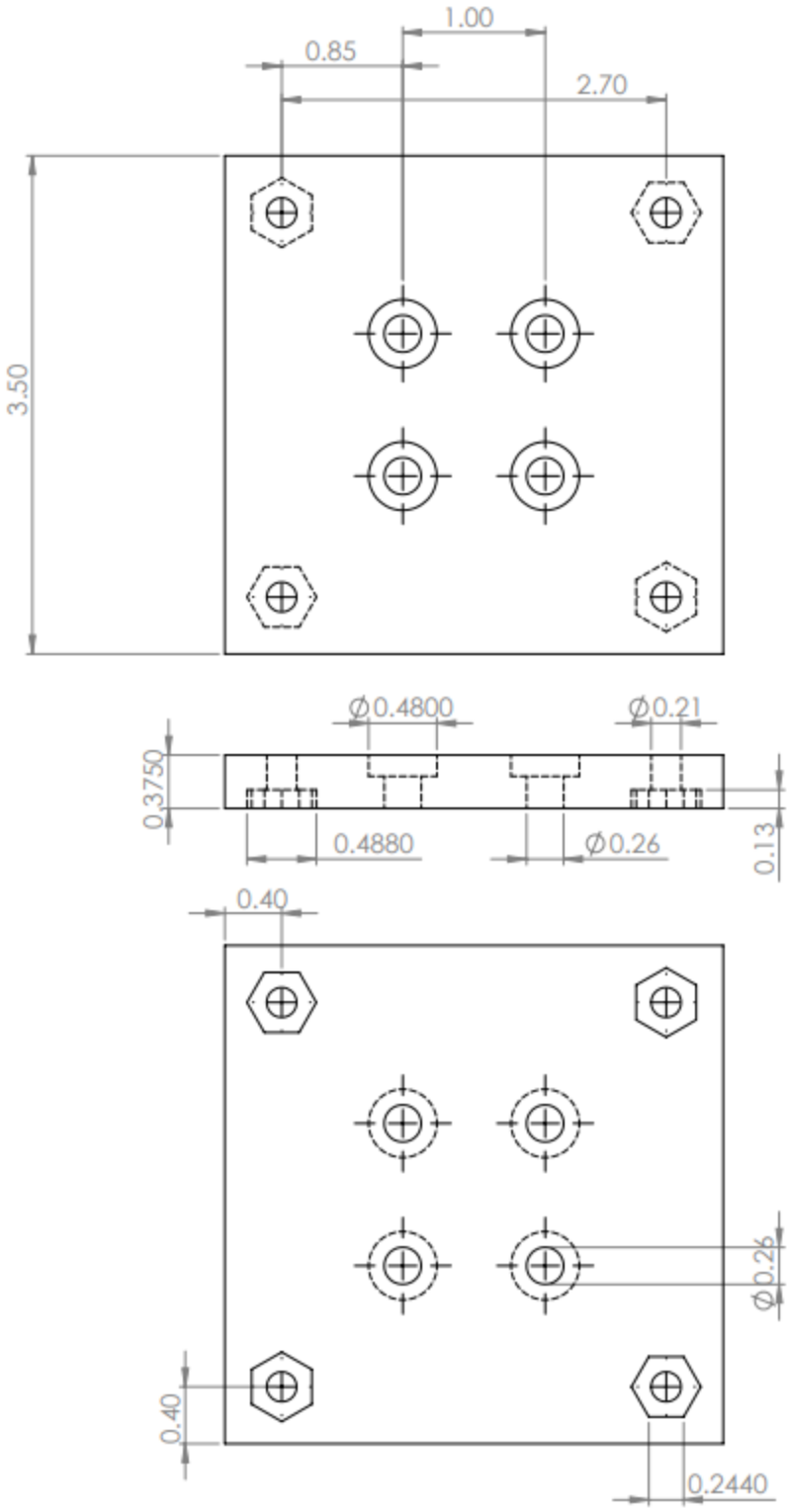

Figure 50. 80/20 Mount Engineering Drawing (IPS)

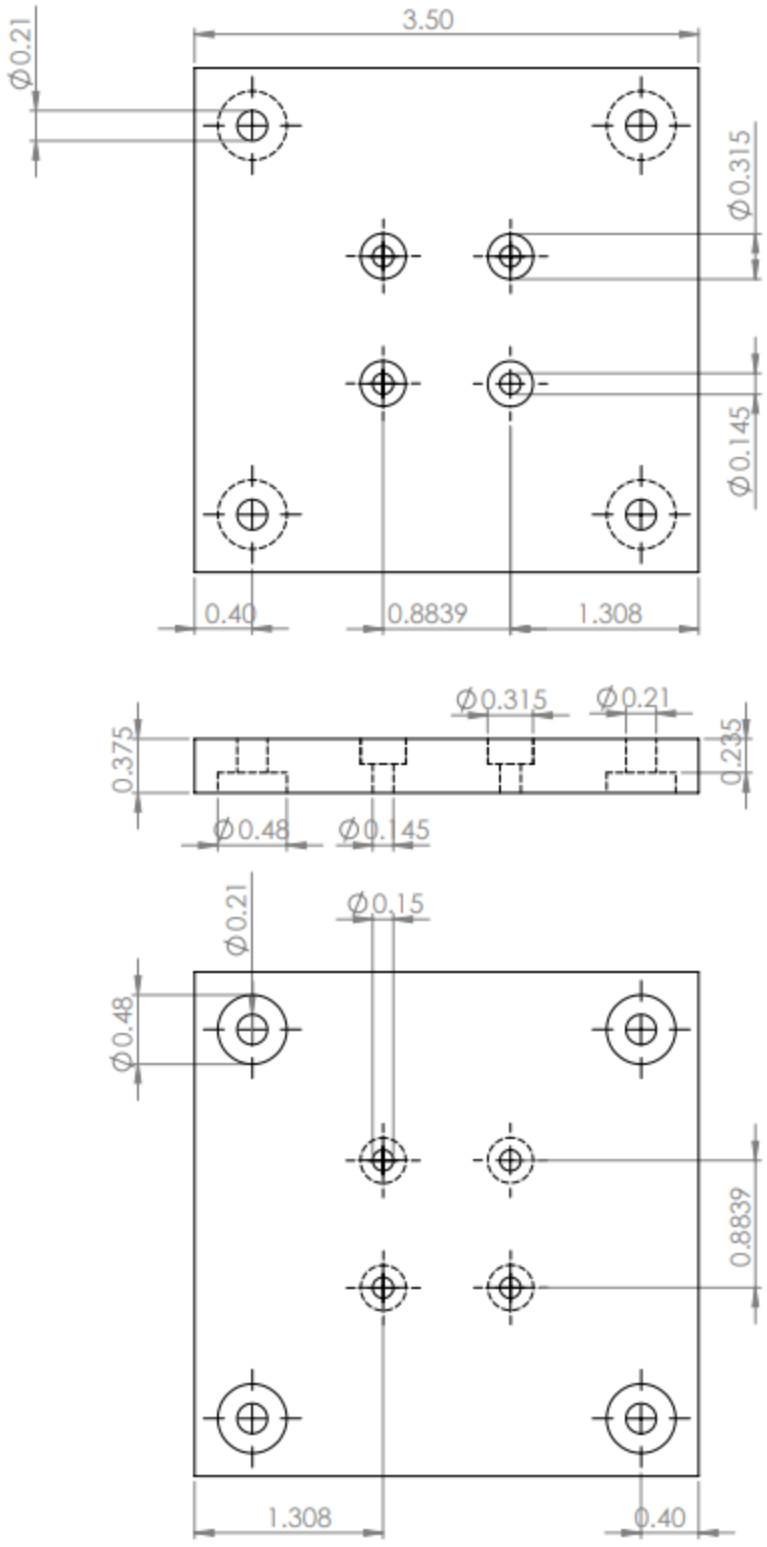

Figure 51. Sensor Mount 1 Engineering Drawing (IPS)

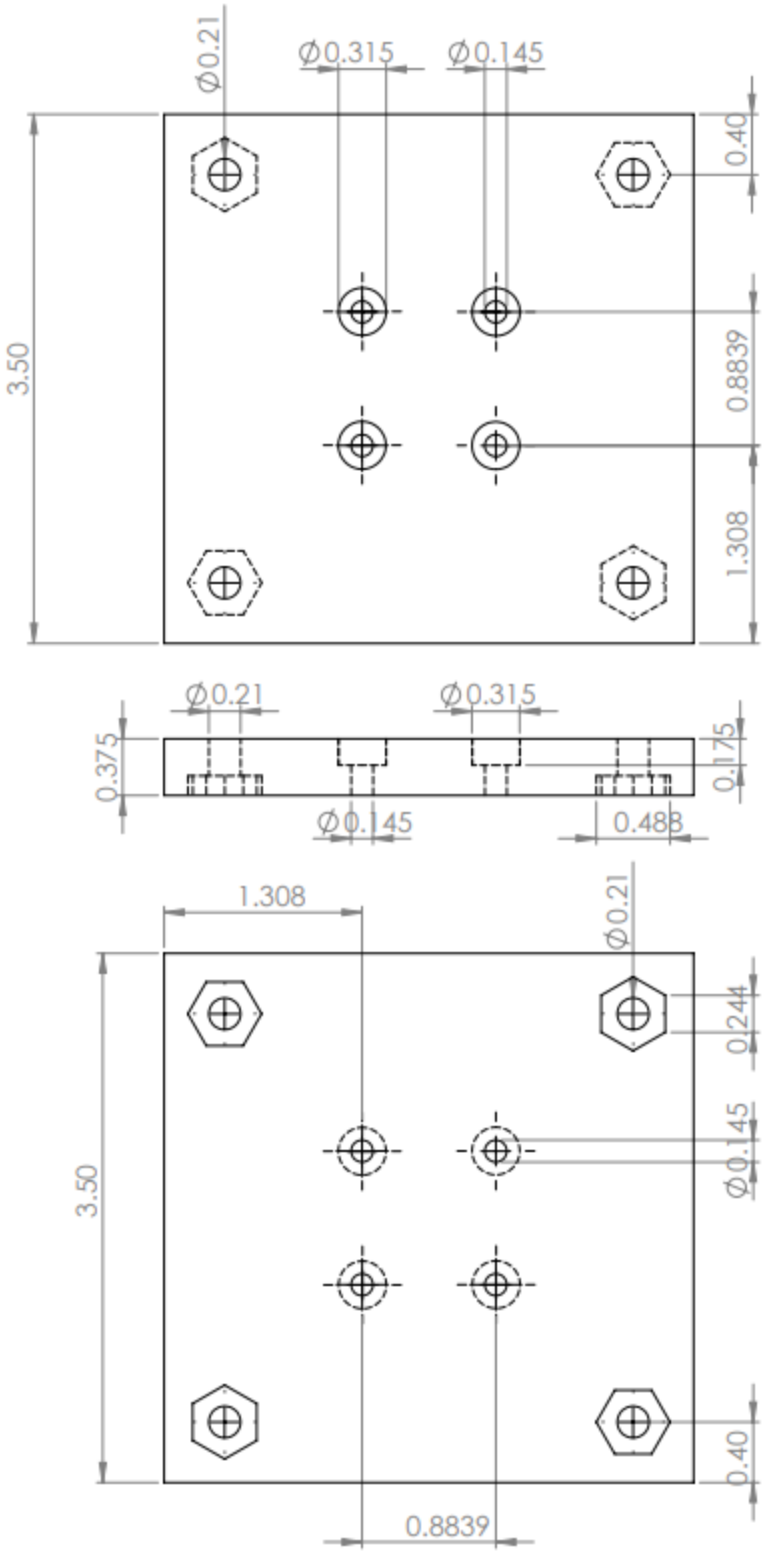

Figure 52. Sensor Mount 2 Engineering Drawing (IPS)

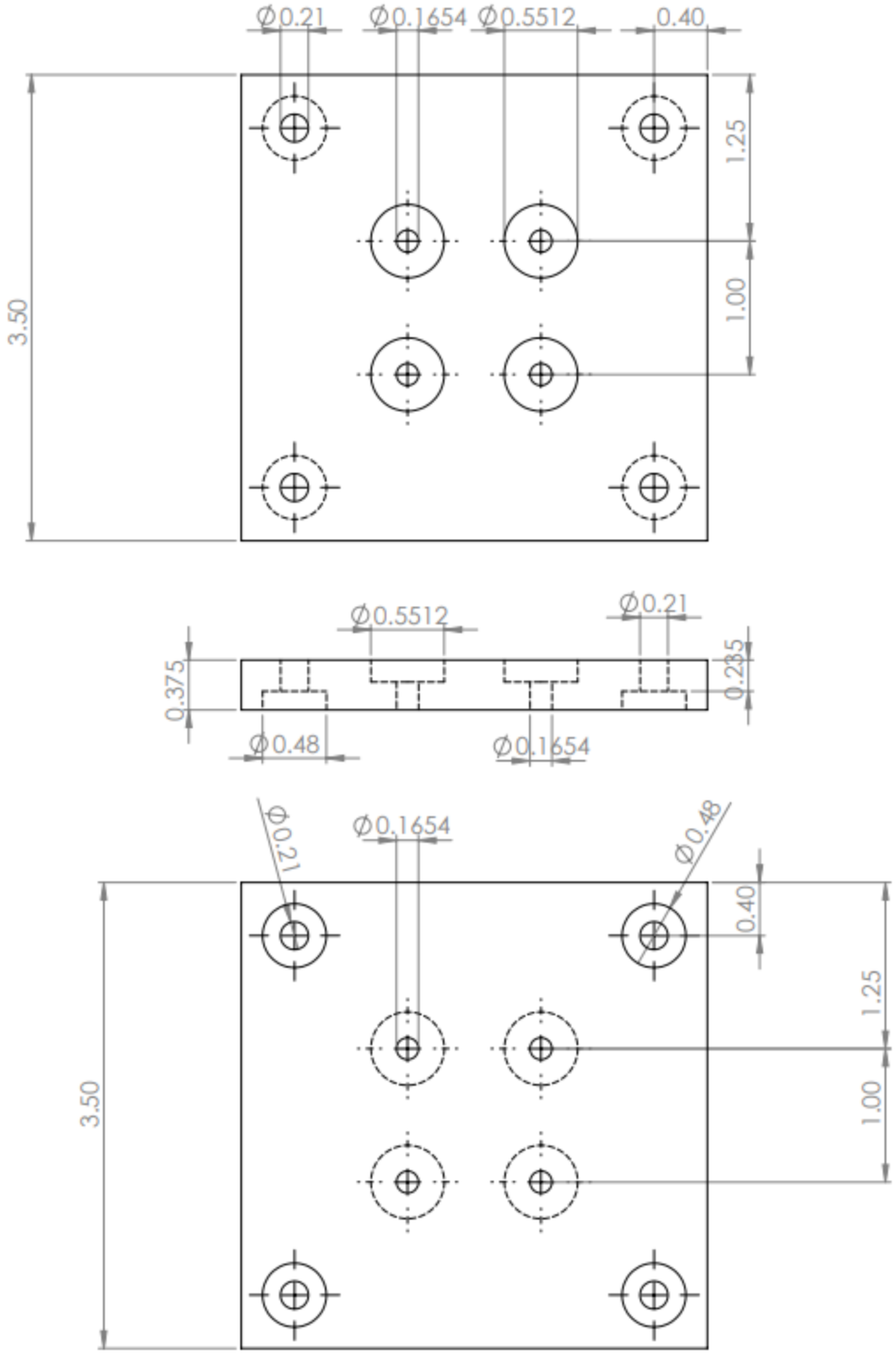

Figure 53. Motor Mount Engineering Drawing (IPS)

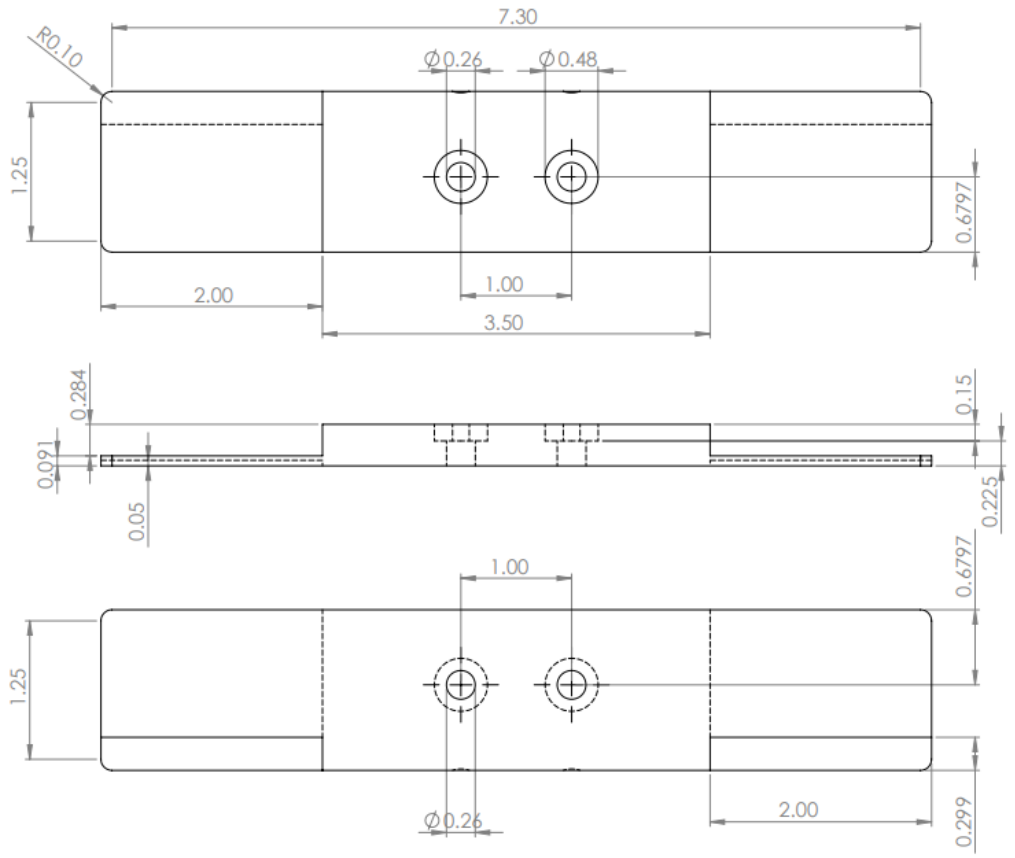

Figure 54. Amplifier Mount Engineering Drawing (IPS)

The assembled schematic consisting of all mount designs as well as the biaxial sensor and DC motor is shown in Figure 55. The way the mount connecting the sensor system to the 80/20 test stand is designed allows for it to be adjusted after being attached to the test stand. This is beneficial to data collection and protective against equipment damage as sensors and wiring can be vertically adjusted depending on the size of the rotor being tested.

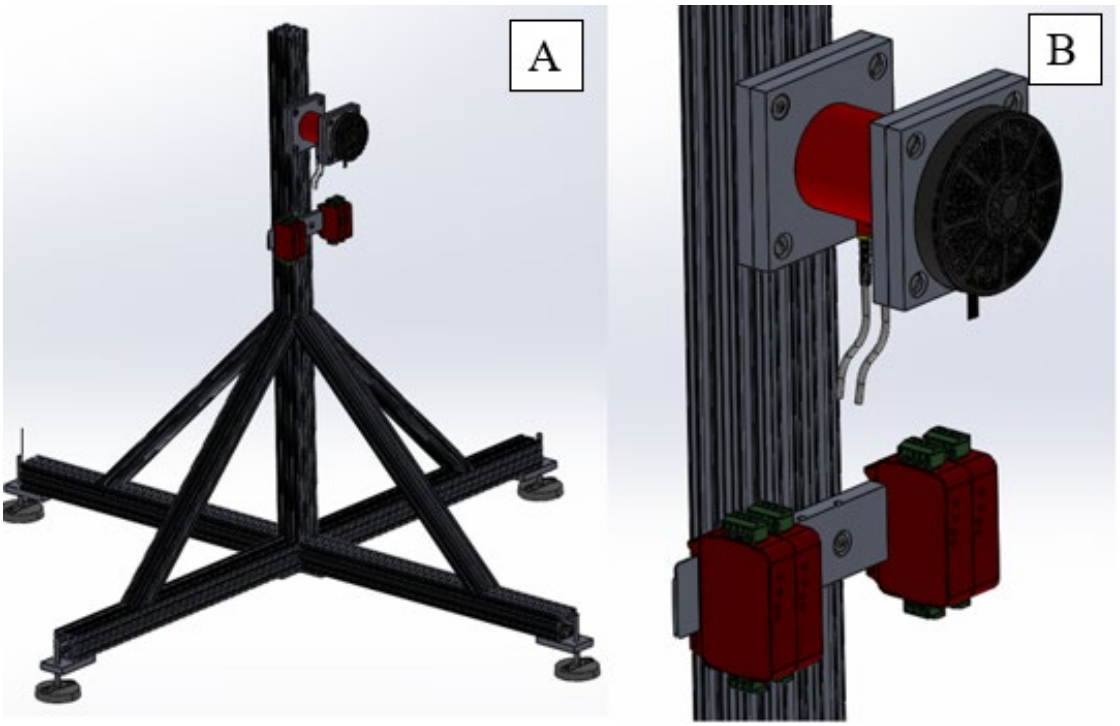

Figure 55. Assembled Mount Schematic (A) Zoomed In (B)

Figure 55 shows (A) the entire test stand, and (B) the individual components holding the sensor, motor, and amplifiers.

Figure 56 shows the front and backside images of the SOLIDWORKS design shown in Figures 45–49. The material used when printing these components was a white polycarbonate that was extruded out of a heated tip onto a printing platform. This allowed for vertical layers to be generated, of which the final results are seen in Figure 56 and 57.

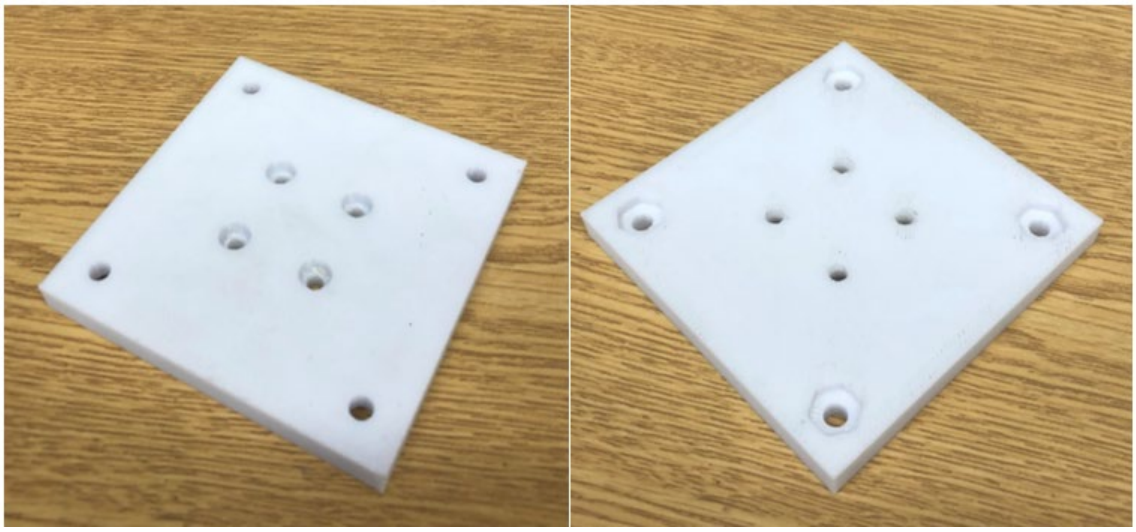

Figure 56. Printed Sensor Mount

In total four mount components were printed, each with slightly different geometries to account for the different equipment being mounted (torque and thrust sensors, electrical motors, and 80/20). The mount shown in Figure 56 is the piece that connects the electrical motor to the sensor.

The next unique component shown in Figure 57 is the amplifier mount. This mount holds the two amplifiers which collects the data being output by the torque and thrust sensor and delivers this information to the National Instruments DAQ for post processing.

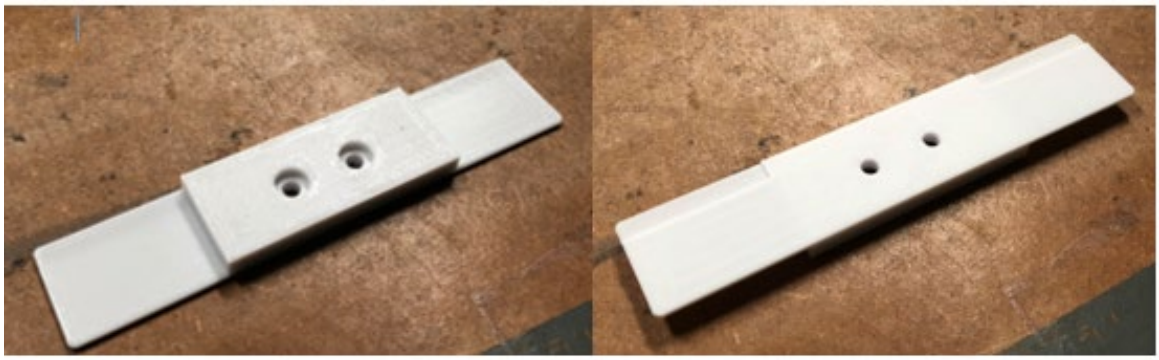

Figure 57. Printed Amplifier Mount

Finally, Figure 58 shows the partially assembled test stand with the sensors and amplifiers connected. The missing components in Figure 58 are the mounts that attach to the end of the sensor located at the top of the test stand. These mounts attach to the electrical motor and subsequently the T-Motor blade from which performance data is being collected from.

Figure 58. Assembled Test Stand

THIS PAGE INTENTIONALLY LEFT BLANK

APPENDIX C. DATA ACQUISITION AND STATION SETUP

Figure 59 shows the test stand with the rotor attached and the wiring complete for data acquisition.

Figure 59. Test Stand with Rotor

The rotor in Figure 59 is directly powered by the T-motor U8 Lite KV85 motor, which in turn receives signals from a 60A Flame ESC. These components were individually selected to best meet the demanded performance characteristics of the drone

for the specific environment it would be operating in (experimental hover). Figure 60 shows both the motor (A) and the ESC (B) .

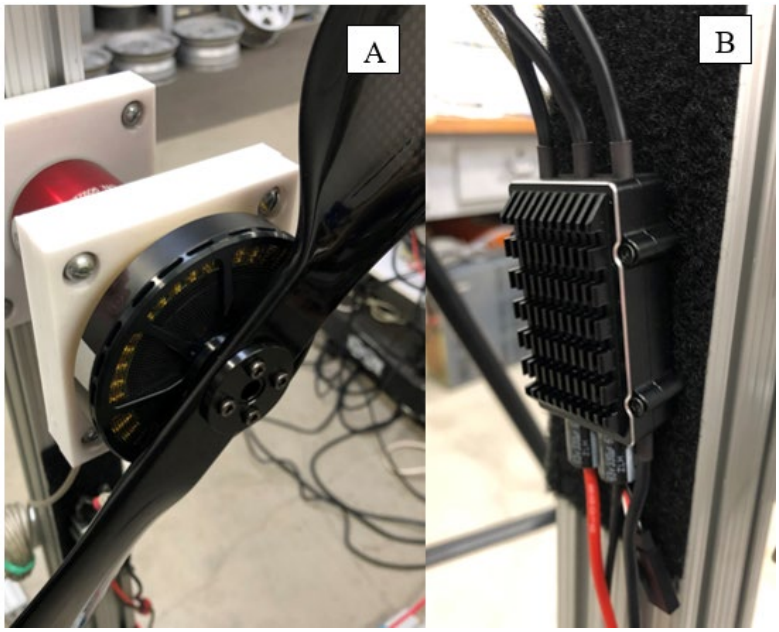

Figure 60. Test Stand Motor (A) and ESC (B)

The torque and thrust sensor which are located directly behind the rotor is fed into the two amplifiers placed near the base of the test stand. The motor driving the rotor is fed into the ESC which is electrically linked to the power supply (right image in Figure 60).

The output signal from the sensors is sent first to the NI DAQ (left image of Figure 61) which in turn compiles, converts from the respective electrical signals, and displays on a monitor for analysis the data obtained by the installed sensors.

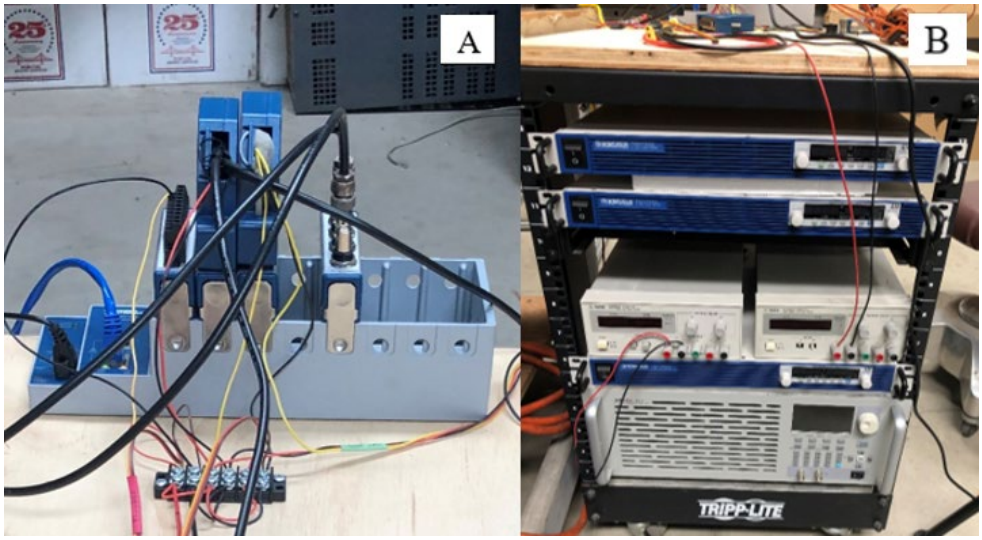

Figure 61. NI DAQ (A) and Power Supply (B)

The power supplies shown in Figure 61 (B) provided the rated excitation voltage for the sensors. Signals and data from the ESC and sensors were fed through the DAQ and into the monitors and oscilloscope shown in Figure 62.

Figure 62. Display Setup

The duty cycle of the ESC was altered on the display monitor through the National Instruments software. The assigned duty cycle in turn dictates the rotational velocity at which the rotor spins. A multimeter displayed the output voltage that corresponds to either the thrust or torque value at the demanded RPM.

APPENDIX D. LOAD, TORQUE AND LIFT CURVES

Prior to any experimental data acquisition on the test stand shown in Appendix C, the sensor had to be calibrated. This was done via a controlled loading and unloading while recording the output voltages during each incremental load change. The load calibration curve in Figure 63 was obtained by orienting the sensor vertically and placing incrementally heavier weights on the sensor creating an increasingly larger compressive load on the sensor.

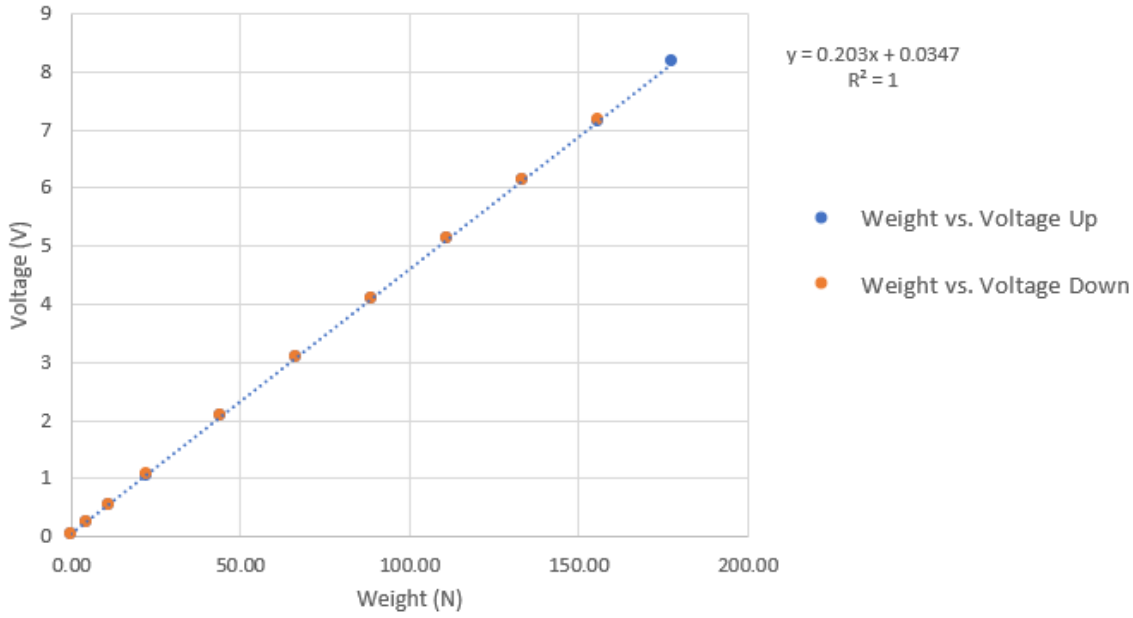

Figure 63. Voltage vs. Weight Calibration Curve

The respective voltage values were recorded at each load step (voltages were negative values as the load was compressive). Two calibration data sets were generated by both loading and unloading the sensor. Figure 64 shows the values of the data obtained for torque curves.

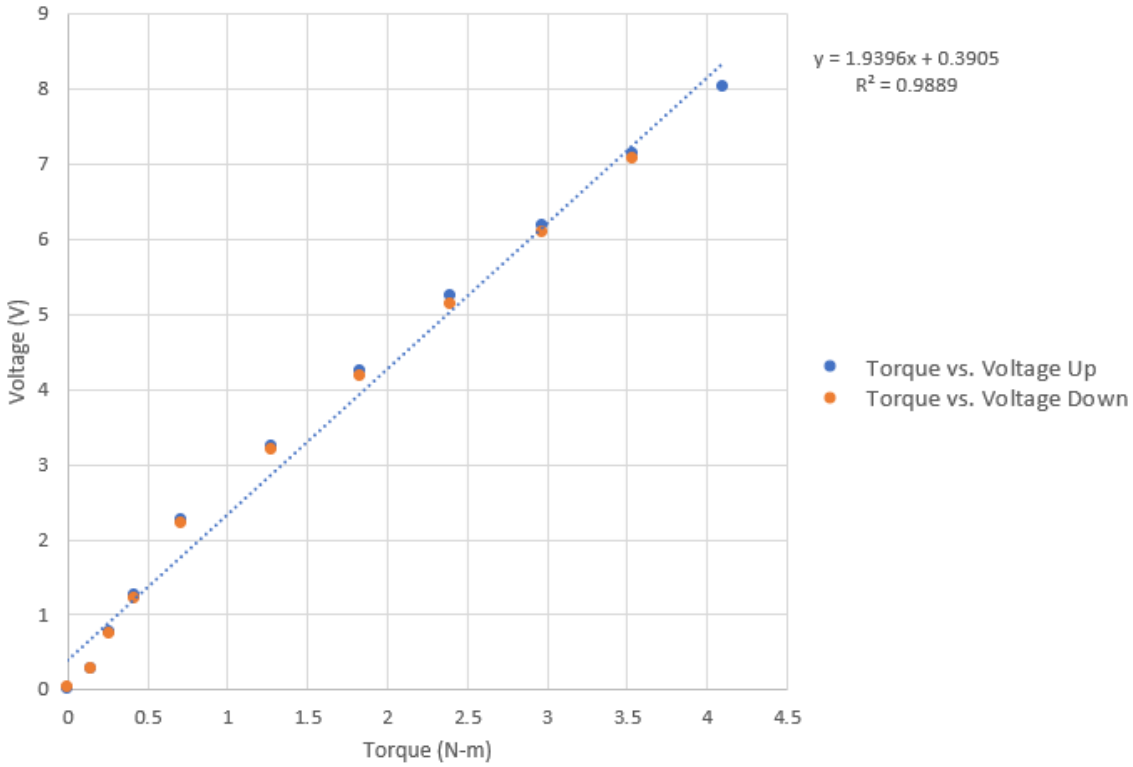

Figure 64. Voltage vs. Torque Calibration Curve

The same process used to obtain Figure 63 was used to produce Figure 64. The sensor was oriented horizontally and a sensor mount (Figure 46) was used as a lever arm. A hole was drilled 25.4mm from center of the sensor mount and a weight tray weighing 0.1469Nm was attached. Weights were placed on this tray which created a torque equivalent to the mass of the tray and weights multiplied by the distance from the origin of rotation (25.4mm). Similar to the load calibration curve, the measured torque was obtained via loading and unloading the sensor.

APPENDIX E. SOLIDWORKS CONTROL VOLUME SETUP

In order to generate an accurate model of the three-dimensional fluid flow over a blade, an accurate blade model and subsequent control volume needed to be generated. The company that manufactured the specific blade model being used for this analysis, T-Motor, was contacted about providing a CAD, specifically SOLIDWORKS, file containing the baseline blade model being used in this study, the 28”x9.2” (diameter and pitch), shown in Figure 65.

Figure 65. T-Motor G28x9.2 Prop-4PCS

T-Motor did not respond to the request. The alternative method taken to obtain the blade model was to access the open source website www.GrabCAD.com [27]. Here a user generated SOLIDWORKS model was found and downloaded for use in this study. Figure 66, shows the original SOLIDWORKS model of the 28”x9.2” blade as downloaded off of GrabCAD.

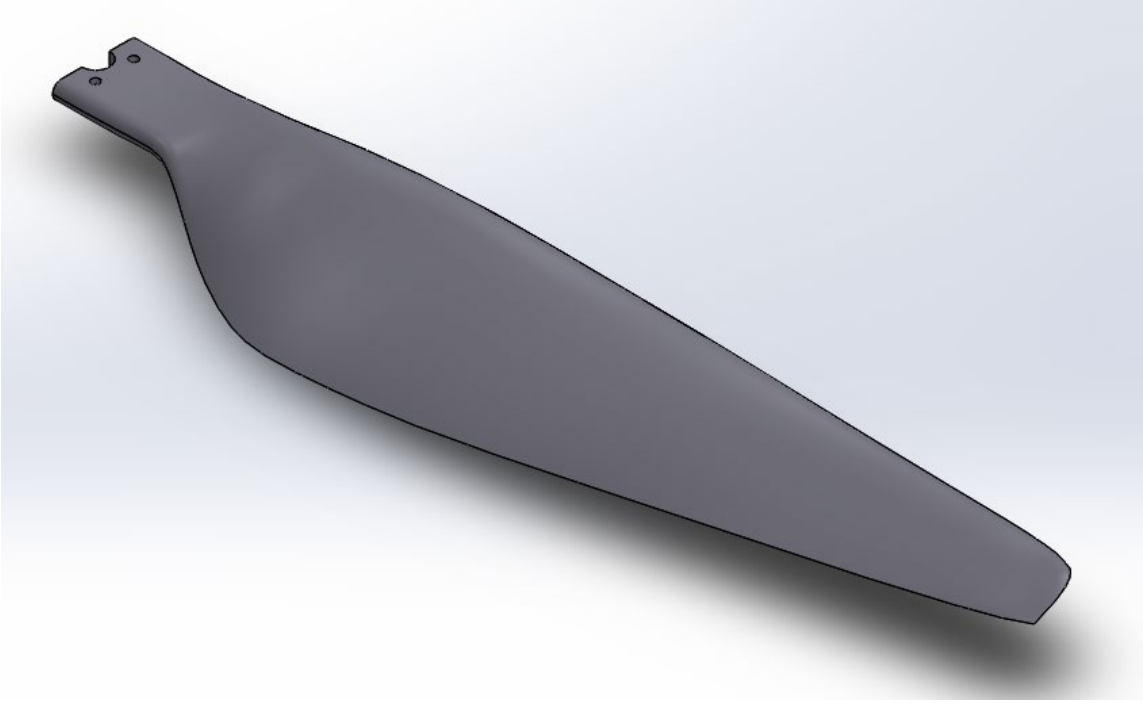

Figure 66. GrabCAD 28”x9.2” T-Motor Blade. Source: [27].

The blade model shown in Figure 66 is not the final blade model used for the numerical analysis. A single modification was made to the open source model in order to simplify the simulation. At the hub of the blade in Figure 66, three holes are present which, for the physical blade, were used to connect the blade to the motor. These holes were eliminated from the SOLIDWORKS model. This has little effect on the final results as negligible lift and drag are generated over this portion of the blade. The blade over this connection interface will be housed directly above the motor, meaning that there is minimal air flux across the disc area created by blade rotation. Because the SOLIDWORKS file for the blade was obtained via an open source, its accuracy in comparison to the actual blade being analyzed needed to be confirmed. This process was done by conducting a 3D scan of the T-Motor blade seen in Figure 67. In order to obtain an acceptable scan, the blade first had to be dusted with a powder that would reflect the scanner’s beams which in turn would provide a surface plot of the blade. Figure 67 shows the blade surface dusted prior to scanning.

Figure 67. Powdered Blade

A variety of tools were placed underneath the blade in order to create contrast so that the scanner could differentiate the depth distances when scanning the blade. Plywood was used as the base in the background as it is minimally reflecting the scanning beams, reducing noise in the output file of the scan. Figure 68, shows the blade along with the scanning device post scanning.

Figure 68. Post-Scanning

In order to scan the blade properly, the scanner was held approximately 1 meter above the blade and was oscillated starting at the hub of the blade, moving radially toward the tip, and back toward the hub multiple times to acquire an accurate topography of the blade's upper surface. The product of this scan was a coarse blade profile. This profile did not need to include the fine details, but rather needed to obtain the general geometry of the blade, specifically the pitch along the radius of the blade. The generated scan file was imported to SOLIDWORKS where an assembly consisting of the scanned file and the file obtained via open source (Figure 64) was constructed. The overlapped open source and scanned blades are shown in Figure 69.

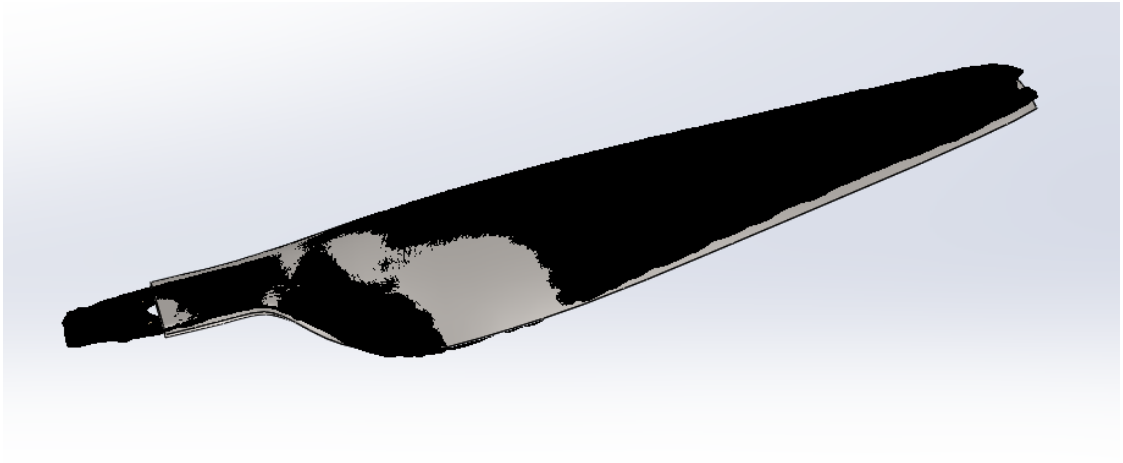

Figure 69. Overlapped Scanned and Open Source Blade

The open-source blade is shown in grey in this figure while the scanned blade is represented by the black mesh appearing across the surface. As is seen, the geometries between the two blades pitch and diameter match, which is the primary concern for the scan. One difference that would introduce error into simulation results was the open source blade having a sharp leading edge rather than an elliptical one, which is the typical shape of subsonic airfoils. The final blade model used is shown in Figure 70.

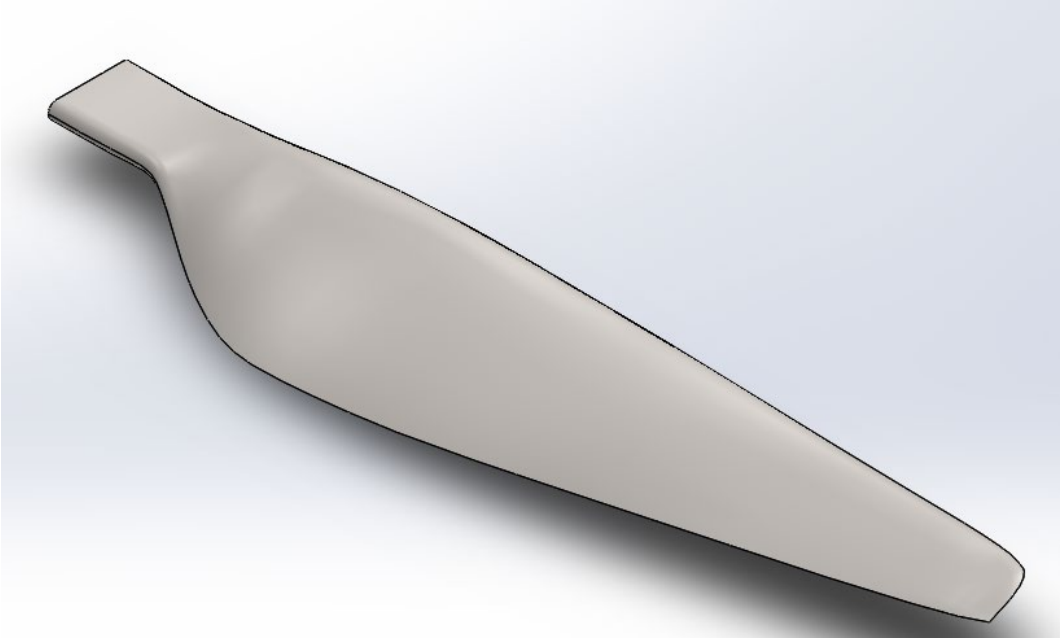

Figure 70. Modified T-Motor Blade

Using the modified blade seen in Figure 70, the fluid domain discussed in Chapter II was generated. During the meshing process, the fluid domain is design to have the finest mesh nearest to the blade. As the distance from the blade increases, the mesh becomes coarser. This allows for a computationally complex solution to be generated near the blade surface, capturing the whirl and tip-vortices flowing off the blade as it spins, while not wasting computational time on the flow behavior further away from the surface of the blade. The first step in creating the control volume discussed in Chapter II is to create a new SOLIDWORKS part file with the blade shown in Figure 70. It is recommended that a copy of the blade file is made so there is a reference file for the blade in addition to the generated control volume file. Before any fluid domain construction is done, the unit precision must be changed to the maximum number of significant figures. This can be done through the following sequence in SOLIDWORKS: Tools→Options→Document Properties→Dimensions→Set Primary Precision and Dual Precision to their maximum values. Figure 71 shows what the SOLIDWORKS display should look like.

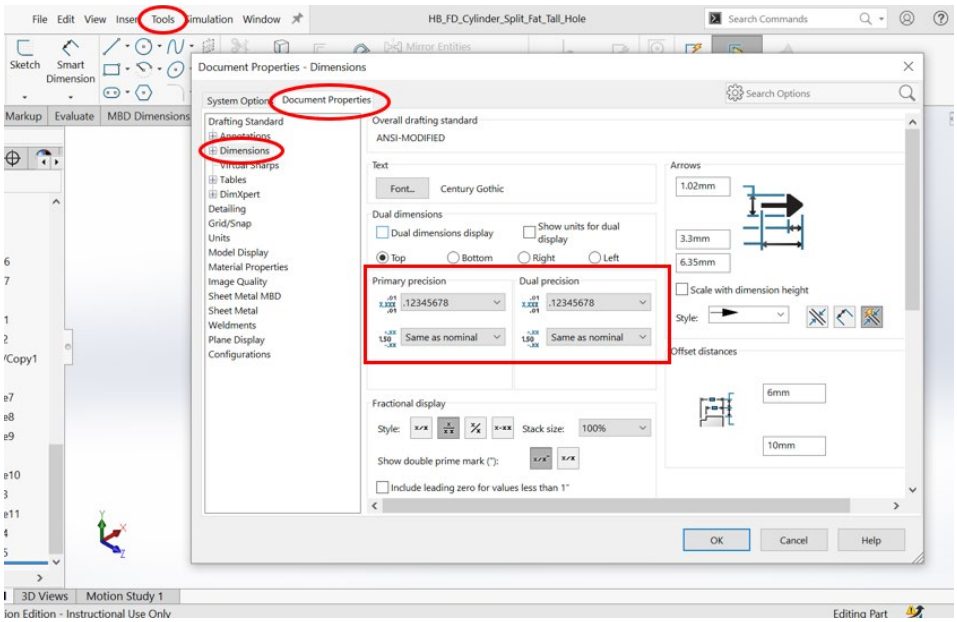

Figure 71. Increasing Primary and Dual Precision

Increasing the precision decreases the error at the interfaces of the fluid control volumes that will be generated. Following the completion of increasing the precision, fluid domain construction can begin. As seen in Figure 72, the blade and fluid domain are set to both occupy positive space, so the body of the domain will be extruded over the blade part.

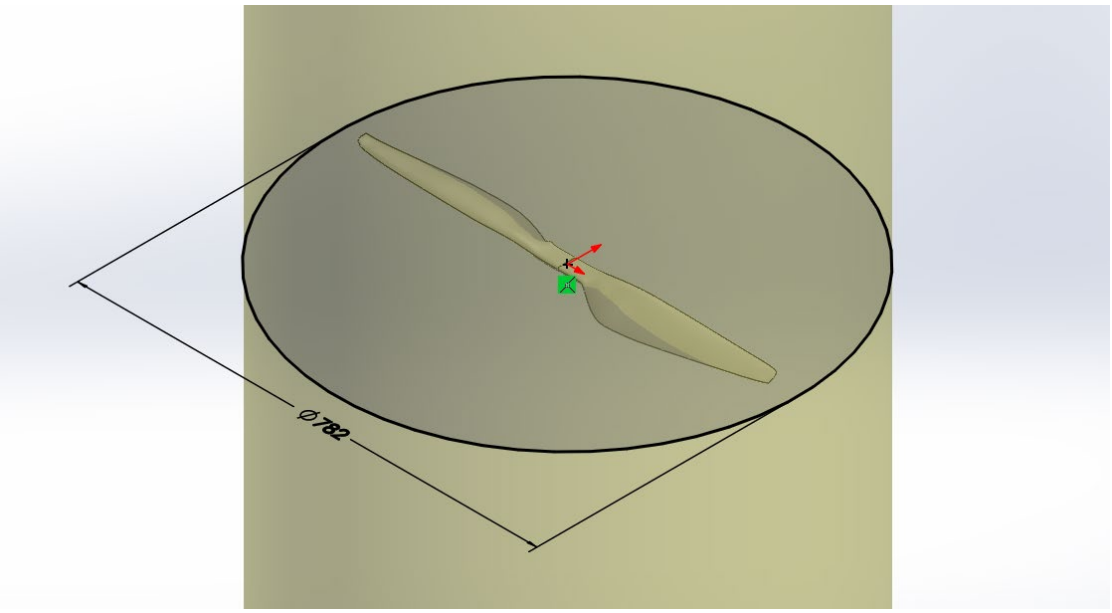

Figure 72. Fluid Domain Generation

After the cylindrical control volume is generated using the dimensions given Table 4, the “indent” feature, a built-in function of SOLIDWORKS, is used to cut the blade geometry from the fluid domain, creating a cavity where the blade was previously located. Figure 73 shows the configuration and selected geometries used to properly use the “indent” feature on a vertically cut plane of the fluid domain.

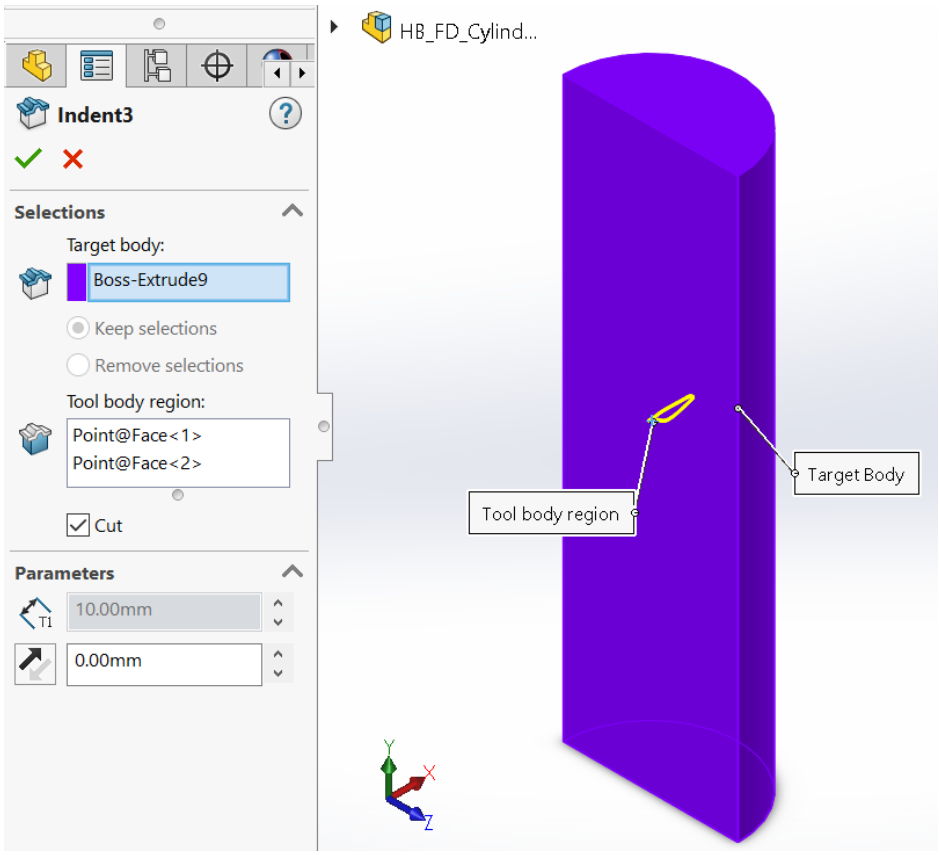

Figure 73. SOLIDWORKS Indent Configuration on Cut Plane

After making the blade negative space within the control volume, the final step before uploading the control volume to the simulation was to combine all bodies. By combining all the bodies (both the positive fluid domain and the negative blade geometry), time is saved in the importation and setup of the fluid domain. Figure 74 shows the method for combining the fluid domain and rotor bodies.

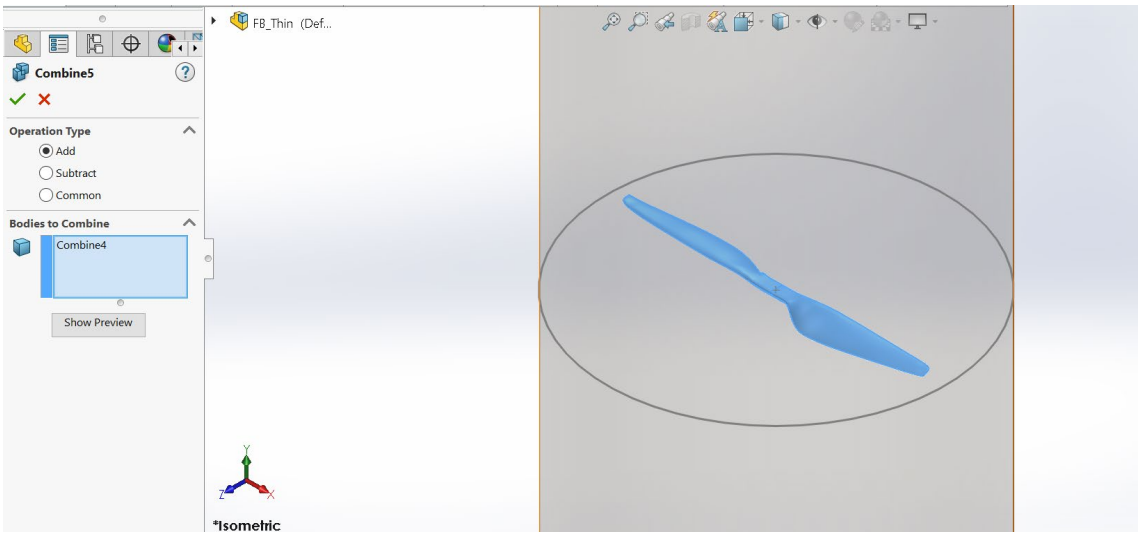

Figure 74. Combining Bodies

Because the rotor has already been indented from within the positive spaced of the control volume, the operation type is specified as “addition” as the negative space cut by the rotor is being added to the positive control volume space.

APPENDIX F. NUMERICAL MODEL SETUP, INPUTS AND RESIDUALS

A. GEOMETRY

Open ANSYS Workbench and begin with a clean workspace. ANSYS 19.2 is used for this modeling. From Figure 75, “Fluid Flow (CFX)” which is located in the left toolbox was selected and dragged onto the “Project Schematic”.

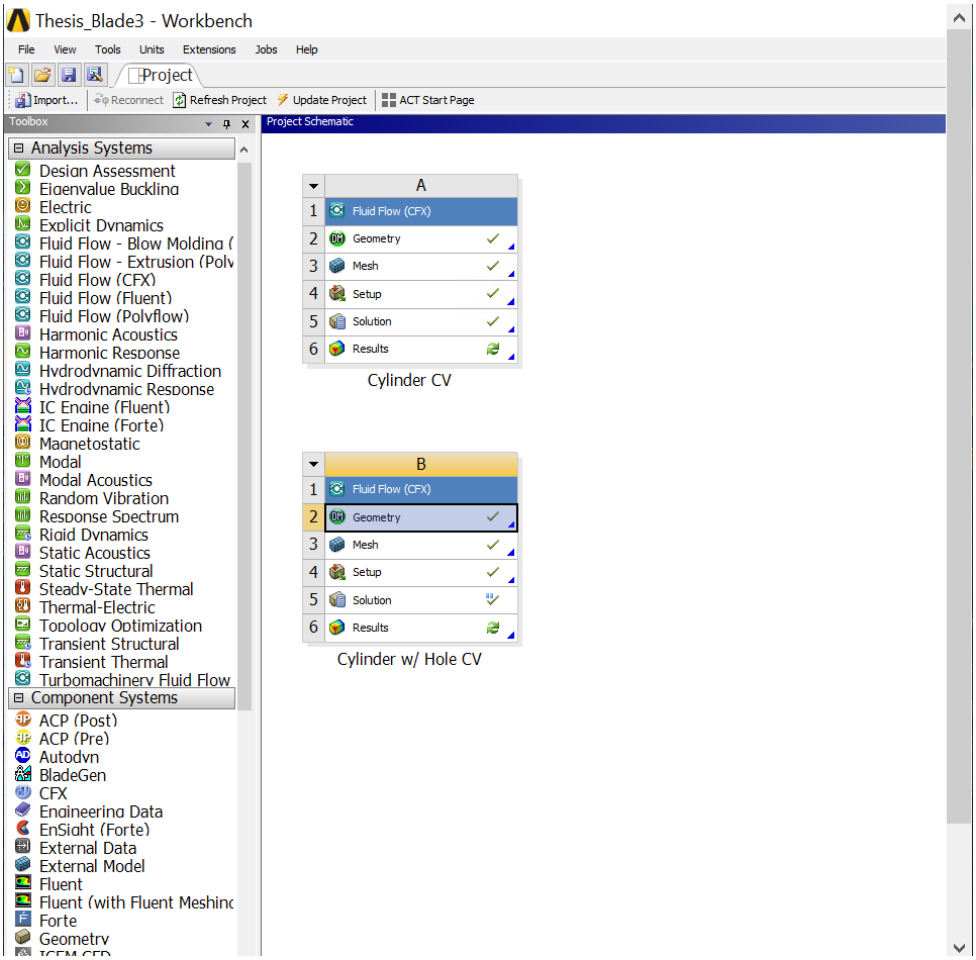

Figure 75. ANSYS GUI

This creates a new CFX simulation. To change the name of the simulation, the nomenclature underneath the newly created project is double clicked and the desired name

is changed. Before proceeding, the project must be saved in the same folder as the SOLIDWORKS file previously created.

The first tab available to be selected in the simulation window is titled “Geometry.” This tab is right clicked and the “Edit Geometry in DesignModeler” option should be selected. This opened a new window within which the control volume SOLIDWORKS file was imported. In the new window, External geometry is imported by selecting the “Import External Geometry File” option found by clicking on the “File” tab in the toolbar. This opened the File Explorer application on the computer and from there the SOLIDWORKS file can be selected to import. Once imported, the model needs to be generated. This is done by selecting the “Generate” button located in the fourth tool bar from top with a yellow lightning bolt. Figure 76 shows the display following model generation.

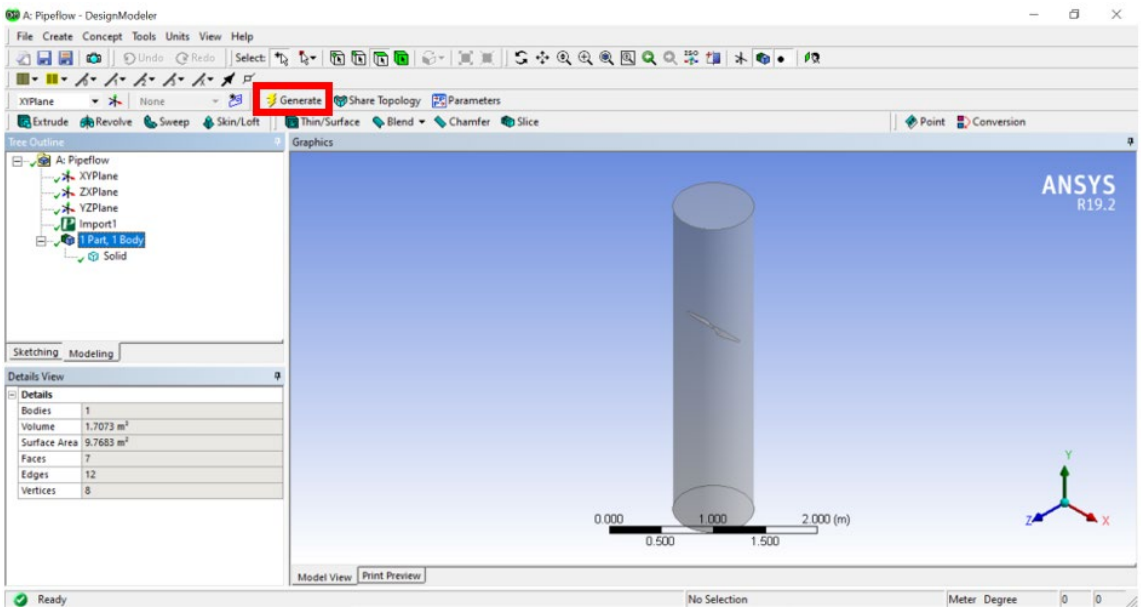

Figure 76. Design Modeler Display

Following generation of the SOLIDWORKS model in the DesignModeler, the Tree Outline located on the left side of the display populated with the imported model, labeled as “Import1.” Expanding the tab below the import label displays the number of unique bodies in the model. In Figure 76, there is only a single unique body present in the imported

SOLIDWORKS model due to combining all the bodies before importation. Selecting the body and then clicking F2 allows for the body's name to be changed to "Fluid Domain," for example. After every unique body is properly named the project can be saved and the DesignModeler tab exited out of to return to the ANSYS Workbench.

B. MESH

Table 5 shows the mesh refinement steps taken on the fluid domain as well as the corresponding important sizing values for each refinement step.

Table 5. Meshing Methods

Meshing Method	Specifications
Face Sizing	Element Size: 1mm
Inflation Layers	7 layers | Total Thickness: 2mm
Sphere of Influence (2)	Sphere Radius: 30mm | Element Size: 1mm

In Table 5 it is seen that the meshing method between both the pipe flow and open flow simulations are the same. The remaining information from the CFX simulation is shown and can be obtained from CFX-Post.

C. EXPRESSIONS

Table 6. Expression Names and Equations

Accumulated Time Step	23093
Angular Velocity	1800 [rev min^-1]
Cl	(Cltop/Clbot)
Clbot	0.5 * ave(Density)@ThesisPolyline * (omega*ave(Radius)@ThesisPolyline*pi/180)^2 * (sum(abs(Length*sineTheta))@ThesisPolyline/2)
Cltop	sum(Pressure*Length*sineTheta)@ThesisPolyline
Current Time Step	23093
Fbot	sum(Pressure*Area)@polylinexzpl bot
FpL	sum(Length)@ThesisPolyline
Ftop	sum(Pressure*Area)@polylinexzpl
Ftot	Fbot-Ftop

Table 6 continued

Lift Per Span	PVert*PolyLength
PVert	sum(Pressure*sin(Theta))@ThesisPolyline
PolyLength	sum(Length)@ThesisPolyline
Practice	(sum(abs(Length*sineTheta))@ThesisPolyline/2)
Ptotal	(Fbot/sum(Area)@polylinexzpl bot)-(Ftop/ sum(Area)@polylinexzpl)
Reference Pressure	1 [atm]
Sequence Step	23093
Time	0 [s]
Vavg	omega*ave(Radius)@ThesisPolyline*pi/180
Vbot	massFlowAve(Velocity in Stn Frame v)@polylinexzpl bot
Vtop	massFlowAve(Velocity in Stn Frame v)@polylinexzpl
Atstep	Accumulated Time Step
Ctstep	Current Time Step
Omega	Angular Velocity
Radii	sqrt((X)^2 + (Z)^2)
sineTheta	(Boundary Normal on ThesisPolyline Y) / (sqrt((Boundary Normal on ThesisPolyline Y)^2 + (Boundary Normal on ThesisPolyline Z)^2))
Sstep	Sequence Step
T	Time

ANSYS Report
ANSYS Logo: AnsysReportLogo.png
Date: 2022/03/22 10:30:35

Contents

---

1. File Report

Table 1. File Information for Pipeflow

Case	Pipeflow
File Path	C:\temp\Hobson Final_files\dp0\CFX-7\CFX\Pipeflow_013.res
File Date	07 March 2022
File Time	10:08:16 AM
File Type	CFX5
File Version	19.2

2. Mesh Report

Table 2. Mesh Information for Pipeflow

Domain	Nodes	Elements
FD	977766	3519224

3. Physics Report

Table 3. Domain Physics for Pipeflow

Domain - FD

Type	Fluid
Location	B16

Materials

Air Ideal Gas

Fluid Definition	Material Library
Morphology	Continuous Fluid

Settings

Buoyancy Model	Non Buoyant
Domain Motion	Rotating
Alternate Rotation Model	On
Angular Velocity	1.8000e+03 [rev min^-1]
Axis Definition	Coordinate Axis
Rotation Axis	Coord 0.2

Reference Pressure 1.0000e+00 [atm]
Heat Transfer Model Total Energy
Include Viscous Work Term True
Turbulence Model SST
Turbulent Wall Functions Automatic
High Speed Model Off

Table 4. Boundary Physics for Pipeflow
Domain Boundaries
FD Boundary - Inlet
Type INLET
Location F21.16
Settings
Flow Regime Subsonic
Heat Transfer Stationary Frame Total Temperature
Stationary Frame Total Temperature 2.8815e+02 [K]
Mass And Momentum Cartesian Velocity Components
U 0.0000e+00 [m s^-1]
V -1.0000e+00 [m s^-1]
W 0.0000e+00 [m s^-1]
Turbulence Medium Intensity and Eddy Viscosity Ratio
Boundary - Outlet
Type OUTLET
Location F20.16
Settings
Flow Regime Subsonic
Mass And Momentum Cartesian Velocity Components
U 0.0000e+00 [m s^-1]
V -1.0000e+00 [m s^-1]
W 0.0000e+00 [m s^-1]
Boundary - Blade
Type WALL
Location "F23.16, F22.16, F18.16, F17.16"
Settings
Heat Transfer Adiabatic
Mass And Momentum No Slip Wall
Wall Roughness Smooth Wall
Boundary - Cylinder
Type WALL
Location F19.16
Settings
Heat Transfer Adiabatic
Mass And Momentum Free Slip Wall

D. OPEN FLOW NUMERICAL SIMULATION REPORT

ANSYS Report
ANSYS Logo: AnsysReportLogo.png
Date: 2022/04/11 15:49:48

Contents

---

1. File Report

Table 1. File Information for Pipeflow Wide Diameter

Case	Pipeflow Wide Diameter
File Path	C:\temp\Thesis_Blade3_files\dp0\CFX-9\CFX\Pipeflow_027.res
File Date	11 April 2022
File Time	03:39:04 PM
File Type	CFX5
File Version	19.2

2. Mesh Report

Table 2. Mesh Information for Pipeflow Wide Diameter

Domain	Nodes	Elements
FD	988391	3577639

3. Physics Report

Table 3. Domain Physics for Pipeflow Wide Diameter

Domain - FD		
Type	Fluid	
Location	B47	
Materials		
Air Ideal Gas		
Fluid Definition	Material Library	
Morphology	Continuous Fluid	
Settings		
Buoyancy Model	Non Buoyant	
Domain Motion	Rotating	
Alternate Rotation Model	On	
Angular Velocity	1.325e+03 [rev min^-1]	
Axis Definition	Coordinate Axis	
Rotation Axis	Coord 0.3	

Reference Pressure	1.0000e+00 [atm]
Heat Transfer Model	Total Energy
Include Viscous Work Term	True
Turbulence Model	SST
Turbulent Wall Functions	Automatic
High Speed Model	Off

Table 4. Boundary Physics for Pipeflow Wide Diameter

Domain Boundaries	
FD Boundary - Inlet	
Type	INLET
Location	F52.47
Settings	
Flow Regime	Subsonic
Heat Transfer	Stationary Frame Total Temperature
Stationary Frame Total Temperature	2.8815e+02 [K]
Mass And Momentum	Cartesian Velocity Components
U	0.0000e+00 [m s^-1]
V	0.0000e+00 [m s^-1]
W	-1.0000e+00 [m s^-1]
Turbulence	Medium Intensity and Eddy Viscosity Ratio
Boundary - Outlet	
Type	OUTLET
Location	F51.47
Settings	
Flow Regime	Subsonic
Mass And Momentum	Cartesian Velocity Components
U	0.0000e+00 [m s^-1]
V	0.0000e+00 [m s^-1]
W	-1.0000e+00 [m s^-1]
Boundary - Blade	
Type	WALL
Location	F48.47, F49.47, F53.47, F54.47
Settings	
Heat Transfer	Adiabatic
Mass And Momentum	No Slip Wall
Wall Roughness	Smooth Wall
Boundary - Cylinder	
Type	WALL
Location	F50.47
Settings	
Heat Transfer	Adiabatic
Mass And Momentum	Free Slip Wall

E. ADDITIONAL OPEN FLOW RESULTS

Figure 77 shows the mass and momentum residuals of the open flow simulation. Similar to those residuals seen in the pipe flow simulation, each jump in the plot represents an increase in the rotational velocity of the model. The larger fluid domain used to simulate open flow increases the total number of iterations required to reach a quasi-steady state and subsequently lowers the step size of the speed increases.

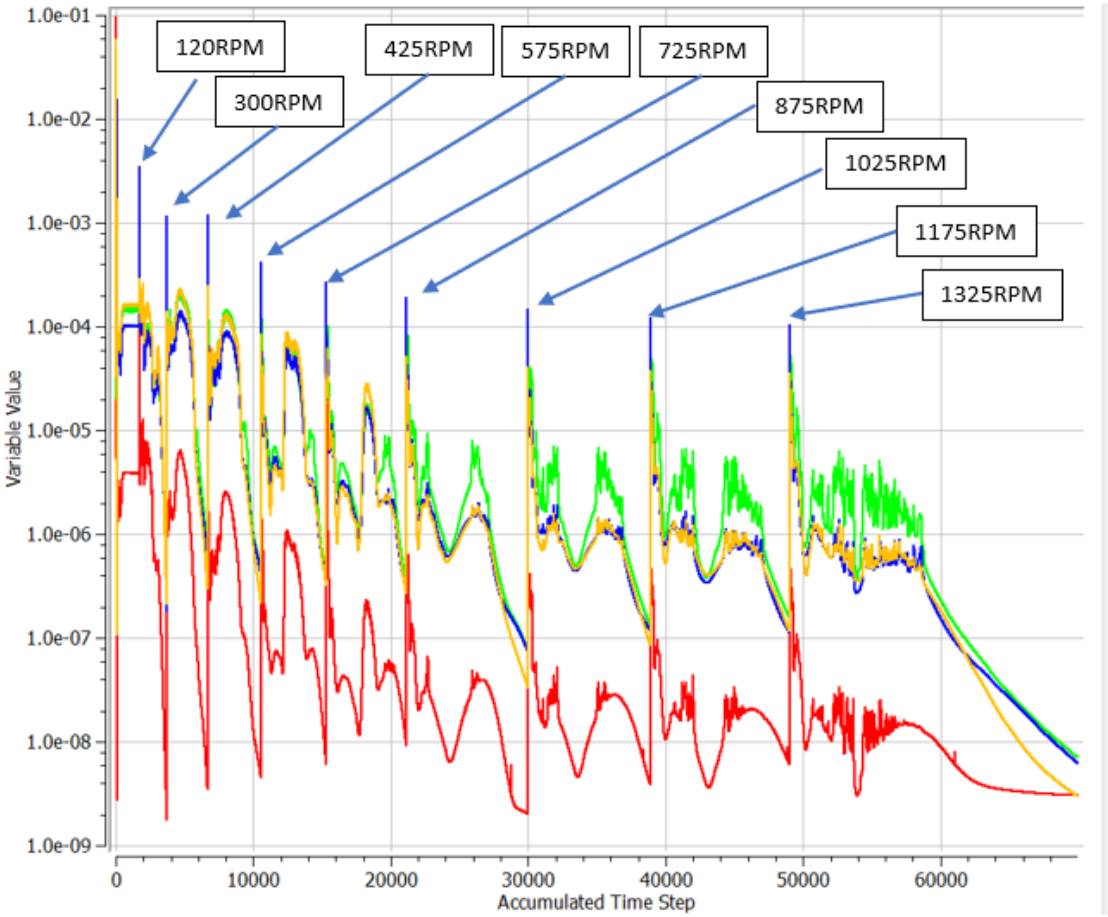

Figure 77. Mass and Momentum Residuals Open Flow

THIS PAGE INTENTIONALLY LEFT BLANK

APPENDIX G. METHODS FOR AVOIDING AND OVERCOMING NUMERICAL MODELLING ERRORS

Simulating three-dimensional fluid flow is difficult with respect to interfacing the fluid domains and meshing. Tactics used that resulted in non-viable solutions will be discussed. Figure 78 shows two fluid domains used in the early stages of analysis that did not produce correct results.

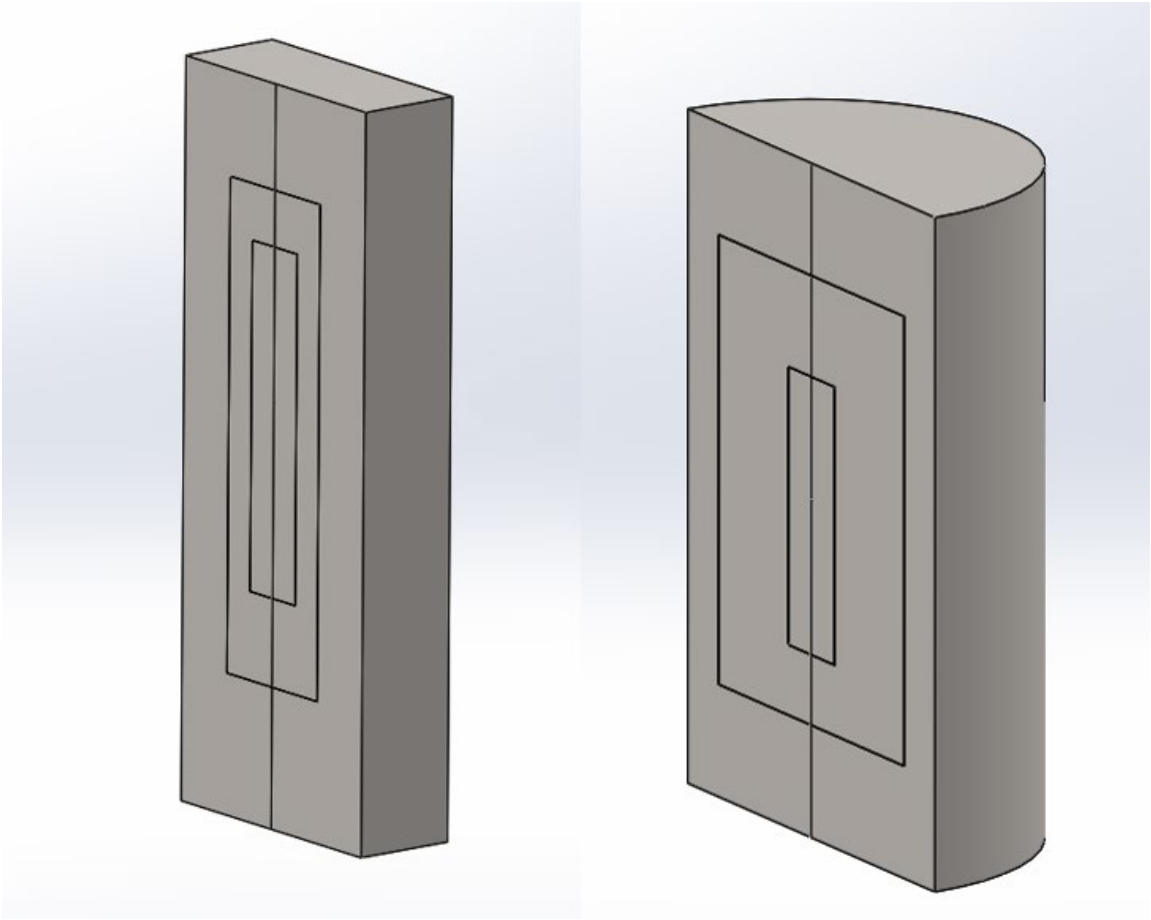

Figure 78. Erroneous Fluid Domains

A common error resulted between the two models seen in Figure 78. This error was discontinuities of fluid properties such as velocity and pressure across the domain interfaces. Implementation of face sizing control with the objective of having each fluid

domain's element face size match at the interface failed. Because the elements were different sizes at the interface, the transition of properties between the two bodies was discontinuous. Additionally, the boundary conditions imposed while using these fluid domains resulted in discontinuities. In Figure 78 the inner most fluid domain was specified as a rotating domain while the outer domains were stationary. This further complicated interface calculations due to the conversion of properties in the stationary frame to the rotational frame. For the left-most image in Figure 78 the rectangular geometry of all domains did not allow for a smooth rotation and periodicity to be imposed on the exposed face on the inner fluid domain. These fluid domains were quickly eliminated from analysis. In order for the simulation to remain stable and produce realistic results, the simplicity of the fluid domain had to be greatly increased. As is seen in the final fluid domain in Appendix E, concatenated fluid domains and periodic boundaries were eliminated, and with it also discontinuities of fluid properties.

Initially, when running the simulation on the fluid domain shown in Appendix E, overflow errors were common due to immediately imposing a rotational velocity of 1800RPM without initializing the flow field. Two methods were derived that solved this problem. The first, and most viable is the initialization of the flow field with a 1 m/s flow before imposing rotation on the fluid domain, and then slowly ramping up the speed of the domain rather than setting the speed immediately to its desired operational speed. The second method involved initially reducing the time step of the simulation, this process is shown in Figure 79.

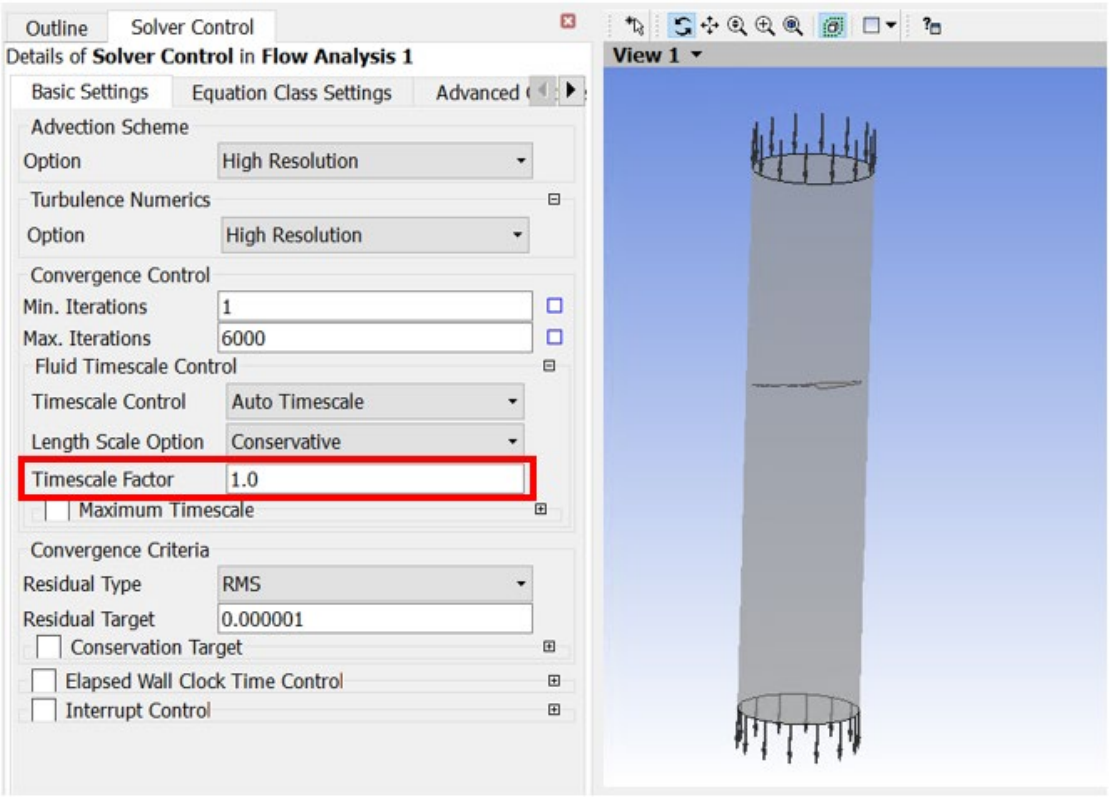

Figure 79. Timescale Factor Adjustment

By lowering this value by multiple orders of magnitude (discretion is used when choosing how low to set this value), the timestep taken in the simulation will correspondingly be reduced as well. After lowering the timescale factor, allow the simulation to run and reach a steady state. Once at steady state, increase the timescale factor by an order of magnitude and repeat until its value is unity. By doing this, the simulation is able to resolve smaller simulation challenges first and incrementally eliminate larger issues as the timescale factor is increased.

THIS PAGE INTENTIONALLY LEFT BLANK

APPENDIX H. POWER CONSUMPTION LOG

Terminal log file
Date: 11/5/2021 - 1:53:16 PM

HYCOPTER2_v1.9.2
DB3:Starting Up. System Init...
DB1:SDCard mounting error (1)
DB2:SDCard is not detected
DB2:Cannot determine FCS log filename
DB3:HGSPressure valid, 0.00
DB3:FCSPressure valid, 0.96
FCS=45.9V,00.00A,000.0W,000.00Wh,LD=34.7V, 27.1C,29.2C,29.2C,29.1C,TST=00.0C,PCB=028.3C, 0.98B,000.0PSIG, 20.0%,2,
DB3:HGS disabled
FCS=51.9V,00.03A,001.7W,000.00Wh,LD=35.2V, 27.1C,29.6C,29.4C,29.2C,TST=00.0C,PCB=027.3C, 0.87B,000.0PSIG, 20.0%,5,
FCS=49.8V,00.05A,002.5W,000.00Wh,LD=34.9V, 27.3C,29.6C,29.7C,29.5C,TST=00.0C,PCB=027.9C, 0.92B,000.0PSIG, 20.0%,5,
FCS=50.9V,00.04A,002.2W,000.00Wh,LD=35.2V, 27.6C,30.1C,29.9C,29.7C,TST=00.0C,PCB=028.6C, 0.77B,000.0PSIG, 20.0%,5,
FCS=50.0V,00.03A,001.5W,000.00Wh,LD=34.6V, 27.4C,29,000.0PSIG, 20.0%,5,
FCS=51.1V,00.07A,003.4W,000.00Wh,LD=34.8V, 27.8C,29.8C,30.0C,29.9C,TST=00.0C,PCB=027.2C, 0.80B,000.0PSIG, 20.0%,5,
FCS=49.7V,00.06A,003.0W,000.00Wh,LD=34.5V, 27.9C,30.0C,30.2C,30.0C,TST=00.0C,PCB=027.8C, 0.93B,000.0PSIG, 20.0%,5,
FCS=51.1V,00.07A,003.8W,000.00Wh,LD=34.9V, 28.0C,30.0C,30.2C,30.1C,TST=00.0C,PCB=029.1C, 0.72B,000.0PSIG, 20.0%,5,
/.5W,000.01Wh,LD=35.4V, 28.4C,30.2C,30.6C,30.4C,TST=00.0C,PCB=029.0C, 0.95B,000.0PSIG, 20.0%,5,
FCS=50.8V,00.09A,004.3W,000.01Wh,LD=35.4V, 28.5C,30.4C,30.8C,30.5C,TST=00.0C,PCB=028.7C, 0.71B,000.0PSIG, 20.0%,5,
FCS=50.0V,00.05A,002.4W,000.01Wh,LD=34.6V, 28.5C,31.0C,30.8C,30.5C,TST=00.0C,PCB=027.9C, 0.91B,000.0PSIG, 20.0%,5,
DB3:OPERATION_StateMachine_cFCS ...
FCS=49.5V,00.41A,020.5W,000.01Wh,LD=49.4V, 28.7C,31.4C,31.2C,30.6C,TST=39.7C,PCB=029.6C, 0.88B,000.0PSIG, 20.2%,6,
FCS=49.2V,00.69A,034.2W,000.02Wh,LD=49.1V, 29.2C,31.5C,31.4C,30.9C,TST=39.7C,PCB=027.9C, 0.95B,000.0PSIG, 20.5%,6,
FCS=48.4V,00.54A,025.9W,000.03Wh,LD=48.2V, 28.9C,31.2C,31.3C,30.7C,TST=39.7C,PCB=027.7C, 0.95B,000.0PSIG, 20.4%,6,
FCS=48.6V,00.57A,027.5W,000.03Wh,LD=48.2V, 29.0C,31.2C,31.3C,30.7C,TST=39.7C,PCB=029.9C, 0.93B,000.0PSIG, 20.4%,6,

FCS=48.7V,00.47A,022.8W,000.04Wh,LD=48.4V, 29.1C,31.3C,31.4C,30.8C,TST=39.7C,PCB=028.9C, 0.86B,000.0PSIG, 20.3%,6,
FCS=47.8V,00.61A,028.9W,000.05Wh,LD=48.9V, 29.3C,31.4C,31.6C,31.0C,TST=39.7C,PCB=029.0C, 0.97B,000.0PSIG, 20.4%,6,
FCS=48.1V,00.61A,029.1W,000.06Wh,LD=47.9V, 29.3C,31.3C,31.5C,30.9C,TST=39.7C,PCB=029.8C, 0.84B,000.0PSIG, 20.4%,6,
FCS=47.4V,00.51A,024.3W,000.06Wh,LD=47.2V, 29.2C,31.7C,31.5C,30.8C,TST=39.7C,PCB=027.8C, 0.96B,000.0PSIG, 20.3%,6,
FCS=48.7V,00.71A,034.6W,000.07Wh,LD=48.4V, 29.5C,32.0C,31.8C,31.2C,TST=39.7C,PCB=030.0C, 0.95B,000.0PSIG, 20.5%,6,
FCS=48.5V,00.62A,029.8W,000.08Wh,LD=48.1V, 29.4C,31.9C,31.7C,31.0C,TST=39.7C,PCB=030.0C, 0.98B,000.0PSIG, 20.4%,6,
FCS=49.3V,00.70A,034.5W,000.09Wh,LD=49.1V, 29.8C,32.1C,32.1C,31.4C,TST=39.7C,PCB=028C, 0.94B,000.0PSIG, 20.5%,6,
FCS=48.9V,00.52A,025.2W,000.10Wh,LD=48.7V, 29.6C,31.9C,31.8C,31.1C,TST=39.7C,PCB=029.2C, 0.93B,000.0PSIG, 20.3%,6,
FCS=48.9V,00.55A,026.7W,000.10Wh,LD=48.1V, 29.9C,32.2C,32.3C,31.5C,TST=39.7C,PCB=028.6C, 0.95B,000.0PSIG, 20.3%,6,
FCS=48.4V,00.68A,033.0W,000.11Wh,LD=48.8V, 30.0C,32.0C,32.3C,31.5C,TST=39.7C,PCB=028.7C, 0.95B,000.0PSIG, 20.5%,6,
FCS=47.8V,00.51A,024.6W,000.12Wh,LD=48.3V, 29.7C,31.8C,32.0C,31.2C,TST=39.7C,PCB=028.4C, 0.85B,000.0PSIG, 20.4%,6,
FCS=48.4V,00.56A,027.2W,000.13Wh,LD=48.2V, 30.1C,32.5C,32.4C,31.5C,TST=39.7C,PCB=028.0C, 0.94B,000.0PSIG, 20.4%,6,
FCS=48.4V,00.55A,026.4W,000.14Wh,LD=47.6V, 30.0C,32.6C,32.3C,31.3C,TST=39.7C,PCB=028.0C, 0.93B,000.0PSIG, 20.4%,6,
FCS=48.4V,00.54A,025.9W,000.14Wh,LD=47.5V, 29.9C,32.7C,32.1C,31.3C,TST=39.7C,PCB=028.5C, 0.92B,000.0PSIG, 20.4%,6,
FCS=49.1V,00.62A,030.4W,000.15Wh,LD=48.9V, 30.5C,32.7C,32.6C,31.7C,TST=39.7C,PCB=29.4C, 0.93B,000.0PSIG, 20.4%,6,
FCS=48.0V,00.66A,031.5W,000.16Wh,LD=47.6V, 30.3C,32.6C,32.5C,31.6C,TST=39.7C,PCB=028.9C, 0.88B,000.0PSIG, 20.4%,6,
FCS=49.6V,00.58A,029.0W,000.17Wh,LD=49.3V, 30.3C,32.5C,32.5C,31.6C,TST=39.7C,PCB=030.4C, 0.95B,000.0PSIG, 20.4%,6,
FCS=49.4V,00.56A,027.8W,000.18Wh,LD=48.7V, 30.4C,32.5C,32.7C,31.7C,TST=39.7C,PCB=029.9C, 0.97B,000.0PSIG, 20.4%,6,
FCS=49.1V,00.63A,030.9W,000.18Wh,LD=48.7V, 30.5C,32.5C,32.7C,31.7C,TST=39.7C,PCB=029.1C, 0.94B,000.0PSIG, 20.4%,6,
FCS=49.1V,00.60A,029.5W,000.19Wh,LD=48.5V, 30.4C,32.8}TæC,32.6C,31.6C,TST=39.7C,PCB=029.5C, 0.92B,000.0PSIG, 20.4%,6,
FCS=48.5V,00.72A,034.8W,000.20Wh,LD=49.4V, 30.9C,33.2C,33.0C,32.0C,TST=39.7C,PCB=029.4C, 0.93B,000.0PSIG, 20.5%,6,
FCS=49.2V,00.70A,034.5W,000.21Wh,LD=48.7V, 30.9C,33.7C,33.0C,31.8C,TST=39.7C,PCB=031.3C, 0.98B,000.0PSIG, 20.5%,6,
FCS=48.5V,00.71A,034.3W,000.22Wh,LD=49.2V, 30.7C,33.4C,33.0C,31.9C,TST=39.7C,PCB=029.1C, 0.95B,000.0PSIG, 20.5%,6,
FCS=48.6V,00.57A,027.6W,000.23Wh,LD=48.1V, 30.4C,32.7C,32.5C,31.4C,TST=39.7C,PCB=029.7C, 0.95B,000.0PSIG, 20.4%,6,
FCS=49.0V,00.59A,029.1W,000.23Wh,LD=47.9V, 30.9C,33.1C,33.0C,31.9C,TST=39.7C,PCB=028.6C, 0.95B,000.0PSIG, 20.4%,6,
FCS=48.6V,00.75A,036.5W,000.=39.7C,PCB=028.6C, 0.8
FCS=49.1V,00.58A,028.4W,000.25Wh,LD=48.8V, 30.8C,32.7C,32.9C,31.7C,TST=39.7C,PCB=027.5C, 0.95B,000”_w□À¢•—³u.0PSIG, 20.4%,6,
FCS=48.4V,00.59A,028.6W,000.26Wh,LD=48.3V, 30.9C,33.0C,32.9C,31.8C,TST=39.7C,PCB=028.4C, 0.96B,000.0PSIG, 20.4%,6,
FCS=48.6V,00.52A,025.5W,000.27Wh,LD=47.9V, 30.7C,33.0C,32.7C,31.6C,TST=39.7C,PCB=027.5C, 0.94B,000.0PSIG, 20.3%,6,

FCS=48.4V,00.56A,027.0W,000.28Wh,LD=48.2V, 30.9C,33.3C,32.9C,3027.1C, 0.95B,000.0PSIG, 20.4%,6,
FCS=48.2V,00.53A,025.6W,000.28Wh,LD=48.0V, 31.1C,33.7C,33.1C,31.8C,TST=39.7C,PCB=028.1C, 0.86B,000.0PSIG, 20.3%,6,
FCS=48.4V,00.54A,026.0W,000.29Wh,LD=48.4V, 31.1C,33.3C,33.0C,31.9C,TST=39.7C,PCB=029.1C, 0.92B,000.0PSIG, 20.3%,6l
FCS=48.1V,00.48A,022.9W,000.30Wh,LD=47.1V, 30.9C,33.0C,32.8C,31.6C,TST=39.7C,PCB=027.1C, 0.95B,000.0PSIG, 20.3%,6,
FCS=47.4V,00.50A,023.7W,000.30Wh,LD=48.4V, 30.9C,32.8C,32.9C,31.7C,TST=39.7C,PCB=028.0C, 0.88B,000.0PSIG, 20.3%,6,
FCS=47.3V,00.48A,022.7W,000.31Wh,LD=48.5V, 31.0C,32.8C,32.8C,31.7C,TST=39.7C,PCB=026.7C, 0.93B,000.0PSIG, 20.3%,6,
FCS=46.8V,00.51A,023.8W,000.32Wh,LD=46.5V, 31.0C,32.8C,32.9C,31.7C,TST=39.7C,PCB=027.7C, 0.87B,000.0PSIG, 20.3%,6,
FCS=49.9V,00.75A,037.5W,000n32Wh,LD=49.3V, 31.5C,33.4C,33.3C,32.1C,TST=39.7C,PCB=031.2C, 0.90B,000.0PSIG, 20.5%,6,
FCS=49.3V,00.56A,027.5W,000.33Wh,LD=49.1V, 31.4C,33.8C,33.3C,32.0C,TST=39.7C,PCB=029.3C, 0.96B,000.0PSIG, 20.4%,6,
FCS=46.6V,00.83A,038.7W,000.34Wh,LD=46.2V, 31.4C,34.0C,33.4C,32.0C,TST=39.8C,PCB=027.7C, 0.93B,000.0PSIG, 20.6%,6,
FCS=43.1V,08.46A,364.4W,000.39Wh,LD=42.8V, 31.5C,33.3C,33.1C,32.0C,TST=41.4C,PCB=027.7C, 0.87B,000.0PSIG, 26.3%,6,
FCS=44.0V,08.35A,367.2W,000.50Wh,LD=43.3V, 31.9C,34.0C,33.7C,32.4C,TST=41.4C,PCB=030.0C, 0.94B,000.0PSIG, 26.2%,6,
FCS=43.0V,08.07A,347.4W,000.60Wh,LD=43.3V, 31.7C,33.6C,33.5C,32.2C,TST=41.4C,PCB=028.1C, 0.87B,000.0PSIG, 26.0%,6,
FCS=41.9V,07.98A,334.0W,000.69Wh,LD<41.5V, 31.5C,33.2C,33.2C,32.1C,TST=41.3C,PCB=026.7C, 0.89B,000.0PSIG, 25.9%,6,
FCS=33.5V,25.66A,858.4W,000.84Wh,LD=33.5V, 31.7C,33.7C,33.6C,32.2C,TST=46.0C,PCB=028.0C, 0.76B,000.0PSIG, 38.0%,6,
FCS=34.4V,31.68A,1089.9W,001.13Wh,LD=35.2V, 32.1C,34.0C,34.1C,32.7C,TST=46.5C,PCB=027.1C, 0.80B,000.0PSIG, 43.8%,6,
FCS=35.6V,31.61A,1126.7W,001.43Wh,LD=35.5V, 33.0C,35.6C,35.2C,33.6C,TST=46.4C,PCB=029.5C, 0.78B,000.0PSIG, 43.5%,6,
FCS=35.0V,35.13A,1228.1W,001.76Wh,LD=35.5V, 34.0C,37.1C,36.1C,34.4C,TST=47.3C,PCB=028.0C, 0.86B,000.0PSIG, 46.4%,6,
FCS=35.4V,34.37A,1216.5W,002.10Wh,LD=35.2V, 34.6C,37.4C,37.0C,35.1C,TST=47.1C,PCB=028.3C, 0.81B,000.0PSIG, 45.7%,6,
FCS=36.6V,32.59A,1194.0W,002.44Wh,LD=36.3V, 35.2C,38.1C,37.6C,35.6C,TST=46.7C,PCB=028.5C, 0.83B,000.0PSIG, 44.5%,6,
FCS=35.7V,30.23A,1078.4W,002.75Wh,LD=35.5V, 35.8C,38.8C,38.2C,36.0C,TST=46.2C,PCB=028.3C, 0.83B,000.0PSIG, 42.6%,6,
FCS=35.2V,32.11A,1131.4W,003.06Wh,LD=.1V, 36.2C,39.4C,38.7C,36.6C,TST=46.6C,PCB9027.8C, 0.82B,000.0PSIG, 44.0%,6,
FCS=35.7V,33.29A,1188.2W,003.38Wh,LD=35.3V, 37.0C,4.rJ&99¾6¾ž37.4C,TST=46.8C,PCB=030.7C, 0.75B,000.0PSIG, 44.8%,6,

FCS=35.0V-â,+_ª,—È60.1W,003.70Wh,LD=35.1V, 36.9C,40.2C,39.7C,37.4C,TST=46.8C<PCB=029.3C, 0.89B,000.0PSIG, 44.8%,6,
FCS=34.8V,33.47A,1165.1W,004.02Wh,LD=34.8V, 37.3C,41.1C,40.2C,37.9C,TST=46.9C,PCB=029.7C, 0.7900.0PSIG, 45.1%,6,
FCS=35.2V,33.45A,1178.1W,004.35Wh,LD=35.0V, 37.5C,41.9C,40.5C,38.2C,TST=46.9C,PCB=030.1C, 0.78B,000.0PSIG, 45.0%,6,
FCS=35.8V,33.35A,1193.7W,004.68Wh,LD=36.4V, 38.5C,42.8C,41.7C,39.3C,TST=46.8C,PCB=030.1C, 0.84B,000.0PSIG, 44.8%,6,
FCS=36.6V,35.43A,1296.3W,005.02Wh,LD=36.4V, 38.6C,43.2C,41.8C,39.4C,TST=47.4C,PCB=029.1C, 0.85B,000.0PSIG, 46.7%,6,
FCS=36.1V,32.53A,1173.3W(005.76Wh,LD=36.7V, 39.0C,43.8C,42.5C,4 .1C,TST=46.7C,PCB=029.7C, 0.83B,000.0SIG, 44.4%,6,
-FCS=36.9V,31.79A,1173.2W,005.69Wh,LD=36.5V, 38.8C,43.5C,42.4C,40.1C,TST=46.5C,PCB=031.1C, 0.84B,000.0PSIG, 43.9%,6,
FCS=36.6V,30.88A,1131.3,06.01Wh,LD=36.0V, 39.1C,44.0C,42.6C,40.3C,TST946.3C,PCB=029.7C, 0.80B,000.0PSIG, 43.1%,,
FCS=37.6V,29.56A,1112.8W,006.32Wh,LD=37.0V, 39.TST=46.0C,PCB=030.8C, 0.86,
FCS=37.0,30.24A,1120.3W,006.62Wh,LD=36.2V, 39.8C,45.3C,43.5C,41.2C,TST=4B,000.0PSIG, 42.6%,6,
FCS=36.7,31.53A,1156.0W,006.94Wh,LD=36.4V, 39.7C-45.7C,43.8C,49*4C,TSD=0’.,000.0PSIG, 41-u%,6,
FCS=35.1V,Wh,LD=34.9V, 39.7C,46.1C,43.7C,41.3C,TST=46.9C,PCB=029.5C, 0.80B,000.0PSIG, 45.2%,6,
FCS=35.0V,34.66A,1214.3W,007.60Wh,LD=35.3V, 39.7C,46.3C,43.8C,41.5C,TST=47.1C,PCB=030.5C, 0.79B,000.0PSIG, 45.9%,6,
FCS=36.3V,33.87A,1229.4W,007.94Wh,LD=35.9V, 40.3C,46.5C,44.6C,42.2C,TST=46.9C,PCB=031.4C, 0.85B,000.0PSIG, 45.3%,6,
FCS=37.3V,34.41A,1282.7W,008.29Wh,LD=37.1V, 40.4C,46.4C,44.6C,42.4C,TST=47.2C,PCB=031.9C, 0.88B,000.0PSIG, 46.0%,6,
FCS=37.5V,30.64A,1148.8W,008.63Wh,LD=37.0V, 40.2C,46.1C,44.4C,42.2C,T, 0.86B,000.0PSIG, 43.0%,6,
FCS=36.9V,31.49A,1161.8W,008.94Wh,LD=36.5V, 40.5C,46.4C,44.7C,42.4C,TST6.4C,PCB=029.9C, 0.82B,000.0PSIG, 69.9%,6,FCS=35.9V,31.85A,1142.2W,009.27Wh,LD=36.7V, 40.5C,46.3C,44.5C,42.3C,TST=4.5C,PCB=030.2C, 0.w
00.0PSIG, 43.8%,6,
FCS=34/9V,31.94A,1145.5×,009.59Wh,LD=35.7V, 40.3C,466m,¾”Q™00-2}ÌT
Q6C,B=00.0PSIG, 43.9%,6,
FCS=35.3V,32.26A,1139.5W,009.90WhŽLD=35.7V, 40.3C,46.7C44.2C,42.1C,TST=16_CCB=030.3C, 0.66B,010PSIG, 44.1%,6,
FCS=35.4V,33.75A,1194.2W,010.23Wh,LD=35.0V, 40.5C,47.0C,44.PCB=030.3C, 0.84B,000/0PSIG, 45.3%,6,

FCS=34.4V,35.84A1231.0W,010.57Wh,LD=34.4V, 40.5C,46.9C,44.6C,45C,TSP=47.4C,PCB=030.6C, 0.81B,000.0PSIG, 46.6%,6,
FCS=35.2V,35.68A,1257.7W,010.91Wh,LD=35.2V, 40.4C,46.6C,44.4C,42.¾W^Kh\¦‡Lë¹æa7C4C,TST=476†C¤PCB=032.4C, 0.81B,000.0PSIG, 46.8%,6,
FCS=?]2Vp3#683,11929W,011.25Wh,LD=35.1V, 40.4C(46.6C,44.6C,42.5C,TST=46.9C,PCB=030.5C, 0.81B,000.0PSIG, 45.2%,6,
FCS=36.1V,35.13A,1269.0W,011.60Wh,LD=35.8V, 41C,47ê±C,64¿+A¬P.7Il´S.0PSIG, 46.6%,6,
FCS=36.5V,34.61A,1262.0W,011.95Wh,LD=36.4V, 40.5C,4.=C,45.0C,43.2C,TST=47.1C,PCB=033.2C, 0.85B,000.0PSIG, 45.9%,6,
FCS=35.6V,34.29A,1226.;ôq'2QWh,LD=35.5V, 40.5C,47.2C,45.1C,43.3C,TST=·,qCCB=031.6C, 0.79B,000.0PSIG, 45.7%,6,
FCS=34.9V,35.48A,1237.4W,012.63Wh,LD=34.8V, 40.3C,47.3C,44.7C,42.9C,TST=47.3C,PCB=030.8C, 0.78B,000.0PSIG, 46.5%,6,
5.3V,36.30A,1280.8W,12.98Wh,LD=s5&4V, 40.7C,48.1C
ý²o³q 0C"¹C<TST=47.5C,PCB=033.3C, 0.81B,000.0PSIG, 47.2%,6,
FCS=34.5V,35.67A,1232.3W,013.3h,LD=35.3V, 40.1C,47.1C,44.8C,43.3C,TST=47.4C,PCB=031.7C, 0.82B,000.0PSIG, 46.7%,6,
S=13.69Wh,LD=35.0V, 40.6C,47.7C,45.5C,43.9C,TST=47.5C,PCB=034.3C, 0.82B,000.0PSIG, 47.0%,6,
FCS=36.1V,35.48A,1281.7W,014.04Wh,LD=36.0V, 40.7C,48.3C,45.8C,44.3C,TST=47.3C,PCB=034.1C, 0.84B,000.0PSIG, 70.9%,6,
FCS=35.2—|+Ï<0><0>,35h1227.2W,014.75Wh,LD=3.1V, 40.2C,47.6C,45.7C44.5C,TST=47+uC,PCB=032.5C, 0.80B,000.0PSIG, .0%,6,
FCS=35.3V,36.12A,1276.1W,015.09Wh,LD=35.0V, 39.5C,47.2C,45.0C,43.7C,TST=47.5C,PCB=031.4C, 083B,000.0PSIG, 47.1%,6,
FCS=35.3V,36.68A,1294.3W,015.46Wh,LD=36.1V, 40.0C,48.2C,45.7C,44.6C,TST=47.6C,PCB=033.5C, 0.81B,000.0PSIG, 47.5%,6,
FCS=35.4V,36.58A,1296.4W,015.83Wh,LD=36.1V, 40.0C,48.0C,45.7C,44.5C,TST=47.6C,PCB=033.3C, 0.83B,000.0PSIG, 47.4%,6,
FCS=36.0V,36.22A,1305.2W,016.19Wh,LD=35.8V, 39.9C,48.1C,45.8C,44.8C,TST=47.5C,PCB=034.2C, 0.87B,000.0PSIG, 47.2%,6,
FCS=36.4V,34.21A,1243.8W,016.54Wh,LD=36.2V, 39.5C,47.7C,5.6C,44.5C,TST=47.1C,PCB=032.9C, 0.82B,000.0PSIG, 45.7%,6,
FCS=37.4V,30.11A,1124.8W,016.88Wh,LD=37.2V, 39.2C,46.9C,45.2C,44.4C,TST=46.2C,PCB=030.9C, 0.86B,000.0PSIG, 65.9%,6,
FCS=35.9V,30.12A,1080.4W,017.18Wh,LD=35.8V, 38.7C,46.5C,44.7C,44.0C,TST=46.1C,PCB=031.7C, 0.83B,000.0PSIG, 93.9%,6,
FCS=35.6V,32.25A,1147.1W,017.49Wh,LD=35.3V, 38.3C,46.0C,44.4C,43.7C,TST=46.6C,PCB=033.9C, 0.84B,000.,`Ñ¦¤1%,6,

FCS=35.1V,34.08A,1197.3W,017.81Wh,LD=35.5V, 38.6C,46.3C,44.8C,44.4C,TST=47.0C,PCB=034.3C, 0.73B,000.0PSIG, 45.5%,6,
0,46.8C,44.7C,44.2C,T=46.83$FCS=35.5V,35.52A,1261.7W,018.50Wh,LD=35.3V,
38.2C,46.8C,44.6C,46.1C,TWT=47.3C,PCB=033.4CÈ, 0.Ûg]ËYGD79B,000.0PSIG, 46.5%,6,
CS=37.1V,35.17A,1305.0W,018.86Wh,LD=37.1V, 38.6C,47.0C,45.1C,44.8C,TST=47.3C,PCB=035.1C, 0.85B,000.0PSIG, 46.5%,6,
FCS=36.7V,33.03A,1211.2W,019.21Wh,LD=36.4V, 38.5C,47.0C,45.1C,44.7C,TST=46.8C,PCB=033.0C, 0.81B,000.0PSIG, 44.8%,6,
FCS=35.7444.3C,TST=46.9C,PCB=032.6C, 0.79B,000.0PSIG, 44.9%,6,
FCS=35.6V,35.3A,1257.7W,019.88Wh,LD=35.5V, 38.7C,46.9C,45.4C,45.1C,TST=47.3C,PCB=034.5C, 0.78B,000.0PSIG, 46.3%,6,
FCS=35.9V,35.99A,1291.4W,020.24Wh,LD=35.3V, 38.6C,46.7C,45.2C,45.0C,TST=47.5C,PCB=033.3C, 0.82B,000n¤tSIÃö®47.0%,6,
FCS=35.8V,35.49A,1270.5W,020.59Wh,LD=36.4V, 38.7C,47.2C,45.6C,45.2C,TST=47.3C,PCB=034.2C, 0.84B,000.0PSIG, 46.5%,6,
FCS=36.7V,33.94A,1244.8W,020.94Wh,LD=36.6V, 38.5C,46.9C,45.4C,45.1C,TST=47.0C,PCB=033.7C, 0.85B,000.0PSIG, 45.5%FCS=36.5V,32.10A,1171.3W,021.28Wh,LD=36.4V, 38.6C,47.6C,45.5C,45.4C,ST=46.6C,PCB=033.7C, 0.8B,000.0PSIG, 44.0%,6,FCS=36.3V,33.04A,1200.5W,021.58Wh,LD=35.9V, 38.5C,48.0C,45.4C,45.4C,TST=46.8C,PCB=035.0C, 0.75B,000.0PSIG, 58.9%,6,
V,14.56A,1264.4W,021.2Wh,LD=36.5V, 39.7C,46.9C,44.4C,44.5C,TST=47.1C,PCB=034.1C, 0.82B72².0PSIG, 46.0%,6,
FCS=36.5V,32.99A,1203.1W,022.27Wh,LD=36.7V, 38.0C,47.1C
FCS=36.3V,33.19A,1204.7W,022.60Wh,LD=36.2V, 37.6C,46.7C,44.2C,44.5C,TST=46.8C,PCB=033.7C, 0.77B,000.0PSIG, 44.9%,6,
FCS=37.2V,32.18A,1197.6W,022.94Wh,LD=36.7V, 37.9C,47.0C,44.7C,45.2C,TST=46.6C,PCB=033.6C, 0.86B,000.0PSIG, 44.2%,6,
FCS=39.3V,29.22A,1147.2W,023.26Wh,LD=38.8V, 37.3C,46.2C,44.1C,44.6C,TST=46.0C,PCB=034.6C, 0.85B,000.0PSIG, 42.2%,6,
FCS=45.3V,20.08A,910.2W,023.55Wh,LD=44.6V, 37.1C,46.1C,43.7C,44.3C,TST=46.0C,PCB=033.9C, 0.83B,000.0PSIG, 41.0%,6,
FCS=43.3V,08.87A,383.7W,023.71Wh,LD=44.7V, 36.7C,46.2C,43.3C,43.8C,TST=41.5C,PCB=032.3C, 0.92B,000.0PSIG, 100.0%,6,
FCS=43.9V,09.40A,412.3W,023.83Wh,LD=42.5V,$35.9C,45.5C,42.4C,42.7C,TST=41.6C,PCB=033.2C, 0.88B,000.0PSIG, 100.0%,6,
FCS=43.5V,09.40A,408.4W,023.94Wh,LD=43.8V, 34.8C,44.,40.9C,41.7C,TST=41.6C,PCB=033.1C, 0.87B,000.0PSIG, 100.0%,6,

FCS=44.0V,08.66A,381.3W,024.04Wh,LD=43.6V, 33.3C,41.7C,38.9C,40.1C,TST=41.5C,PCB=034.7C, 0.84B,000.0PSIG, 67.6%,6,
FCS=48.2V,02.67A,128.9W,024.13Wh,LD=46.9V, 32.5C,40.8C,37.9C,39.3C,TST=40.2C,PCB=033.3C, 0.96B,000.0PSIG, 67.1%,6,
FCS=49.6V,01.09A,054.1W,024.14Wh,LD=49.1V, 31.9C,39.6C,37.2C,38.5C,TST=39.8C,PCB=035.5C, 0.99B,000.0PSIG, 20.8%,6,
FCS=49.2V,00.63A,031.0W,024.16Wh,LD=48.9V, 30.9C,38.1C,36,7.4%,6,
FCS=47.8V,00.57A,027.5W,024.16Wh,LD=48.6V, 30.2C,36.9C,35.0C,36.5C,TST7C,PCB=031.4C, 03B,000.0PSIG, 20.4%,6,
FCS=48.3V,00.53A,025.5W,024.17Wh,LD=48.4V, 29.9C,37.0C,34.8C,36.3C,TST=39.7C,PCB=032.8C, 0.95B,000.0PSIG, 20.4%,6,
FCS=49.5V,00.63A,031.2W,024.18Wh,LD=48.8V, 29.8C,36.6C,34.5C,36.1C,TST=39.7C,PCB=034.7C, 0.93B,000.0PSIG, 20.4%,6,
FCS=48.5V,00.71A,034.5W,024.19Wh,LD=49.0V, 29.5C,36.6C,34.2C,35.7C,TST=39.7C,PCB=032.6C, 1.00B,000.0PSIG, 20.5%,6,
FCS=48.4V,00.53A,025.8W,024.20Wh,LD=48.2V, 29.0C,35.6C,33.6C,35.1C,TST=39.7C,PCB=033.9C, 0.96B,000.0PSIG, 20.4%,&,
FCS=48.8V,00.71A,034.5W,024.20Wh,LD=48.8V, 29.0C,35.2C,33.6C,35.2C,TST=39.7C,PCB=03.2C, 0.97B,000.0PSIG, 20.5%,6,
FCS=48.6V,00.69A,033.6W,024.21Wh,LD=49.8V, 28.8C,34.8C,33.3C,34.9C,TST=39.7C,PCB=032.8C, 091B,000.0PSIG, 20.5%,6,
FCS=49.3V,00.66A,032.7W,024.22Wh,LD=49.0V, 28.7C,34.2C,33.0C,34.6C,TST=39.7C,PCB=031.7C, 0.96B,000.0PSIG, 20.5%,6,
FCS=48.8V,00.57A,027.7W,024.23Wh,LD=48.3V, 28.4C,34.1C,32.7C,34.2C,TST=39.7C,PCB=031.5C, 0.97B,000.0PSIG, 20.4%,6,
FCS=49.0V,00.72A,035.5W,024.24Wh,LD=48.7V, 28.7C,34.6C,33.0C,34.6C,TST=39.7C,PCB=032.2C, 0.99B,000.0PSIG, 20.5%,6,
FCS=49.0V,00.62A,030.5W,024.25Wh,LD=48.7V, 28.5C,34.4C,32.7C,34.3C,TST=39.7C,PCB=032.6C, 0.98B,000.0PSIG, 20.4%,6,
FCS=49.2V,00.62A,030.3W,024.26Wh,LD=48.9V, 28.5C,34.4C,32.6C,34.2C,TST=39.7C,PCB=033.6C, 0.88B,000.0PSIG, 20.4%,6,
FCS=48.3V,00.69A,033.4W,024.27Wh,LD=49.1V, 28.6C,34.5C,32.7C,34.3C,TST=39.7C,PCB=032.4C, 0.98B,000.0PSIG, 20.5%,6,
FCS=48.6V,00.56A,027.3W,024.28Wh,LD=48.0V, 28.2C,33.7C,32.1C,33.7C,TST=39.7C,PCB=032.3C, 0.91B,000.0PSIG, 20.4%,6,
FCS=48.0V,00.57A,027.3W,024.28Wh,LD=47.7V, 28.0C,33.4C,32.0C,33.5C,TST=39.7C,PCB=030.5C, 0.95B,000.0PSIG, 20.4%,6,
FCS=48.4V,00.55A,026.6W,024.29Wh,LD=48.1V, 28.1C,33.3C,32.1C,33.6C,TST=39.7C,PCB=033.1C, 0.97B,000.0PSIG, 20.4%,6,
FCS=42.9V,00.44A,018.9W,024.30Wh,LD=43.0V, 27.8C,32.8C,31.8C,33.4C,TST=39.7C,PCB=030.5C, 0.79B,000.0PSIG, 20.3%,6,
FCS=49.1V,00.72A,035.6W,024.31Wh,LD=49.7V, 28.2C,33.5C,32.2C,33.7C,TST=39.7C,PCB=032.5C, 0.96B,000.0PSIG, 20.5%,6,
FCS=49.1V,00.52A,025.6W,024.31Wh,LD=49.0V, 28.3C,33.5C,32.3C,33.7C,TST=39.7C,PCB=032.9C, 0.98B,000.0PSIG, 20.3%,6,
FCS=49.4V,00.59A,029.4W,024.32Wh,LD=49.1V, 28.5C,34.0C,32.4C,33.7C,TST=39.7C,PCB=033.6C, 0.97B,000.0PSIG, 20.4%,6,
FCS=48.1V,00.44A,021.2W,024.33Wh,LD=48.2V, 28.1C,33.8C,32.1C,33.3C,TST=39.7C,PCB=030.2C, 0.95B,000.0PSIG, 20.3%,6,
FCS=48.9V,00.61A,029.8W,024.34Wh,LD=48.3V, 28.3C,33.3C,32.2C,33.5C,TST=39.7C,PCB=032.9C, 1.00B,000.0PSIG, ,6,
FCS=48.2V,00.76A,036.5W,024.35Wh,LD=49.3V, 28.5C,33.7C,32.3C,33.6C,TST=39.7C,PCB=031.4C, 0.91B,000.0PSIG, 20.5%,6,
FCS=48.7V,00.66A,032.3W,024.36Wh,LD=48.6V, 28.5C,33.5C,32.4C,33.6C,TST=39.7C,PCB=030.8C, 0.96B,000.0PSIG, 20.5%,6,
FCS547.<V,00.5A,828.4W,024&36Và,LD947.Ö, :8n0,31.7C,33.1C,TST=39.7C,PCB=030.0C, 0.92B,000.0PSIG, 20.4%,6,
FCS=48.4V,00.59A,028.4W,024.37Wh,LD=48.3V, 28.2C,32.8C,32.0C,33.3C,TST=39.7C,PCB=032.4C, 0.94B,000.0PSIG, 20.4%,6,
FCS=48.7V,00.67A,032.7W,024.38Wh,LD=48.4V, 28.3C,33.1C,31.9C,33.1C,TST=39.7C,PCB=030.3C, 0.94B,000.0PSIG, 20.5%,6,

FCS=48.9V,00.56A,027.2W,024.39Wh,LD=48.4V, 28.3C,33.3C,32.0C,33.2C,TST=39.7C,PCB=029.8C, 0.95B,000.0PSIG, 20.4%,6,
FCS=49.0V,00.72A,035.5W,024.40Wh,LD=49.6V, 28.7C,34.0C,32.4C,33.5C,TST=39.7C,PCB=032.1C, 0.98B,000.0PSIG, 20.5%,6,
FCS=48.7V,00.58A,028.5W,024.41Wh,LD=48.7V, 28.5C,33.3C,32.1C,33.3C,TST=39.7C,PCB=032.0C, 0.98B,000.0PSIG, 20.4%,6,
FCS=48.0V,00.48A,023.2W,024.41Wh,LD=48.4V, 28.3C,33.0C,31.9C,33.1C,TST=39.7C,PCB=031.0C, 0.92B,000.0PSIG, 20.3%,6,
FCS=49.3V,00.72A,035.5W,024.42Wh,LD=49.1V, 28.8C,33.4C,32.3C,33.4C,TST=39.7C,PCB=032.8C, 0.87B,000.0PSIG, 20.5%,6,
FCS=48.4V,00.56A,027.3W,024.43Wh,LD=48.6V, 28.4C,32.9C,32.0C,33.0C,TST=39.7C,PCB=031.0C, 0.94B,000.0PSIG, 20.4%,6,
FCS=48.8V,00.79A,0LD=48.1V, 28.7C,33.2C,32.4C,33.4C,TST=39.8C,PCB=031.4C, 0.93B,000.0PSIG, 20.6%,6,
FCS=49.1V,00.81A,039.8W,024.45Wh,LD=48.8V, 28.7C,33.1C,32.3C,33.4C,TST=39.8C,PCB=033.1C, 0.93B,000.0PSIG, 20.6%,6,
FCS=48.1V,00.59A,028.2W,024.46Wh,LD=48.0V, 28.3C,32.8C,31.8C,32.8C,TST=39.7C,PCB=031.9C, 0.95B,000.0PSIG, 20.4%,6,
FCS=01.5V,00.48A,000.7W,024.47Wh,LD=40.1V, 28.3C,33.2C,31.8C,32.7C,TST=39.7C,PCB=032.9C, 0.83B,000.0PSIG, 20.3%,6,
FCS=49.4V,00.74A,036.4W,024.47Wh,LD=50.2V, 28.,TST=39.7C,PCB=032.1C, 0.93B,000.0PSIG, 20.5%,6,
FCS=48.6V,00.62A,030.1W,024.48Wh,LD=49.2V, 28.8C,33.3C,32.3C,33.2C,TST=39.7C,PCB=030.7C, 0.97B,000.0PSIG, 20.4%,6,
FCS=48.8V,00.78A,038.0W,024.49Wh,LD=49.5V, 29.0C,33.4C,32.4C,33.4C,TST=39.7C,PCB=031.2C, 0.99B,000.0PSIG, 20.5%,6,
FCS=48.00.75A,036.8W,024.50Wh,LD=48.6V, 29.0C,33.0C,32.3C,33.4C,TST=39.7C,PCB=031.2C, 0.99B,000.0PSIG, 20.5%,6,
FCS=47.7V,00.50A,024.0W,024.51Wh,LD=47.9V, 28.5C,32.6C,31.9C,32.7C,TST=39.7C,PCB=029.9C, 0.87B,000.0PSIG, 20.3%,6,
FCS=48.0V,00.54A,026.1W,024.52Wh,LD=48.0V, 28.7C,32.6C,32.0C,32.8C,TST=39.7C,PCB=029.6C, 0.95B,000.0PSIG, 20.4%,6,
FCS=48.8V,00.73A,035.7W,024.53Wh,LD=48.7V, 29.0C,33.0C,32.2C,33.1C,TST=39.7C,PCB=032.0C, 0.98B,000.0PSIG, 20.5%,6,
FCS=48.0V,00.60A,028.7W,024.54Wh,LD=47.9V, 28.5C,32.9C,31.8C,32.6C,TST=39.7C,PCB=030.3C, 0.94B,000.0PSIG, 20.4%,6,
FCS=48.7V,00.59A,028.9W,024.54Wh,LD=47.9V, 29.0C,33.4C,32.1C,32.9C,TST=39.7C,PCB=030.5C, 0.97B,000.0PSIG, 20.4%,6,
FCS=49.2V,00.79A,039.0W,024.55Wh,LD=49.0V, 28.8C,32.82.1C,32.8C,TST=39.8C,PCB=032.4C, 0.90B,000.0PSIG, 20.5%,6,
FCS=49.2V,00.65A,031.8W,024.56Wh,LD=49.7V, 29.1C,33.0h,LD=49.7V, 29.C,32.3C,33.0C,TST=39.7C,PCB=030.9C, 0.98B,000.0PSIG, 20.4%,6,
FCS=48.4V,00.59A,028.7W,024.58Wh,LD=48.0V, 28.7C,32.5C,32.0C,32.7C,TST=39.7C,PCB=030.0C, 0.93B,000.0PSIG, 20.4%,6,
FCS=48.4V,00.62A,030.1W,024.59Wh,LD=48.3V, 28.8C,32.7C,32.2C,32.9C,TST=39.7C,PCB=029.0C, 0.97B,000.0PSIG, 20.4%,6,
FCS=48.3V,00.61A,029.4W,024.60Wh,LD=48.9V, 29.0C,32.8C,32.2C,32.9C,TST=39.7C,PCB=031.0C, 0.83B,000.0PSIG, 20.4%,6,
FCS=48.5V,00.75A,036.2W,024.61Wh,LD=48.3V, 29.3C,33.3C,32.4C,33.0C,TST=39.7C,PCB=030.2C, 0.96B,000.0PSIG, 20.5%,6,
00.78A,038.6W,024.62Wh,LD=48.6V, 29.1C,33.2C,32.3C,32.9C,TST=39.8C,PCB=031.5C, 0.96B,000.0PSIG, 20.5%,6,
FCS=48.1V,00.73A,034.9W,024.63Wh,LD=48.1V, 29.0C,32.9C,32.2C,32.8C,TST=39.7C,PCB=030.5C, 0.94B,000.0PSIG, 20.5%,6,
DB3:SetNormalShutdown_cFCS ...
FCS=48.6V,00.80A,038.9W,024.64Wh,LD=47.9V, 29.2C,33.2C,32.3C,32.9C,TST=39.8C,PCB=031.1C, 0.78B,000.0PSIG, 20.6%,8,
FCS=50.7V,00.39A,019.8W,024.65Wh,LD=34.9V, 28.8C,32.3C,31.9C,32.6C,TST=39.7C,PCB=032.2C, 1.06B,000.0PSIG, 20.3%,8,

FCS=49.9V,00.06A,003.1W,024.65Wh,LD=34.8V, 29.2C,32.8C,32.4C,32.9C,TST=39.6C,PCB=030.5C, 1.10B,000.0PSIG, 20.0%,8,
FCS=47.6V,00.05A,002.4W,024.65Wh,LD=34.4V, 29.1C,32.6C,32.3C,32.7C,TST=39.6C,PCB=029.0C, 1.05B,000.0PSIG, 20.0%,8,
FCS=46.3V,00.06A,002.7W,024.65Wh,LD=35.2V, 30.0C,33.2C,33.1C,33.5C,TST=39.6C,PCB=032.6C, 1.11B,000.0PSIG, 20.0%,8,
FCS=01.2V,00.04A,000.0W,024.65Wh,LD=34.7V, 30.2C,33.9C,33.4C,33.6C,TST=39.6C,PCB=029.3C, 1.00B,000.0PSIG, 20.0%,8,
FCS=06.4V,00.05A,000.3W,024.65Wh,LD=35.0V, 30.7C,34.7C,33.9C,34.0C,TST=39.6C,PCB=030.8C, 1.02B,000.0PSIG, 20.0%,8,
FCS=05.5V,00.06A,000.4W,024.65Wh,LD=35.1V, 30.8C,35.0C,34.0C,34.0C,TST=39.6C,PCB=032.1C, 0.98B,000.0PSIG, 20.0%,8,
FCS=06.3V,00.08A,000.5W,024.65Wh,LD=35.4V, 30.8C,34.7C,34.0C,34.1C,TST=39.6C,PCB=030.2C, 1.00B,000.0PSIG, 20.0%,8,
FCS=06.7V,00.10A,000.7W,024.65Wh,LD=35.6V, 31.1C,34.8C,34.2C,34.3C,TST=39.6C,PCB=030.5C, 0.94B,000.0PSIG, 20.0%,8,
FCS=06.7V,00.04A,000.3W,024.65Wh,LD=34.9V, 30.6C,34.2C,33.6C,33.7C,TST=39.6C,PCB=029.5C, 0.89B,000.0PSIG, 20.0%,8,

---

Date: 11/5/2021 - 1:56:52 PM
End log file

THIS PAGE INTENTIONALLY LEFT BLANK

APPENDIX I. SCALING LAW RAW DATA

N (rpm)	Open Flow Force (N)	Open Flow Torque (Nm)
0	0	0.0000
425	0.93	-0.0352
575	1.69	-0.0644
725	2.69	-0.1024
875	3.92	-0.1491
1025	5.38	-0.2046
1175	7.07	-0.2689
1325	9.45	-0.3533
1475	11.71	-0.4493
1625	14.21	-0.5568
1800	17.44	-0.6758

N (rpm)	Measured Force (N)	Measured Torque (Nm)
0	0	0
425	1.33	-0.2447
725	3.27	-0.3189
1025	6.413	-0.4123
1325	10.82	-0.5402
1625	16.43	-0.7078
1800	21.12	-0.8176

N (rpm)	Pipe Flow Force (N)	Pipe Flow Torque (Nm)
120	0.32568	-0.01487
450	1.4171	-0.04756
1100	7.8696	-0.18916
1800	22.614	-0.57088

THIS PAGE INTENTIONALLY LEFT BLANK

APPENDIX J. VELOCITY AND PRESSURE RAW DATA

Pipe Flow		
Radius	Pressure (Pa)	Velocity (m/s)
0.035	38.98	4.092
0.07	42.999	5.641
0.0875	61.198	17.245
0.105	66.07	-6.78
0.1225	59.468	-4.359
0.14	54.849	-4.58
0.175	60.464	-5.356
0.21	62.633	-5.267
0.245	62.96	-4.507
0.28	61.204	-3.511
0.315	55.971	-68.435
0.355	27.928	3.992

Open Flow				
	1325 RPM		1800 RPM	
Radius	Pressure (Pa)	Velocity (m/s)	Pressure (Pa)	Velocity (m/s)
0.035	-0.2215	-0.2433	-0.4088	-0.3305
0.07	3.0966	-2.2122	5.7148	-3.0053
0.105	15.4385	-4.3221	28.4917	-5.8715
0.14	21.9620	-4.6957	40.5308	-6.3791
0.175	24.2851	-4.9849	44.8181	-6.7719
0.21	24.9860	-5.0853	46.1116	-6.9083
0.245	24.1880	-4.8068	44.6389	-6.5300
0.28	22.4389	-4.2549	41.4109	-5.7802
0.315	19.7815	-3.5644	36.5067	-4.8422
0.3325	16.7984	-3.0106	31.0014	-4.0899
0.35	0.1845	-0.7874	0.3404	-1.0697

THIS PAGE INTENTIONALLY LEFT BLANK

APPENDIX K. COEFFICIENT OF LIFT RAW DATA

Spanwise Lift Coefficient		
Radius (m)	Pipe Flow	Open Flow
0	0	0
0.03556	4.506	0.02524
0.07112	2.781	0.82719
0.10724	1.453	0.79165
0.14336	0.8163	0.66543
0.17948	0.7429	0.612967
0.21560	0.6905	0.58712
0.25172	0.6896	0.56594
0.28784	0.7111	0.565226
0.32396	0.7370	0.57585
0.36008	0	0

THIS PAGE INTENTIONALLY LEFT BLANK

LIST OF REFERENCES

[1] A.O. Kohn, "Military Vertical Takeoff and Landing (VTOL) Propulsion Systems Design," *Proceedings of the ASME 1972 International Gas Turbine and Fluids Engineering Conference and Products Show.* San Francisco, CA, USA, March 26–30, 1972.

[2] Krossblade Aerospace, "Disc loading and hover efficiency." Accessed September 17, 2021. [Online]. Available: https://www.krossblade.com/disc-loading-and-hover-efficiency

[3] B. R. Hein and I. Chopra, "Hover performance of a Micro Air Vehicle: Rotors at low Reynolds number," *Journal of the American Helicopter Society*, vol. 52, no. 3, pp. 254–262, 2007.

[4] A. Roderick, "Transformer losses and efficiency - technical articles," *EEPower*, June 16, 2021. [Online]. Available: https://eepower.com/technical-articles/transformer-losses-and-efficiency/.

[5] A. G., J. S., O. López, L. Suárez C, and J. A. Escobar, "Numerical and Experimental Estimation of the Efficiency of a Quadcopter Rotor Operating at Hover," *Energies*, vol. 12, no. 2, p. 261, Jan. 2019, doi: 10.3390/en12020261.

[6] G. V. Hobson, A. J. Gannon, C. T. Delagrange, C. S. Clay and A. M. Jones, "Cross Flow Fan Development for Propulsion of a Vertical Take-Off and Landing Vehicle," in 15th International Symposium on Transport Phenomena and Dynamics of Rotating Machinery, ISROMAC-15, Honolulu, HI, USA, February 24–28 2014.

[7] ANSYS, "Applications," Accessed November 13, 2021. [Online]. Available: https://www.ansys.com/applications.

[8] Zeal CAD Services, "What Is the Scope of Finite Element Analysis for Future," Accessed November 13, 2021. [Online]. Available: https://www.zcads.com.au/scope-finite-element-analysis-future/.

[9] T. Yomchinda, "Simplified Propeller Model for the Study of UAV Aerodynamics using CFD method," *2018 5th Asian Conference on Defense Technology (ACDT)*, 2018, pp. 69–74, doi: 10.1109/ACDT.2018.8592940.

[10] H. Kutty and P. Rajendran, "3D CFD Simulation and Experimental Validation of Small APC Slow Flyer Propeller Blade," *Aerospace*, vol. 4, no. 1, p. 10–, 2017, doi: 10.3390/aerospace4010010.

[11] J. N. Sorensen, “Aerodynamic Analysis of Wind Turbines,” *Comprehensive Renewable Energy*, 2012. Accessed January 3, 2022. [Online]. Available: https://www.sciencedirect.com/science/article/pii/B9780080878720002092.

[12] NASA, “Propeller Thrust,” Accessed January 3, 2022. [Online]. Available: https://www.grc.nasa.gov/WWW/K-12/airplane/propth.html.

[13] G. R. Hough, D. E. Ordway, and Therm Advanced Research Inc, Ithaca, NY, USA, “THE GENERALIZED ACTUATOR DISK,” *DTIC*, 01 January 1964. [Online]. Available: https://apps.dtic.mil/sti/citations/AD0433976.

[14] Joel CFD, “What is Y+ and why is it important?” Accessed April 14, 2022. [Online]. Available: https://joelcfd.com/what-is-y-and-why-is-it-important/.

[15] Vortarus Technologies LLC, “Affinity Laws for Pumps and Fans.” Accessed April 7, 2022. [Online]. Available: https://vortarus.com/affinity-laws-for-pumps-and-fans/.

[16] Google Sites, “Terminal,” Accessed April 14, 2022. [Online]. Available: https://sites.google.com/site/terminalbpp/.

[17] Futek Advanced Sensor Technology, Inc., *Torque and Thrust Biaxial Sensor*, Model MBA500, Accessed April 21, 2022. [Online]. Available: https://media.futek.com/content/futek/files/pdf/productdrawings/mba500.pdf

[18] C. R. Green, “Modeling and Test of the Efficiency of Electronic Speed Controllers for Brushless DC Motors,” M.S. thesis, Department of Aerospace Engineering, California Polytechnic State University, San Luis Obispo, CA, USA, September, 2015. [Online]. Available: https://digitalcommons.calpoly.edu/cgi/viewcontent.cgi?article=2617&context=theses.

[19] MPS, “Brushless Vs Brushed DC Motors,” Accessed November 14, 2021. [Online]. Available: https://www.monolithicpower.com/en/brushless-vs-brushed-dc-motors.

[20] U.S. Department of Energy, “Determining Electric Motor Load and Efficiency,” Accessed November 14, 2021. [Online]. Available: https://www.energy.gov/sites/prod/files/2014/04/f15/10097517.pdf.

[21] T-Motor, “U8 Lite L KV95,” Accessed November 14, 2021. [Online]. Available: https://store.tmotor.com/goods.php?id=1081.

[22] T-Motor, “U8 Lite KV85,” Accessed November 14, 2021. [Online]. Available: https://store.tmotor.com/goods.php?id=462.

[23] MiniPro, “Understanding Motor Turns & Kv Rating,” Accessed November 13, 2021. [Online]. Available: https://www.minipro.com/blogs/articles/motor-turns-kv-rating.

[24] Abel Electronics, “Generating a PWM Signal,” Accessed November 14, 2021. [Online]. Available: https://www.abelectronics.co.uk/kb/article/1078/generating-a-pwm-signal.

[25] M. Yoon “On Driving Signal of Electronic Speed Controller for Small Multi-Rotor Helicopter,” *International Journal of Engineering Research & Technology (IJERT)*, Vol. 4, Issue 11, 2015.

[26] User Manual Brushless ESC for Airplane. Flycolor. Accessed 15 November, 2021 [Online] Available: www.flycolor.net.

[27] T Motor, 28x9.2 Propeller. Accessed December 14, 2021. [Online]. Available: https://grabcad.com/library/t-motor-28x9-2-propeller-1.

THIS PAGE INTENTIONALLY LEFT BLANK

INITIAL DISTRIBUTION LIST

1. Defense Technical Information Center
   Ft. Belvoir, Virginia

2. Dudley Knox Library
   Naval Postgraduate School
   Monterey, California